High-performance Perovskite Solar Cell and Photocathode

by

Yulin Liu

Bachelor of Science, Harbin Institute of Technology, 2016

Master of Science, Harbin Institute of Technology, 2018

Submitted to the Graduate Faculty of the

Swanson School of Engineering in partial fulfillment

of the requirements for the degree of

Doctor of Philosophy

University of Pittsburgh

2022

UNIVERSITY OF PITTSBURGH

SWANSON SCHOOL OF ENGINEERING

This dissertation was presented

by

Yulin Liu

It was defended on

October 4, 2022

and approved by

Markus Chmielus, PhD, Associate Professor, Department of Mechanical Engineering and Materials Science

Paul Ohodnicki, PhD, Associate Professor, Department of Mechanical Engineering and Materials Science

Prashant Kumta, PhD, Professor, Departments of Bioengineering, Mechanical Engineering and Materials Science, Chemical and Petroleum Engineering

Dissertation Director: Jung-Kun Lee, PhD, Professor, Department of Mechanical Engineering and Materials Science

High-performance Perovskite Solar Cell and Photocathode

Yulin Liu, PhD

University of Pittsburgh, 2022

ABX_3-based organometal halide perovskite solar cells (OMH PSCs) have opened up a new overture in photovoltaic (PV) devices for sunlight harvesting. Methylammonium and formamidinium lead halides ($MAPbI_3$ and $FAPbI_3$) are the two most feasible structures due to their excellent optoelectrical performance and manageable deposition method. However, to stimulate the outspread applications of OMH PSCs in the field of industry, further progress on the improvement of their power conversion efficiency (PCE) and compatibility with related PV systems must be achieved. Therefore, this dissertation has put effort into PCE improvement of PSC devices. Near-infrared (NIR) plasmon particles have been utilized to improve the solar energy harvesting at the near-band edge of the $MAPbI_3$. Moreover, we have also developed a new kind of electron transport layer (ETL)-SnO_2. The efficient modification of the bottom interlayer between $FAPbI_3$ and SnO_2 has considerably decreased trapping sites and stabilized the perovskite growth. Finally, an inverted PSC structure has been assembled with noble metal free catalysts for solar-driven water splitting application.

Plasmon silica@silver (SiO_2@Ag) core@shell particles with IR surface plasmon resonance wavelength are incorporated into $MAPbI_3$-based PSC devices. Based on the position and concentration optimization, the IR plasmons can considerably increase the quantum efficiency in the near-band edge range of the devices, where typically the fragile part is. Investigation on light management and carrier dynamics includes wavelength-dependent photoluminescence (PL) analysis and electromagnetic simulation.

PbS quantum-dot modification has been employed to promote the SnO_2 ETL-based PSCs. An ultrathin interfacial layer between planar SnO_2/$FAPbI_3$ simultaneously passivated the trapping sites, induced perovskite growth and decreased energy level mismatch. As a result, incredible current-voltage performance improvement and elongated stability are attained due to the reduction of nonradiative carrier recombination.

Finally, PSC devices are extended to convert solar energy to water splitting in a versatile method with molybdenum carbide (Mo_2C)-based catalysts. Commercially purchased metal foil-Titanium foil has been deployed here as a protection layer for the PSC devices and also the substrate for the earth-abundant catalysts. The hybrid photocathode structure PSC/Ti/Mo_2C can be directly immersed into an acid electrolyte solution for hydrogen evolution over 10 hours.

Table of Contents

List of Tables

List of Figures

Acknowledgement

It is my privilege to work under the guidance of Professor Dr. Jung-Kun Lee. Not only has Dr. Lee led me towards the field of optical materials and semiconductor devices and let me experience the beauty of establishing a personal research brand and story, but he also inspired me with his working spirit, passion and brave rise to the challenge faced with difficulties, which would guide me throughout the rest of my life. I feel so fortunate to have a Ph.D. advisor like him and I really appreciate his support and mentorship in those years.

I want to thank my committee members: Professor Dr. Prashant Kumta, Professor Dr. Markus Chmielus and Professor Dr. Paul Ohodnicki for their great lecture and guidance, encouragement and patience during my study and research at University of Pittsburgh.

During my PhD life at Pitt, I have met so many great and helpful people here. Thanks to all the members in our lab for making my stay in Pitt a great memory. Without their kindness and support, life would become hard and challenging. I appreciate the help from Dr. Seongha Lee, Dr. Fen Qin and Professor Dr. Yingjie Wu for their consistent technical support, endless inspiration as well as fruitful discussion. I would like to thank Dr. Salim Caliskan for lab training at my initial stage of my PhD study and Anqi Wang, Sumin Bae, Junyan Zhang, Joseph John Churey Damian and Jorge Torres for their kind experimental support and experience sharing. Moreover, I could not have done my research without the instruction and help from staff in the Department of Mechanical Engineering and Materials Science, Materials Science Characterization Lab and Nano-Scale Fabrication and Characterization facility.

Finally, I would also like to express my deepest gratitude to my family, my friends and Dr. Arthur Schopenhauer for giving me agape encouragement and supporting me to follow the heart of enjoying and discovering the truth of my life.

1.0 Introduction

1.1 Solar Industry

It is the irreversible trend that fossil energy source will have been gradually fading out in the historic stage of human civilization development.[1] Though the combination of coal, oil and natural gas retains 70% portion of world primary energy supply in 2020, DNV energy transfer outlook 2021 forecasted that traditional energy was losing position and would be lowered to half in 30-year future, testament to the starting up of a decarbonization era. Other than motivated by the environment pollution and limited consume of fossil resource, the rise for the renewable energy depends on the efficient and compact industrial electrification network for energy transition.[2] Solar energy can be competitive to other power sources such as nuclear, wind and hydropower with their massive productivity and direct storage.[3] Photovoltaic (PV) devices such as solar panels are already one of the cheapest forms of new power almost everywhere, maintaining a surplus power usage at a satisfactory cost level. Solar energy will be critical asset in the modern industrial power system within the next decade.

Solar radiation is radiant (electromagnetic) energy from the sun. It provides light and heat for the earth and energy for photosynthesis for organic life foundation. This solar radiation spectrum is divided into three relevant bands, which are ultraviolet (UV), visible, and infrared (IR). In the whole spectra, IR and visible radiation make up 49.4% and 42.3% of the total light reaching Earth's surface while UV light provides less than 9%.[4] Each range of the solar radiation has indispensable impact on earth and not all radiation can be taken account into solar industry. it is the premise to notice that much of it will be absorbed, reflected or scattered in the outer atmosphere.

And the received amount and intensity of solar radiation by a location/surface depends on a variety of factors including latitude, season, time of day, cloud cover and altitude. To unify the measurement of PV test, most research including ours have taken the standard 1.5G solar illumination condition which is represented by the American Society for Testing and Materials (ASTM). The G-173 spectra shows terrestrial distributions of power as a function of wavelength on a surface of specified orientation under one and only one set of specified atmospheric conditions (i.e., the surface is defined as an inclined plane at 37° tilt toward the equator, facing the sun, at an elevation of 41.81° above the horizon). More details about PV measurement and industry standards and atmospheric condition definitions can be obtained from U.S. standard atmosphere.

The solar cell is a semiconductor device consisting of PN junctions which can utilize the solar energy via PV effect. First, when the incident photon energy surpasses the bandgap of the material, the electrons in the shining part will be excited from a low-energy state to a high-energy state and the electron-hole pairs will be massively produced through the absorption of photons.[5] In a semiconductor, this state transition can be divided into two types, band to-band transition and transition through defect states. In this study, most of our materials are direct band structure and thus we are more focused on the valence band-to conduction band transition.[6] The excess energy ($hv-E_g$) can be dissipated as thermal energy while the excited electron collides with the lattice and finally relaxes to the bottom of conduction band. However, the inter-band energy levels caused by the impurities or defects will also be mentioned since some carrier kinetics will be influenced in this study.[5, 7] Under the drive of built-in electric field inside the PN junctions, the photogenerated electrons will be swept to N side and holes to the P side. Therefore, the PN junction is under a forward bias status and once connected with the out-electric load, there will be a continuous power output under the continuous irradiation, which is solar energy. The P and N sides are defined as the cathode and anode, respectively.

According to the fundamental operation mechanism in a working solar cell device, it can be concluded that the vital parts are carrier generation revolving light absorption and carrier kinetics including recombination, transportation and collection.[8] Thus, in 1961, with reasonable PV assumptions and standard solar radiation condition, Shockley and Queisser have calculated the theoretical efficiency of semiconductor solar cells and depicted the result in Figure 1.[9] Only considering absorption loss, black-body radiation loss and radiative recombination, the upper limit of electric usage efficiency get as far as 34% with the optimal bandgap of 1.34 eV. Otherwise, the theoretical device efficiency will be decreased by radiative recombination or abruption loss due to the small or large bandgap. This directed us to a clear pathway involving criteria and expectations for the solar cell. The most straightforward and versatile strategy is to choose a semiconductor with a proper bandgap.

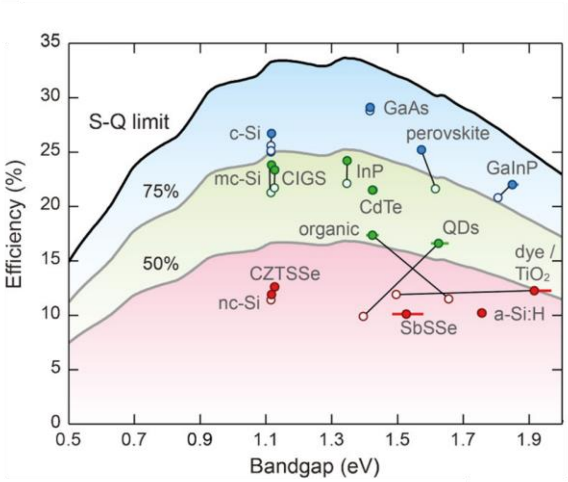

Figure 1 2020 Record efficiency of solar cells of different materials against their bandgap. (Reproduced with permission from 9. Copyright 2020 American Chemical Society.)

So far, 95% value of the global solar panel market are based on silicon (Si) . As the second most abundant material on earth, silicon is the most widely utilized semiconductors due to the batched and mature techniques, satisfying the developing rhythm of electronics and energy industry. Silicon has a bandgap of 1.11 eV which is close to 1.34 eV and its electric properties are able to considerably be tuned and improved by slight element doping. A typical commercial silicon solar cell is fabricated by two types of crystalline silicon material where the p-type silicon is produced by boron or gallium doping and the n-type silicon is usually doped by phosphorus, as shown in Figure 2.[10]

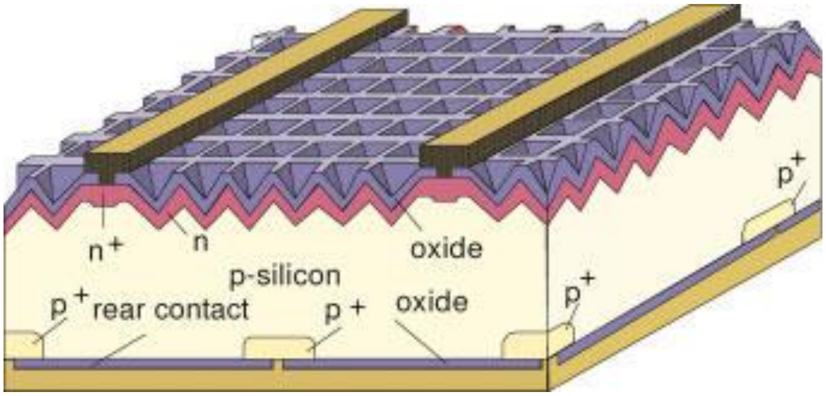

Figure 2 Illustration of a milestone silicon solar cell with 25% efficiency. (Reproduced with permission from 10. Copyright 2009 Wiley.)

Other than silicon, there is another strong candidate material which has great potential for solar cell device with extra high power conversion efficiency (PCE). In 1839, ABX_3 structural perovskite compound calcium, titanium and oxygen was first discovered in Ural mountains and named after a Russian mineralogist, Count Lev Perovski. Then in 2006, Tsutomu Miyasaka and his colleagues of Toin University discovered that some perovskites are semiconductors and could be applied on the PV devices. As a beginner of the perovskite solar cell era, they first realized the prototyping of first perovskite solar cell (PSC) based on the organic metal halide (OMH) $MAPbBr_3$ with a PCE of 2.2% in 2006[11] and $MAPbBrI_2$ with an increased PCE of 3.8% in 2009[12]. Since then, interest in PSC devices has been perked up. Typical OMH perovskite phase and corresponding crystal structure is shown in Figure 6 and generally, the metastable alpha (α) phase is required for the PV devices for its photoactivities.[13] Perovskites are hybrid compounds made from metal halides and organic constituents in a general chemical formula ABX_3, in which A involves an organic cation group or inorganic metal cations such as Methylammonium ($CH_3NH_3^+$), formamidinium ($NH_2CH{=}NH_2^+$), as well as cesium (Cs^+); B is generally a heavy metal cation such as lead(II) (Pb^{2+}) and tin(II) (Sn^{2+}); X is commonly a halide ion including chlorine (Cl^-), bromide (Br^-), or iodine (I^-) (Figure 3). The Goldschmidt tolerance factor (t), is a simple way to check whether or not specific compositions can form a stable perovskite structure,[14]

$$t = \frac{r_A + r_X}{\sqrt{2}(r_A + r_X)} \tag{1-1}$$

where r_A, r_B, and r_X represent the corresponding ionic radius of A, B and X, respectively. The stable 3D perovskite structures require t value locates in the range of 0.8~1.0.[15]

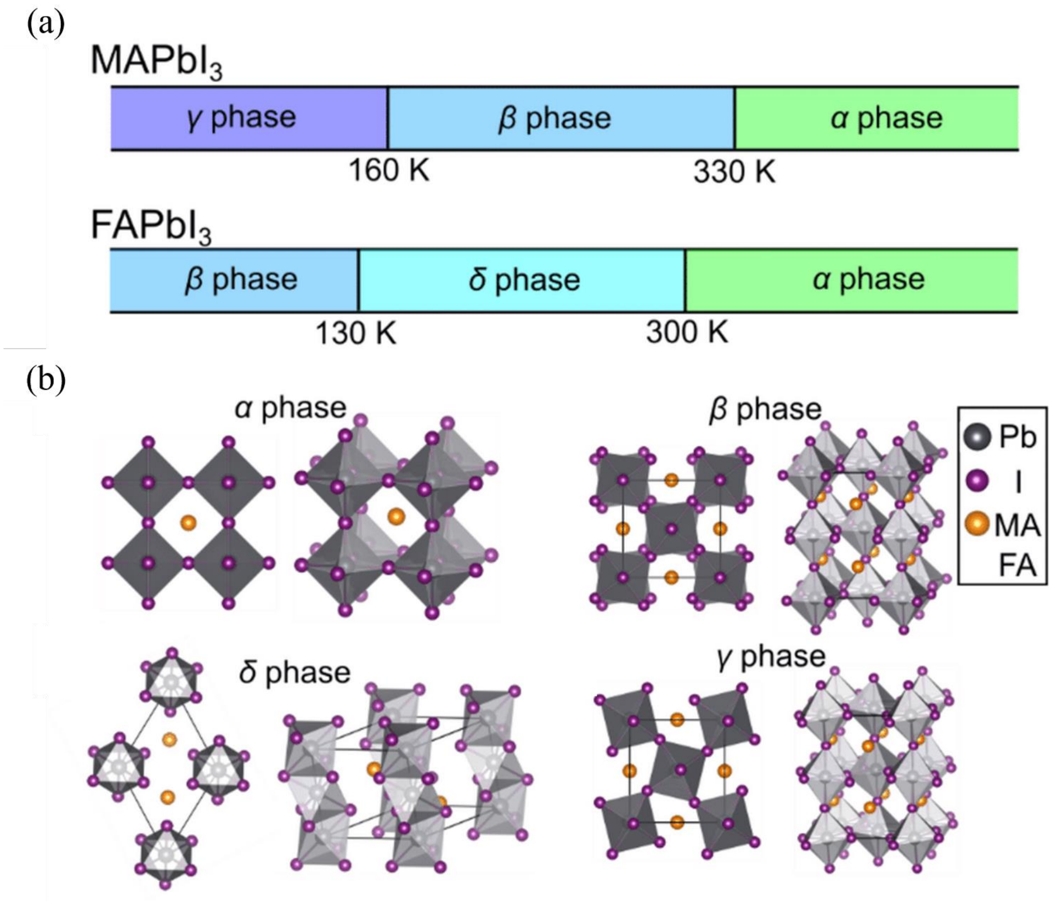

Figure 3 (a) Typical crystal structure and phase variations of $MAPbI_3$ and $FAPbI_3$ at various temperatures: (b) the cubic alpha (α) phase, the tetragonal beta (β) phase, the trigonal delta (δ) phase, and the orthorhombic gamma (γ) phase. (Reproduced with permission from 13. Copyright 2020 Springer Nature.)

OMH perovskites have been confirmed as a proper material for solar cell fabrication for low-cost material constitutes, proper bandgap (~1.5 eV), easily tunable band structure, long carrier lifetime, diffusion length and solution-based deposition methods with low temperature and controllable processes.[15-17] Thus, they have shown great potential not only in solar cells, but an extensive range of PV applications such as LED lights, lasers, photodetectors and so on. Thousands of articles related to PSCs have been published and now a lab-scale device of 25.7%[18] PCE has been achieved, outshining the performance of commercial multi-crystalline silicon solar cells which did take more than 60 years to obtain, according to the record efficiency of different PV technologies reported 2022 from the National Renewable Energy Laboratory (NREL). Thus, there is an intensive research passion on pushing perovskite efficiency to go higher and figuring out the stability and scale-out issue, the critical factors, whereas the PSC devices could be put in viable usage routine.

1.2 Perovskite Solar Cell

Unlike silicon solar cells made by n-type and p-type Si materials, typical PSC design utilizes perovskite materials as a light absorber and corresponding semiconductors as electron transport layer (ETL) and hole transport layer (HTL) with suitable electron band structures favoring carrier transportation. As shown in Figure 4a, the perovskite absorbs the light, producing the charge carriers.[8] Then carrier dissociation occurs at the interface and the charges are extracted towards the FTO and metal as anode and cathode, respectively. Commonly handled semiconductors are listed in Figure 4b.[19]

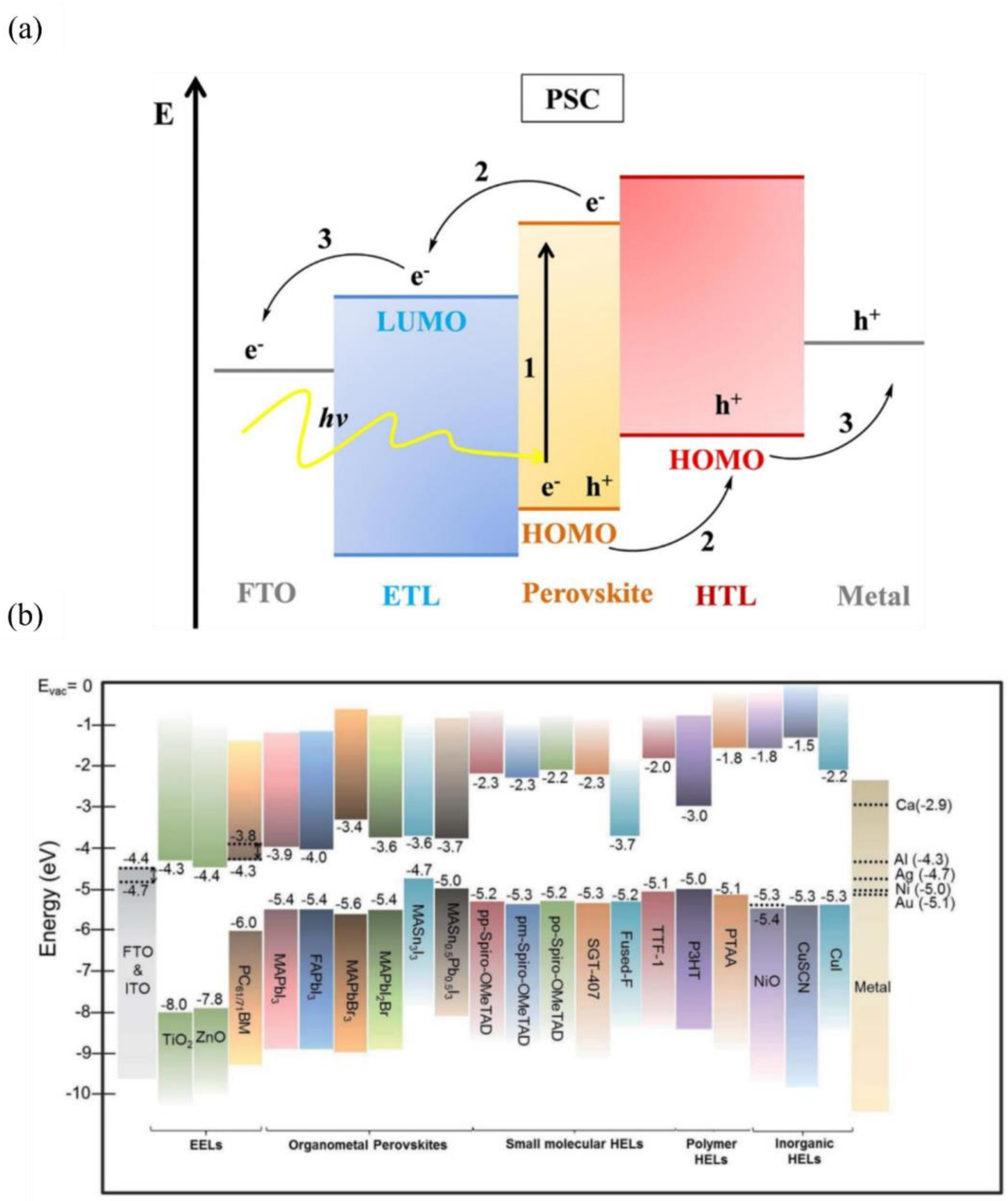

Figure 4 Schematic of (a) band diagram and operation principle of PSC (Reproduced with permission from 8. Copyright 2017 Elsevier.) and (b) energy level diagram of representative hybrid halide perovskites and charge-extraction interlayers. (Reproduced with permission from 19. Copyright 2015 RSC Publishing.)

Generally, based on the light incident direction, PSC structures are classified into two major types: n-i-p structure and p-i-n structure. And each kind of structure can be further divided into mesoporous and planar structures.[20] The device is fabricated on a transparent conductive electrode fluorine-doped tin oxide (FTO) glass substrate, the ETL consists of a blocking TiO_2 layer and a mesoporous scaffold (TiO_2 particles), a $MAPbI_3$ perovskite absorption layer, a Spiro-OMeTAD HTL and a top Au electrode layer. The mesoporous structure has usually been used to increase the contact area of the active layer and transport layers.

One of the obstacles facing the commercialization of PSCs is that their efficiency and operational stability drop as they scale up, making it a challenge to maintain high performance in a complete solar cell.[20, 21] Moreover, although PSCs have achieved high PCE, the operation mechanism and device physics of PSCs are not yet clearly understood. To be able to optimize the PCE of PSCs further, it is essential to gain a better understanding of material properties that influence the PCE. Based on the working principles of the PSC devices, proper materials should be close to fabricate high-efficiency devices. Here we are going to introduce several kinds of common materials for active layer, ETL, HTL, all of which are also going to be fabricated and applied to prototype a complete device in this dissertation.

1.2.1 Photo-Active Layer: $MAPbI_3$ and $FAPbI_3$

As mentioned previously, $MAPbI_3$ and $FAPbI_3$ are the most commonly used OMH perovskite materials, which are easily fabricated via various methods including spin coating,[16, 17] vacuum deposition,[22] printing[23] at a relatively low temperature at around 100 or 150 ^oC. Herein, polycrystal perovskite are fabricated using a two-step spin-coating method with anti-solvent, as can be seen in Figure 5a.[24] The primary growth mechanism is increasing the precursor solution concentration into a high level and inducing the seed formation in an ultra-short time range. Then, there is a start of uniform grain growth followed by the classical nucleation theory and Lamer's

1950 model (Figure 5b).[5, 26] The quality of the active layer is the most crucial part in a high-efficient PSC device.[24]

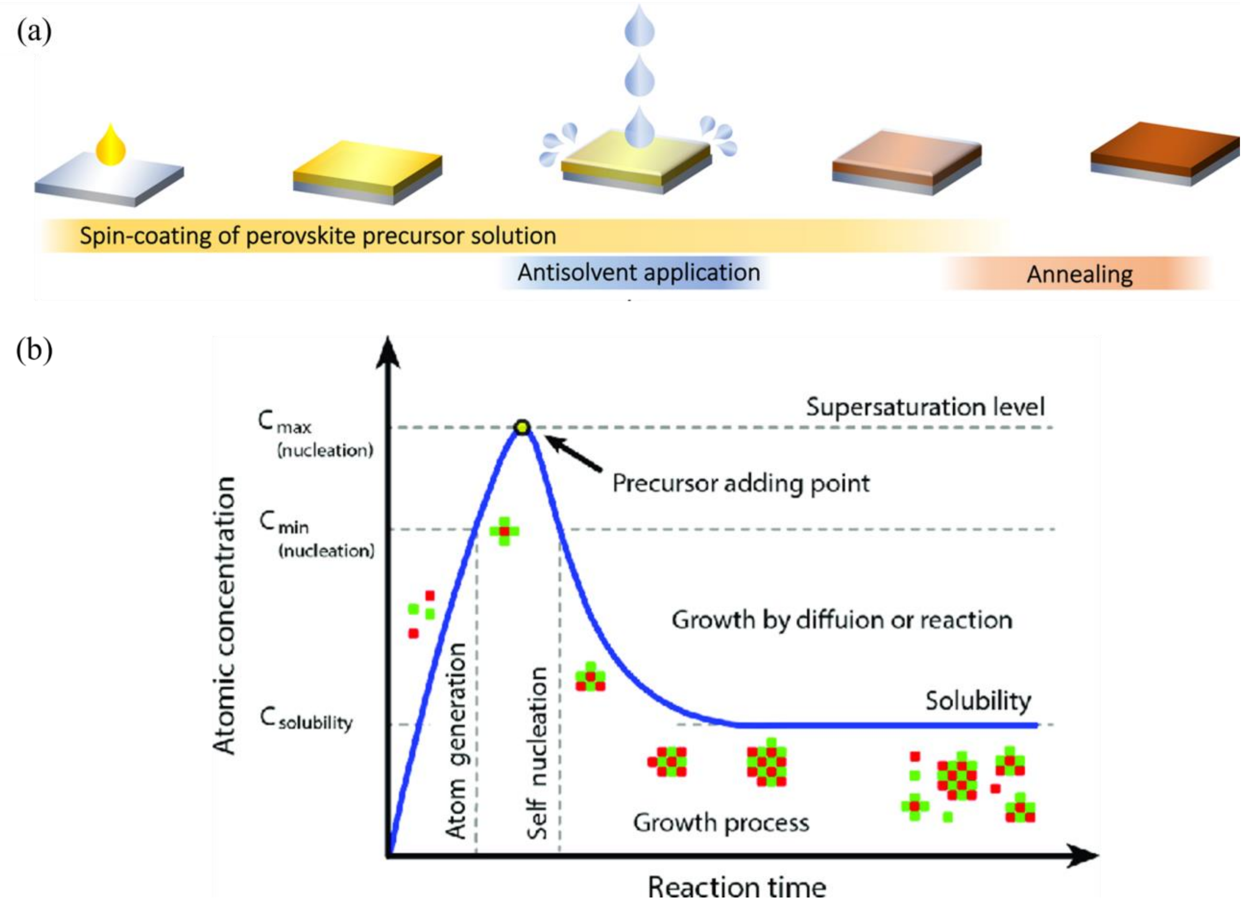

Figure 5 (a) Schematic illustration of antisolvent-assisted one-step deposition of perovskite film (Reproduced with permission from 24. Copyright 2021 Springer Nature.)and (b) classical Lamer diagram for monodispersed particle formation (homogeneous nucleation). (Reproduced with permission from 25. Copyright 1950 American Chemical Society.)

The reaction pathways for $MAPbI_3$ and $FAPbI_3$ are different though both from a precursor solution dissolved in the solvent such as DMF, DMSO, toluene, NMP or their mixture with special molar/volume ratio. $MAPbI_3$ usually synthesized from a combination of MAI and PbI_2 powders with a stoichiometric ratio of 1 to 1 as shown in Figure 6.[27] The precursor was dissolved into a mixture solvent of DMSO and DMF, where DMF has a high solubility while DMSO has low volatility. The soft colloid particles with iodine sharing PbI_x framework can be attached with DMSO and thus the particle size can be controlled. During the post-annealing process, the MAI will incorporate to the intermediate framework to form final perovskite films. Thereafter, by tuning the precursor solution concentration and the volume ratio of DMF/DMSO, the drying time and film formation process can be controlled. However, the photoactive alpha $FAPbI_3$ is usually transformed from the delta phase $FAPbI_3$.[28] The critical point to form high-quality photoactive $FAPbI_3$ is the stabilization and induction of interphase.[29, 30] $MAPbBr_3$ and MACl are two stabilizers which can decrease the activation energy of the phase transformation, as shown in Figure 6b.[29] Compared with $MAPbI_3$, $FAPbI_3$ perovskites are considered to exhibit higher thermal stability and a more ideal band gap of 1.48 eV due to the more symmetry FA anion.[31] However, as $FAPbI_3$ require for a higher annealing temperature (150 ^{o}C) than $MAPbI_3$ (100 ^{o}C), surface passivation for the $FAPbI_3$ to decrease the remaining surface tension mismatch is a necessary step for high-performance $FAPbI_3$ based PSC device.

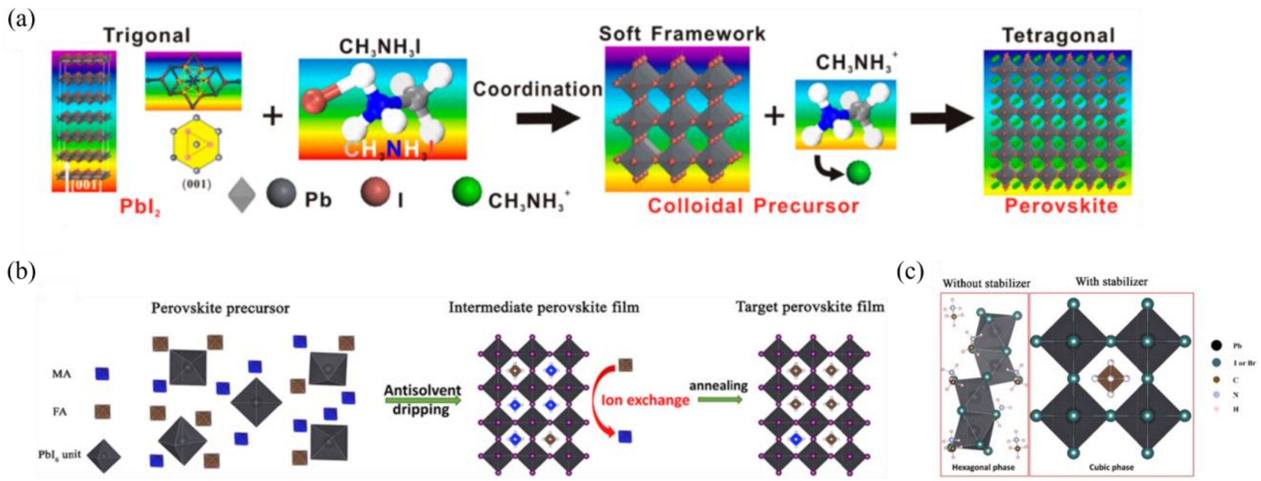

Figure 6 Reaction pathways of (a) $MAPbI_3$ (Reproduced with permission from 27. Copyright 2015 American Chemical Society.) and (b) $FAPbI_3$. And (c) $FAPbI_3$ interphase with and without MACl and $MAPbBr_3$ stablizers. (Reproduced with permission from 29. Copyright 2019 Elsevier.)

1.2.2 Electron Transport Layer: TiO_2 and SnO_2

TiO_2 is a widely utilized ETL material in PSCs for n-i-p planar structures due to its proper bandgap and good transmittance. However, when tested under continuous light illumination, TiO_2 obtains electrons from I^-, leading to perovskite cubic structural damage and generation of I_2.[32] Furthermore, TiO_2 has a disadvantage of poor electron mobility (μ_e) (~10^{-5} $cm^2/(V•s)$) due to impaired intrinsic electron mobility. Therefore, TiO_2 ETL based PSCs usually suffer from low electron mobility, high defect state density, and high chemical catalytic activity, limiting the overall device performance. At the same time, the TiO_2 mesoporous layer is always post-treated at high temperatures (typically above 450 ^{o}C) to increase the conductivity and remove the organic material in the TiO_2 paste.[33]

On the other hand, planar structures for OMH PSC devices have recently garnered attention, due to their simple and low-temperature device fabrication processing.[34] Unfortunately, planar structures typically show *J-V* hysteresis and lower stable device efficiency compared with mesoporous structures.[32] SnO_2 is a promising candidate for planar PSCs. It has attracted tremendous research efforts for its high transmittance, suitable bandgap, matched energy level, high electron mobility (~10^{-3} $cm^2/(V\bullet s)$) compared with that of TiO_2, and low-temperature preparation.[35] Zhang and You et. al. compared the planar structural PSCs based on SnO_2 and TiO_2, as shown in Figure 7. It has been shown that SnO_2-based devices are almost free of hysteresis because SnO_2 ETL with good quality could enhance charge transfer from perovskite to electron transport layers, and reduce charge accumulation at the interface, compared with TiO_2. Till now, the certificated efficiency of SnO_2 based planar n-i-p PSC is 25.5% and 25.7% and high operational stability and facilitated the scale-up of the PSCs to larger areas, which is fully compatible with mesoporous structural PSC devices.[18]

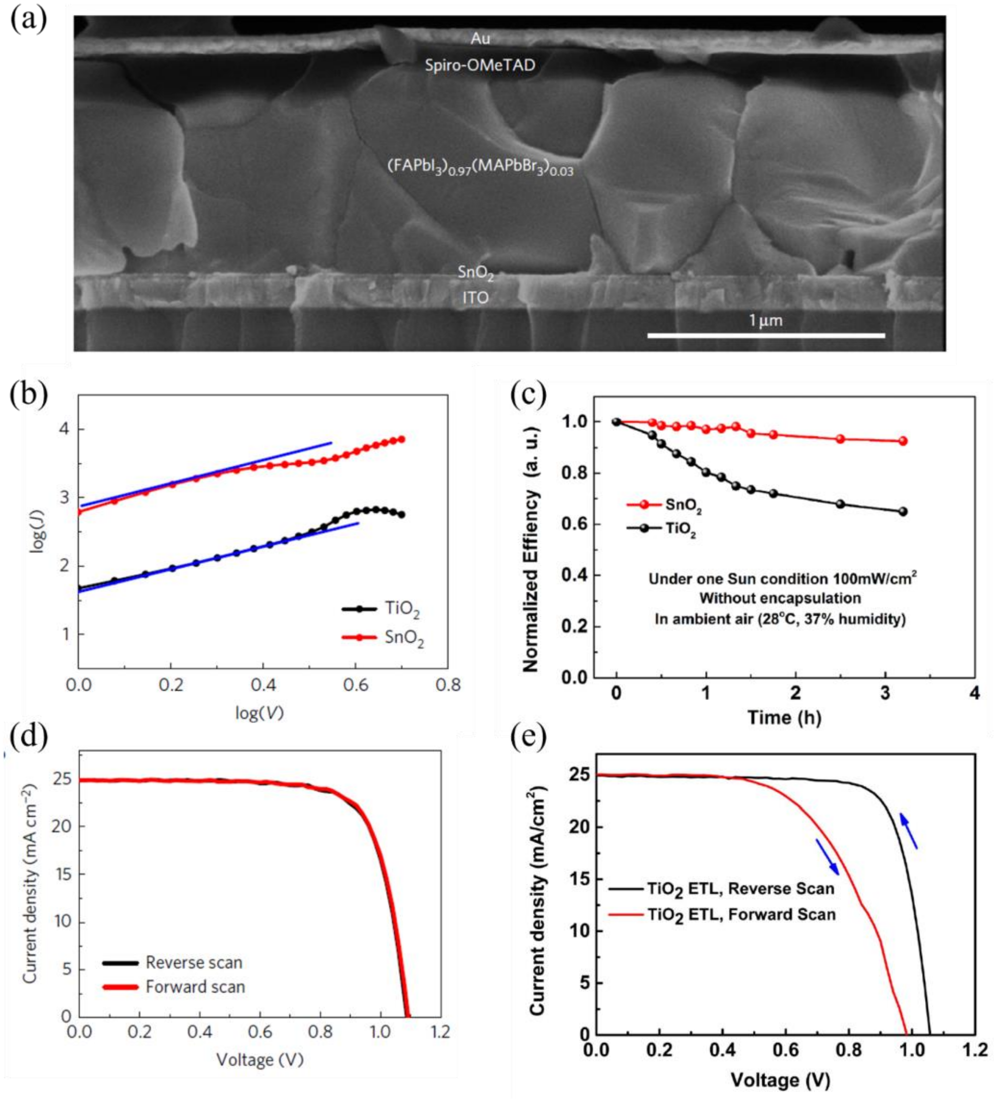

Figure 7 (a) Cross-section SEM image of planar PSC device and (b) log(*J*)-log(*V*) plots, (c) normalized stability and (d-e) *J-V* curves under different scan directions for the SnO_2 and TiO_2 as ETL. (Reproduced with permission from 32. Copyright 2016 Nature Publishing Group.)

1.2.3 Solar Cell Device Characterization

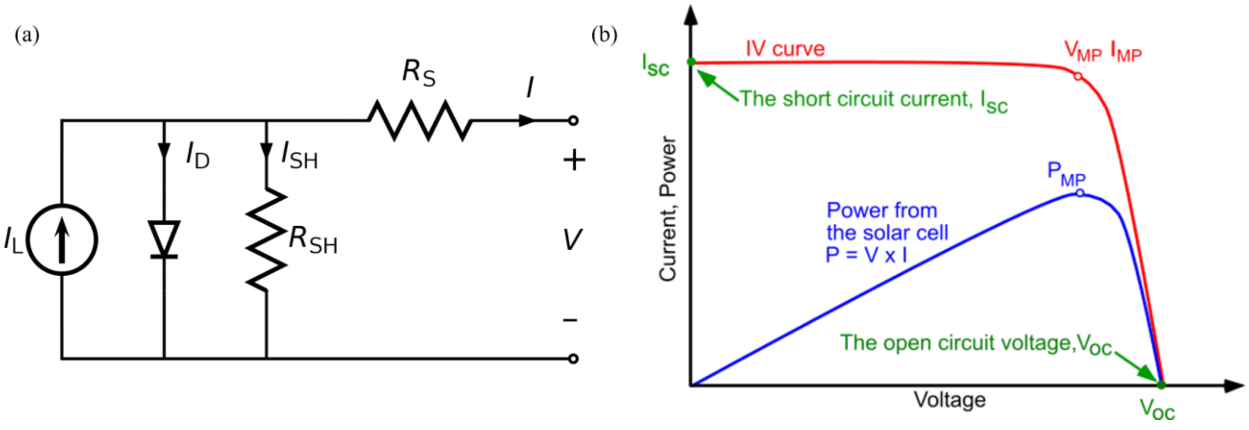

Figure 8 Solar cell (a) equivalent circuit and (b) *J-V* curve.

The current-voltage (*J-V*) curve is the most important measurement in solar cell device characterization. Figure 8a shows a simplified but versatile equivalent circuit for a PSC. Under the illumination conditions, the IV curve can be shifted into the first quadrant where power can be extracted from the PN diode. Therefore, the solar cell operation depends on the light absorption as well as carrier dynamics. The net current (I) flowing through the can be calculated using the equation below:

$$I = I_L - I_0[\exp(\frac{qV}{nkT})] \tag{1-2}$$

Where I_L is the illuminating current, I_0 term is the dark current, related to carrier recombination. I_0 is the diode leakage current density in the absence of light, q is electron charge, V is applied voltage, k is Boltzmann's constant, T is the absolute temperature. n is the ideality factor for a diode, usually ranging from 1~2. Plotting the equation gives the IV curve as shown in Figure 8b with the relevant points on the curve labeled. The power curve has a maximum power point (MPP) denoted as P_{MPP} where the solar cell should be operated to give the maximum power output.

The shortcut-circuit current density (J_{SC} [mA/cm^2]) is the current through the solar cell when the applied voltage is zero, and thus totally rests on the generation and collection of light-generated carriers. The J_{SC} value depends on many factors such as the incident light density and spectrum, the absorption and reflection properties of the devices, the minority-carrier collection probability and so on.

To obtain more details about the J_{SC}, incident-photon-to-current efficiency (IPCE), also referred to external quantum efficiency (EQE) can be conducted. As shown in Figure 9, IPCE is the ratio of the number of carriers collected by the solar cell to the number of photons of a given energy incident on the solar cell, given as a function of wavelength or photon energy.

$$\mathrm{IPCE}(\%)=\frac{N_e}{N_p}=\frac{1240\times J_{photon}}{\lambda\times I_{incident,\lambda}} \tag{1-3}$$

$$J_{SC}\approx J_{int}=\int \mathrm{IPCE}(\lambda)\times I(\lambda)\times\lambda\times(\frac{e}{hc})d\lambda \tag{1-4}$$

If all photons of a certain wavelength are absorbed and the resulting minority carriers are collected, then the quantum efficiency at that specific wavelength is unity.[36] The IPCE for photons with energy below the band gap is zero. Therefore, ideal IPCE curve should be in square shape while usually reduced by recombination effects. It is worth noting that the red portion is a weak absorption range in perovskite and easily degrades. Thus, to increase the efficiency and stability of the PSCs, the absorption and carrier collection at near band edge range require further investigation.

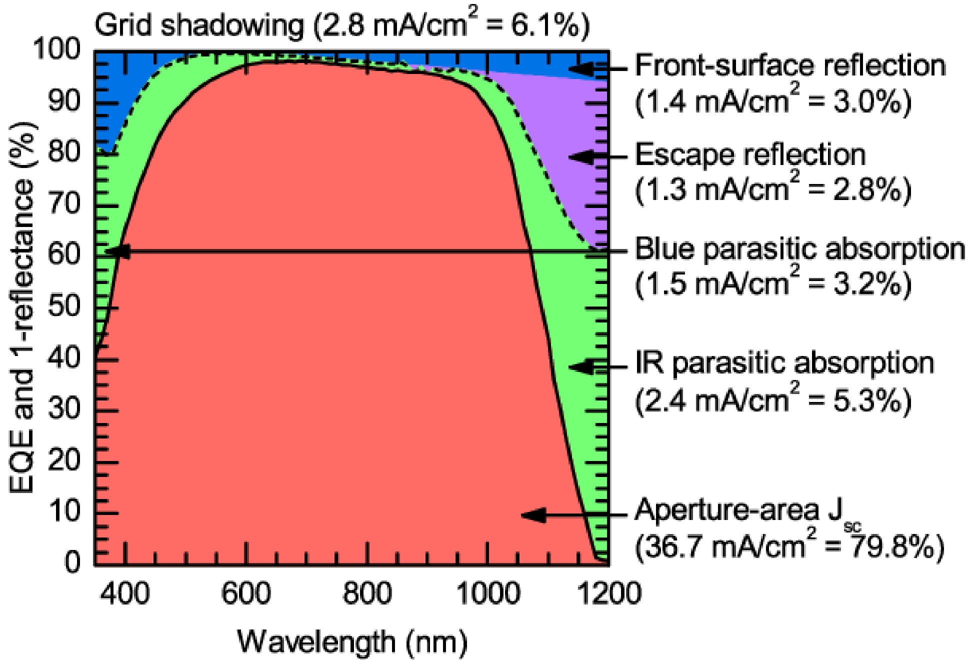

Figure 9 IPCE curve of a solar cell. (Reproduced with permission from 36. Copyright 2013 IEEE.)

Another prominent PV parameter that has led to the high efficiency in PSCs is the open-circuit voltage (V_{OC}). The origins of the V_{OC} in PSCs are complicated and influenced by many factors. Generally, the open-circuit voltage (V_{OC}) of an illuminated solar cell is defined by the energy difference between the quasi-Fermi level of ETL ($E_{F,e}$) and HTL ($E_{F,h}$) as: [37]

$$-qV_{OC}=E_{F,e}-E_{F,\,h} \tag{1-5}$$

For PSCs, the V_{OC} can be written as:

$$-qV_{OC}=E_g-\varphi_e-\varphi_h-\Delta E_{loss} \tag{1-6}$$

where φ_e/φ_h is electron/hole injection barrier height, ΔE_{loss} represents energy losses in transporting charge carriers to the electrodes. Thus, it should be noted that the energy alignment of ETL/HTL and active layer helps in the efficient transport. [18, 32, 38] Thus, to decrease the V_{OC} loss of the PSC device, the choice of carrier transport materials with proper band energy structure and high carrier mobility to obtain better energy level alignment and carrier extraction, as shown in Figure 10.[39]

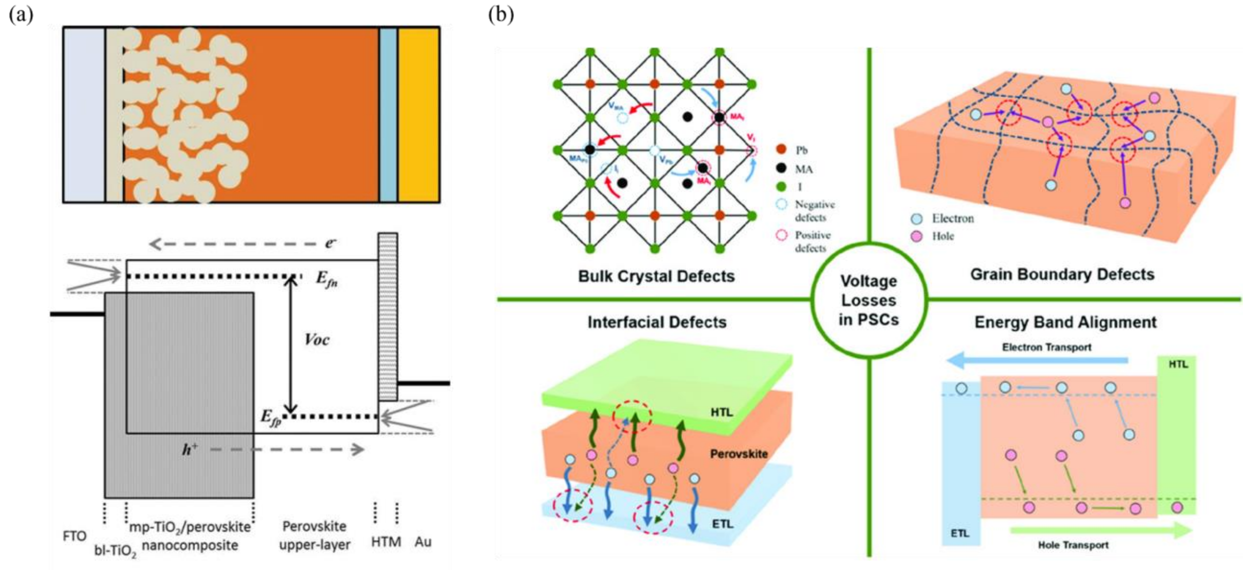

Figure 10 Schematic illustration (a) mesoporous PSC device energy band diagram and (b) the origins of voltage losses in PSCs. (Reproduced with permission from 39. Copyright 2020 WILEY.)

1.3 Tunable Surface Plasmon

One of the basic strategies within the optical research area is enhancing the interaction of light, sometimes with specific wavelengths. And this also works for the perovskite solar cells, which can contribute to photon absorption enhancement and photon-generated carrier transportation. Localized surface plasmon resonance (LSPR or SPR) is an ancient phenomenon but still widely used today. It is that light can induce collective oscillations of the valence electrons in noble metal nanoparticles (NPs).[40] As shown in Figure 11a, the oscillating electron cloud exhibits a lifetime on the order of femtoseconds that is limited by different radiative and nonradiative damping processes.[41] The population of surface plasmons that decays by radiative damping is converted into photons while the population that decays by non-radiative damping is converted into electron-hole pairs by inter-band and intra-band excitations (as shown in Figure 11b).[42] Surface plasmons mainly decay through nonradiative processes are called absorption, since the irradiating energy is absorbed by the NPs and subsequently transferred to their surroundings. Otherwise, the radiative decay is called scattering. In 1908, Gustav Mie derived analytical expressions for the absorption and scattering cross-sections of spherical NPs of arbitrary size.[43] This theory has evolved to the generalized Mie theory that can also accurately predict the optical behavior of particles of different shapes, such as ellipsoids and rods.[44] Based on this theory, metallic particles have become a new kind of optical materials that have been widely studied. There are various metallic geometries, such as spheres[45], disks[46], and shell[47].

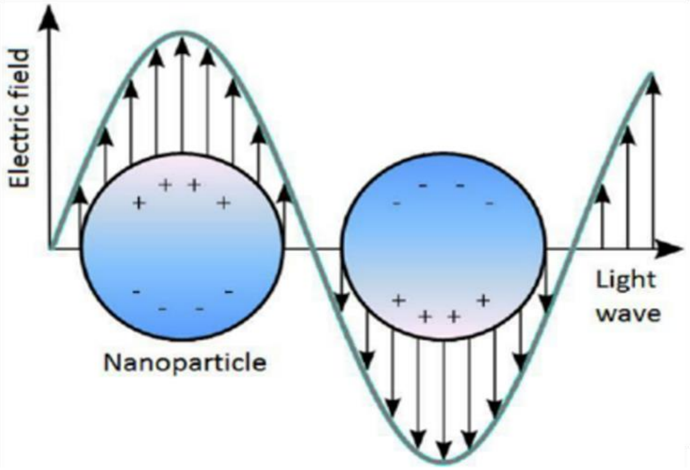

Figure 11 Schematic of LSPR in the metal NPs. (Reproduced with permission from 41. Copyright 2014 MDPI)

1.3.1 SiO_2@Ag Core@Shell Particles

Core shell NPs represent one of the most interesting areas due to their unique combined and tailored properties.[40, 48] Core shell particles consist of a dielectric or semiconducting core coated with a nanometer-scale metallic shell. These particles manifest a strong optical resonance that is dependent on the dimension of core and metallic shell as well as their refractive index, accounted for exceptionally well by Mie scattering.[49, 50] By varying material selection and core-shell size, this optical resonance can be placed virtually anywhere across the visible or IR regions of the optical spectrum.[51] Moreover, N. J. Halas' group has presented a simple and intuitive hybridization model-an electromagnetic analog of molecular orbital theory to describe the plasmon response of complex nanostructures of arbitrary shape.[52] The LSPR of core shell structure can be seen as an interaction between the essentially fixed-frequency plasmon response of a nano-sphere and a nanocavity. The sphere and cavity plasmons are electromagnetic excitations that induce surface charges at the inner and outer interfaces of the metal shell. Because of the finite thickness of the shell layer, the sphere and cavity plasmons interact with each other which split into two new resonances: the lower energy symmetric plasmon and the higher energy antisymmetric plasmon. Thus, the inside core and the thickness of the shell is the key to the LSPR. Figure 12 has plotted the core shell ratio versus resonance wavelength for a silica core gold shell nanoparticle. [49] It can be seen that the core shell structure has extremely agile LSPR tunability and thus their optical properties can be systematically designed for extensive applications.

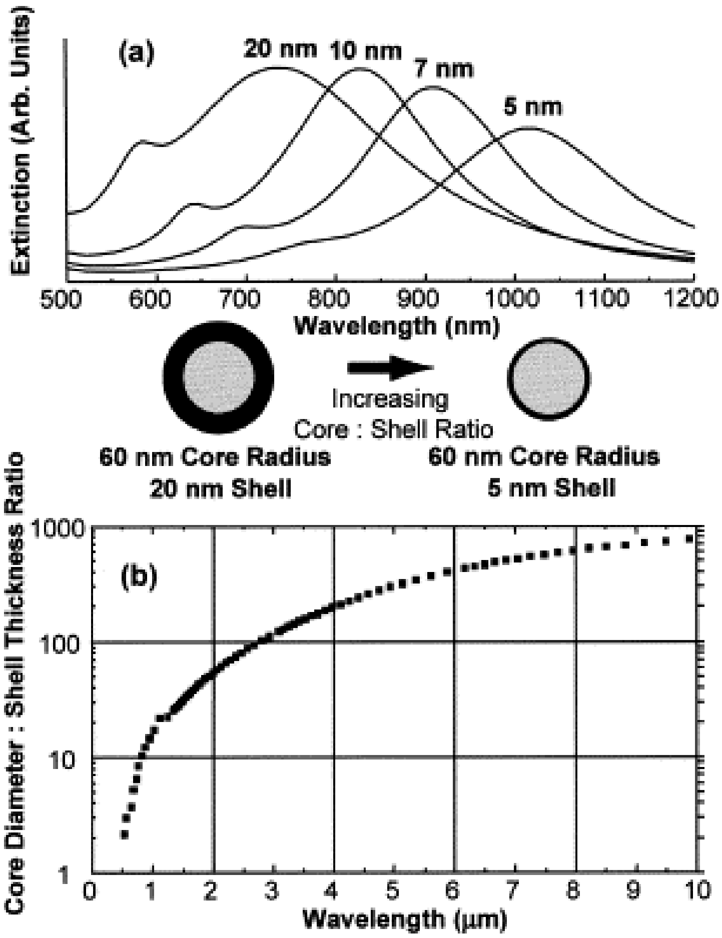

Figure 12 Calculation of optical resonance wavelength versus the ratio core radius and shell thickness. (Reproduced with permission from 49. Copyright 1998 Elsevier.)

Therefore, due to the excellent optical resonance properties, core shell structures can serve as constituents in a new class of materials that are capable of uniquely controlling radiation in the visible or IR spectral regions. However, the common exhibiting resonances of these core shell materials are primarily in the visible spectrum, mainly focused on the 400~600nm.[47, 48] Therefore, the extension of these resonances to the red and even IR regime still needs comprehensive investigation. In this proposal, combined with application of solar light and IR sensing, we have tried to core shell structures using silica spheres with the diameters of 100nm and 1300nm, respectively. As can be seen in Figure 13, the simulation expected the selection wavelength from 400nm to 1500nm, which fully satisfied our requirement.

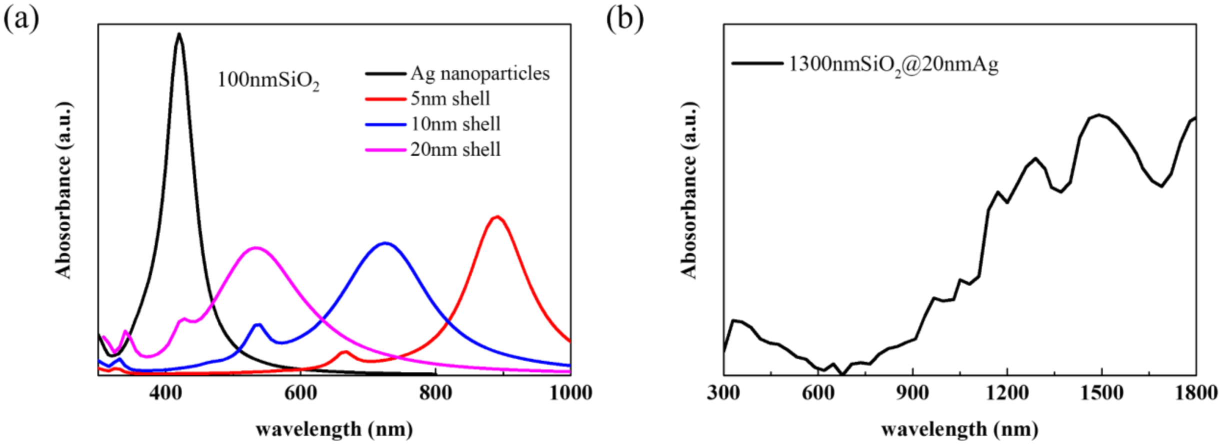

Figure 13 Mie scattering theory of spectra for various silica cores: (a) 100nm and (b) 1300nm.

1.3.2 Plasmon Enhanced Solar Cells

As we mentioned previously, PSC devices hold great promise as cost-effective renewable energy sources but still require a higher PCE for the future industrial applications. The primary mechanism lied behind this drawback is the incomplete photon absorption and utilization. Not only perovskite based solar cells, but other solution-processing thin-film solar devices like organic solar cells (OSCs) also suffer from insufficient solar light harvesting. Aim to realize the full potential of the solar cell devices, incorporation of plasmonic metal structures into the thin active layers has been considered as a breakthrough strategy to solve this inherent limit and represent an imperative milestone toward the highly efficient PSCs and OSCs, arising from the significantly enhanced light absorption and electrical characteristics in fundamental.[53, 54]

The light coupling effect of plasmons in the active layers can be complicated and reports have even shown controversial results. Typically, Xu, Wand and their colleagues have embedded a core-shell plasmonic nanostructure into both active layers of OSCs and PSCs.[55] Specifically, Ag nanoparticles were decorated with a titania/benzoic-acid-fullerene bi-shell (Ag@TiO_2@Pa), enabling the nanoparticles to be compatible with fullerene acceptors or a perovskite absorber, as can be seen in Figure 14. Moreover, coating the Ag@TiO_2 nanoparticles with a fullerene shell can activate efficient plasmon-exciton coupling and eliminate the charge accumulation, thus facilitating exciton dissociation and reducing the monomolecular recombination. The improved light absorption and enhanced carrier extraction of devices with Ag@TiO_2@Pa nanoparticles are responsible for the improved short-circuit current and fill factor, respectively. On the basis of the synergistic effects (optical and electrical), a series of plasmonic OSCs exhibited an enhancement of 12.3-20.7% with a maximum power conversion efficiency of 13.0%, while the performance of plasmonic PSCs also showed an enhancement by 10.2% from 18.4% to 20.2%. This core-shell design concept of plasmonic nanostructures demonstrates a general approach to improving the photovoltaic performance with optical and electrical contributions.

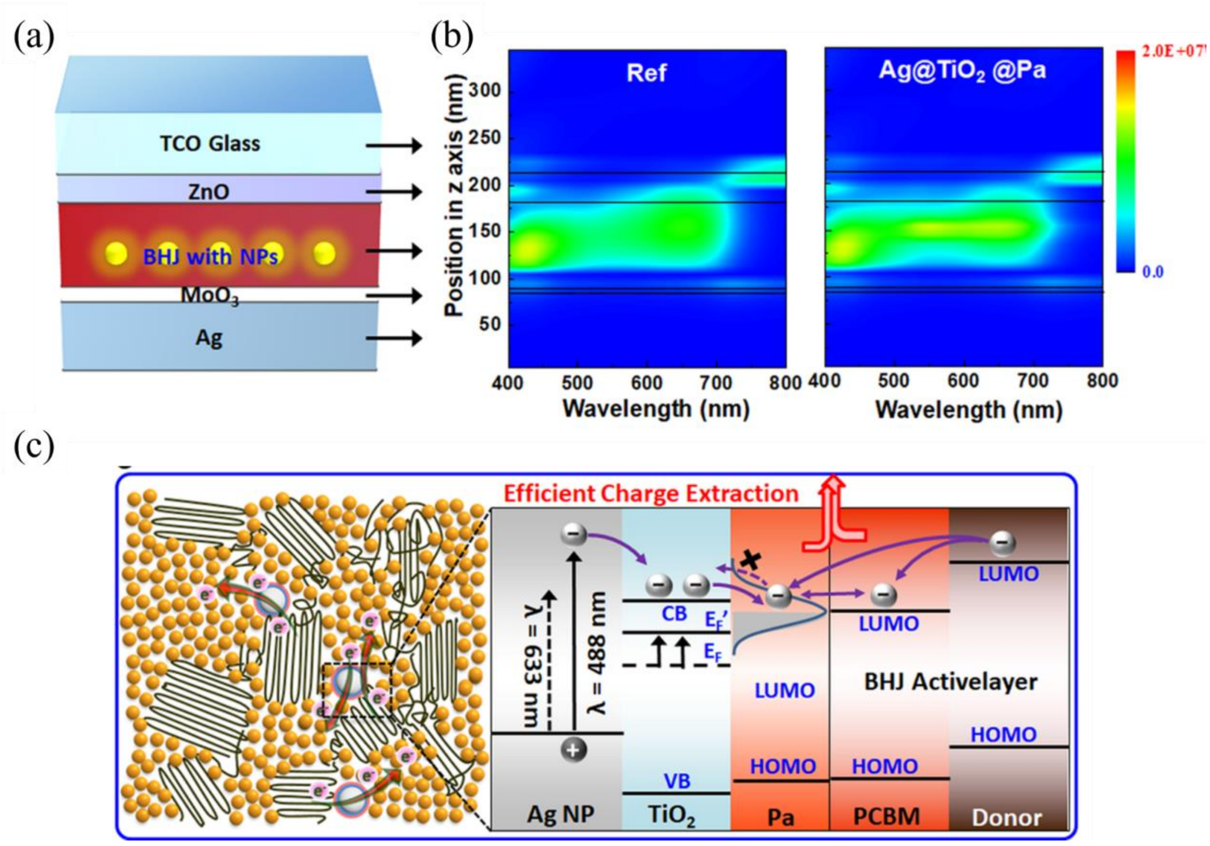

Figure 14 (a) Plasmonic device structures of OSCs, (b) variation of absorptive power distribution due to plasmonic incorporation and (c) energy diagram of the proposed charge extraction process. (Reproduced with permission from 55. Copyright 2019 American Chemical Society.)

The rise of the optical and electronic effects can be attributed to LSPR effects in metal structures, giving rise to a collection of optical and electronic effects which occurred during the excitation and subsequent decoherence of a plasmon. Accordingly, plasmonic enhancement in solar devices can be attributed to radiative and nonradiative effects as can be seen in Figure 15.[56] For the radiative part, the LSPR relaxes and re-radiates light into the absorptive layer or the metal nanostructures act as a secondary light source that enhances local electric fields including light scattering and near field enhancement, and the non-radiative effects are where the LSPR relaxes and energy is subsequently transferred to vicinal semiconductor which can be divided into hot electron transfer and plasmon resonant energy transfer.

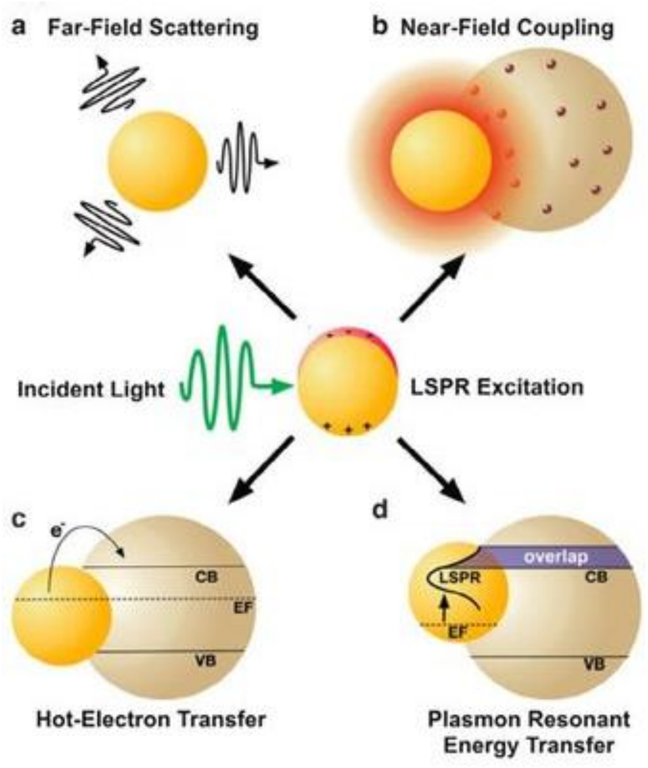

Figure 15 Schematic of plasmonic effect in perovskite solar cells a: far-field scattering, b: near-field coupling, c: hot-electron transfer and d: plasmon resonant energy transfer. (Reproduced with permission from 56. Copyright 2016 Royal Society of Chemistry.)

1.3.3 Other applications

Based on our previous discussion, it can be predicted that the graphene IR absorption can be enhanced by the silica core silver shell particles. Therefore, we have designed a graphene biometric sensor integrating red silica core silver shell particles based on thermoelectrical and biometric mechanisms, as can be seen in Figure 16. By coating plasmonic particles on the suspending graphene grown by CVD, the temperature of the effective area of device can be increased rapidly and thus reflect the incident light. Silica core silver shell particles can contribute to local temperature increment rapidly. The TCR of graphene is complicated and heavily influenced by the environment, suspending structure are taken here to maximally convert incident photons to heat. The photodetectors were fabricated on a highly conductive Si wafer (p-type) and the suspend membrane consists of graphene and SiN as shown in Figure 16 (The graphene effective area is 5*5mm^2 to counteract the dissipation of heat due to the large heat conductivity of graphene).

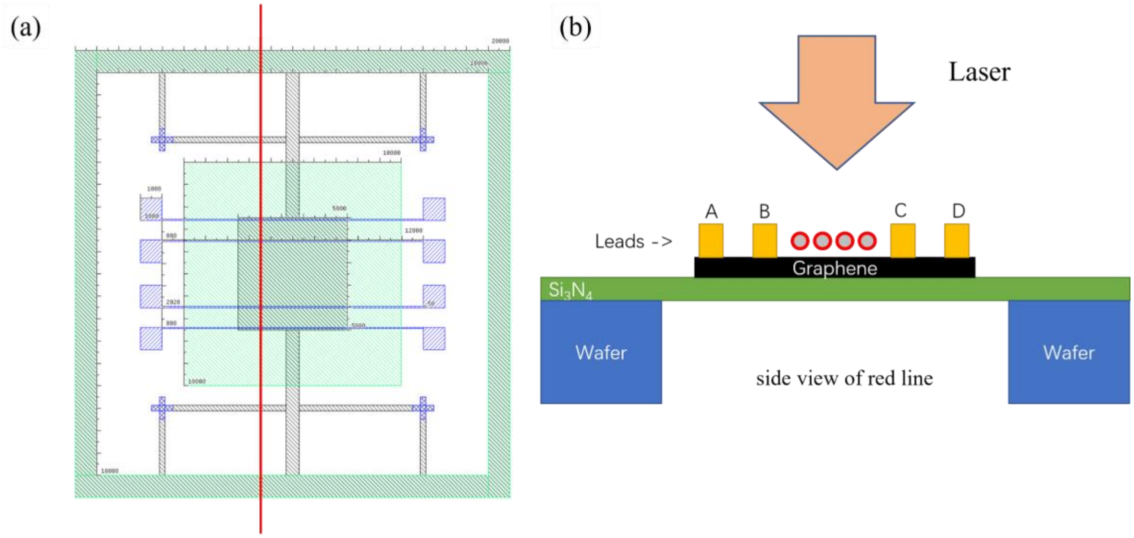

Figure 16 Schematic illustration of graphene photodetector. Green: Membrane (10*10mm^2) Black: Graphene (5*5mm^2) Blue: Leads/Contacts (1*1mm^2).

We have run tests on the device, as can be seen in Table 1. The graphene sensors are coated with plasmon and under the shining of the red diode (λ=618nm), the resistance of the device decreased by 1.24% which the reference sensor didn't show the change under laser at all. In the future, more device measurement will be conducted under the different laser to confirm the selection of the detector by plasmon.

Table 1 Initial Testing of Graphene based Sensors

		Potential (V)	Current (A)	Resistance (Ohm)	
W/O	Control	0.2	1.09E-04	1.83E+03	null
	Lighten	0.2	1.09E-04	1.83E+03	
W	Control	0.2	8.28E-05	2.41E+03	-1.24%
	Lighten	0.2	8.41E-05	2.38E+03	

Sensors relating to gas (H_2, CO_2), temperature, and pH value based on optical fiber are gaining attention because of their higher sensitivity.[57] Attributed to the higher refractive index of the TiO_2 compared to that of silica core, the TiO_2 layer can also be the sensing layer with optical fiber sensors.[58] Moreover, atomic layered deposition (ALD) is a vapor phase deposition technique based on successive, alternating surface controlled and self-limiting reactions to produce highly conformal and uniform thin films with thickness control.[59] Hence, ALD has emerged as a powerful tool for many industrial and research applications. Moreover, the ALD TiO_2 films are more stable than SiO_2 and can resist high temperature environment.[60] However, there is still lack of knowledge about the gas sensing of ALD TiO_2 films with optical fibers. Thus, in this proposal, we are going to apply ALD TiO_2 layers with different thickness as sensing layer under different temperature. NIR gas sensor using ALD TiO_2 films on optical fibers are used. For further enhancing the IR response, IR plasmonic particles will also be coated on the optical fibers for less attenuation. The schematic of the optical fiber sensor and set-up are shown in Figure 17. Moreover, the coating of the particles, the thickness of TiO_2 films and the using temperature will be investigated for better understanding the mechanism of gas sensing.

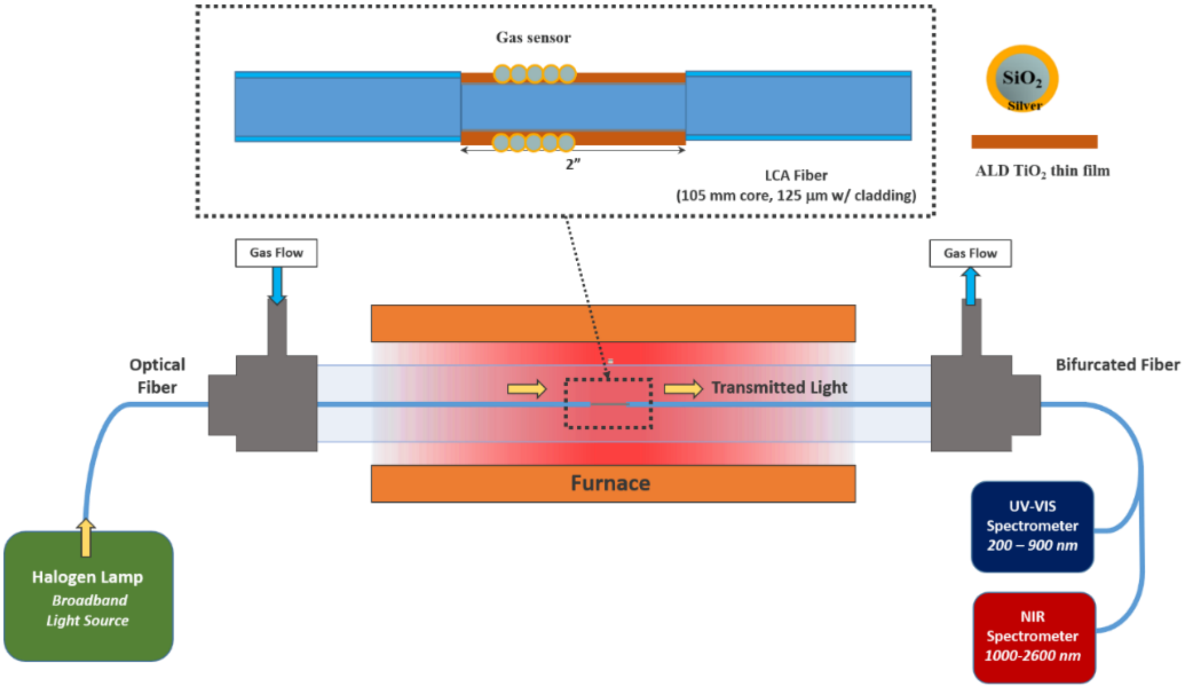

Figure 17 Schematic of Gas Sensor based on Plasmon Enhancing Optical Fiber.

NIR plasmon particles were achieved with the 1400nm diameter Silica coated with a 20nm silver shell. As-synthesized particle solution using ethanol solvent possessed a sharp peak at 1400nm, consistent with the simulation result in Figure 13b. Then the particles will be coated on the silica plate and 10nm ALD TiO_2 deposited fiber via dip coating method.[61] As can be seen in Figure 18a, there is a broad but prominent peak for the silica plate around 1300nm. Although there is a slight blue shift, compared with solution, the effect can be ascribed to the media difference for the particle and also some aggregation.[62] However, it can be concluded that the successful transfer of the enhanced NIR absorbance effect. Therefore, the transmission spectrum of NIR plasmon particles coated film on fiber was then acquired in 100ºC increments from 100-800ºC and at each temperature step, the system was stabilized for 5 minutes prior to the acquisition of a transmission spectrum. These spectra are presented in Figure 18b, all relative to the initial transmission spectrum at 25°C. From room temperature to 500ºC, it can be seen that the transmission spectrum is dominated by a broad absorption feature at a 1400nm-plasmonic wavelength that gradually grows with increasing temperature. Prior work with only ALD TiO_2 layer didn’t show such enhancement at this range from data presented in 63. After performing the temperature series, the fiber was held at 800°C in 3.9% H_2 and varied levels of hydrogen as shown in light blue in Figure 18b. The relative change of transmission intensity is shown for a range of different wavelengths in the NIR (Figure 18c). During the second cycle of hydrogen exposure, a measurable broad NIR response was observed. More specifically, at 1100 nm a peak response of around 1% relative to the baseline, as shown in Figure 18d. However, it seems that the NIR particles are not very stable in the high-temperature atmosphere which requires more complex design and assembly. Detachment may happen because of stress mismatch caused by the TiO_2 phase transformation. And for more stabilized NIR particles, a protective layer such as a thin silica outer shell should also be considered.

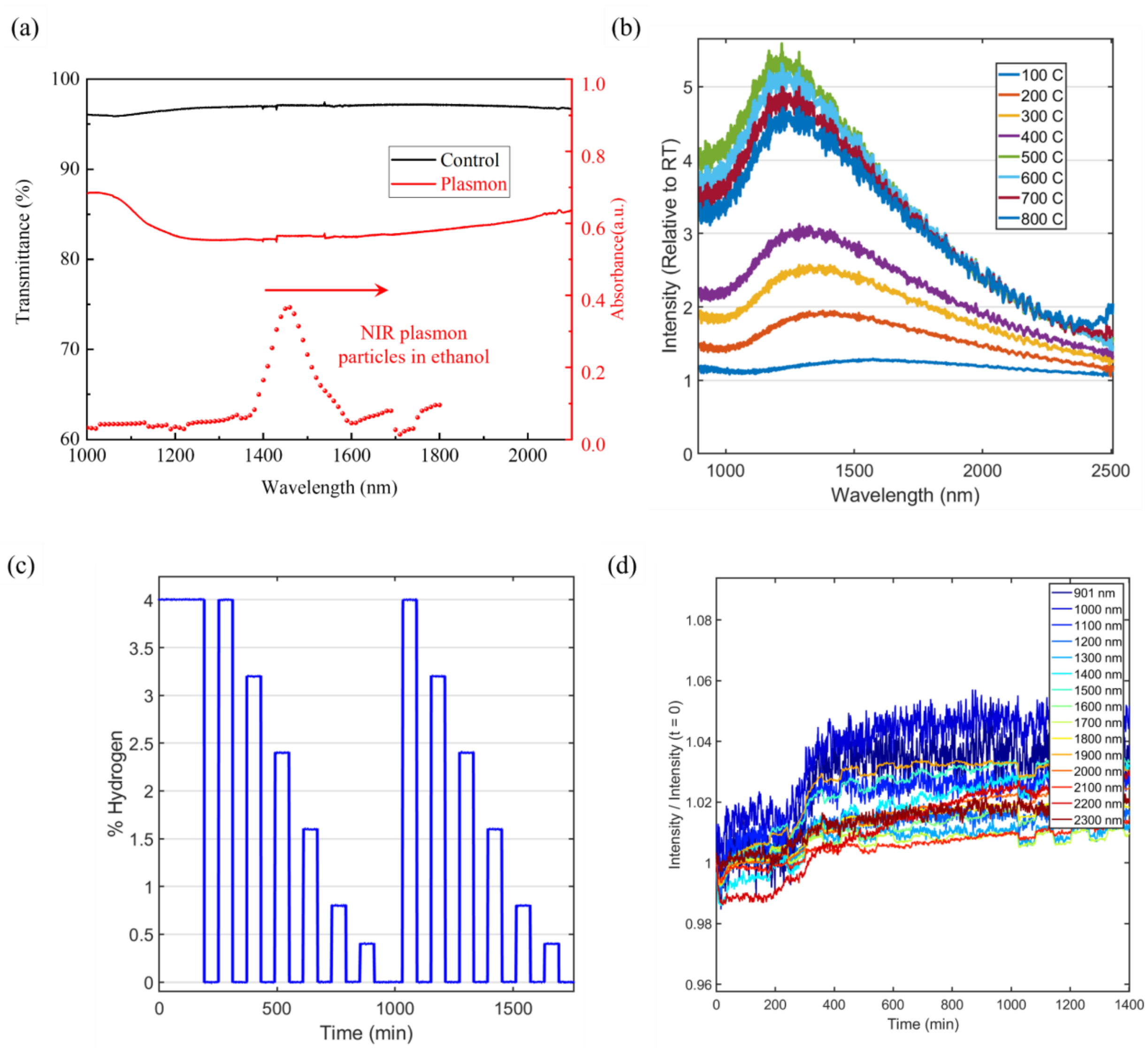

Figure 18 Transmittance spectra of (a) silica plates with (red line)/without (black) NIR plasmon coating and paticle solution dispered in ethanol (right) and (b) TiO_2-based fiber coated with NIR plasmonic particles. (c) Hydrogen cycled from 3.9% to 0.4% and (d) corresponding optical response of plasmon fiber sensor at 800ºC.

1.4 Hydrogen Evolution Reaction

1.4.1 Solar-driven HER

Solar energy is an inexhaustible natural energy source and to fully take advantage of it, the extension and combination with other industry technology is indispensable. Moreover, it has also been mentioned that the prominent obstacle encountered in solar technology is a massive grid-scale storage system to store the converted electrical energy, so as to compensate for the intermittent nature of sunlight. As an alternative to PV cells, photoelectrochemical PEC system utilizes a solid/liquid junction by immersing a semiconductor material into an electrolyte. PEC cells offer the advantage of producing chemical fuels such as hydrogen (H_2) through splitting of water and thereby provide an alternative pathway to store solar energy at a large scale in the form of chemical bonds. Hydrogen energy is compatible with the current industry systems and has the highest energy density (143MJ/kg), far higher than methane. Electrolysis powered by grid electricity is disadvantaged by the limited number of hours of low-priced electricity. The future production of hydrogen for energy purposes will be dominated by electrolysis using dedicated off-grid renewables, such as solar and wind farms. In the presence of sunlight, water is split into its constituting atoms at the photoanode and cathode.

A typical photoelectrochemical (PEC) cell for hydrogen evolution reaction (HER) is illustrated and shown in Figure 19a.[64] As can be seen, the fundamentals of the kind of devices to transfer the solar energy to the reduced H_2. In HER, photosensitive materials are treated as cathodes. The photocathodes can absorb light, and then produce photoexcited electrons and negative voltage bias. The H^+ flows towards the cathode in the solution while the electron flow towards the cathode in external circuit to complete a closed loop. The reduction reaction can then occur on the surface of photocathode electrodes, which are also the catalyst materials for the HER. Actually, the HER is half of water splitting:

in acidic electrolytes:

$$2H_{(aq)}^{+} + 2e^{-} \rightarrow H_{2(g)} \tag{1-7}$$

in alkaline electrolytes:

$$2H_2O + 2e^{-} \rightarrow H_{2(g)} + 2OH_{(aq)}^{-} \tag{1-8}$$

Thus, solar-driven HER process requires that the cathode catalytic materials can absorb sunlight and then transfer solar energy to hydrogen. Therefore, transition metal oxides and sulfides with proper energy band structures are often chosen as photocatalytic electrodes as shown in Figure 19b. These semiconductors can absorb light as the electrons in valence band (VB) jump into the conductive band (CB) ($h\nu > E_g$). And then the photoexcited electrons can participate in HER.[65] Thus, the materials should possess proper bandgap value which allows maximal sunlight absorption and hydrogen production. The CB electron energy level should be more negative than the H^+/H_2 reduction potential, ensuring enough energy to overcome the activation energy barrier.[64]

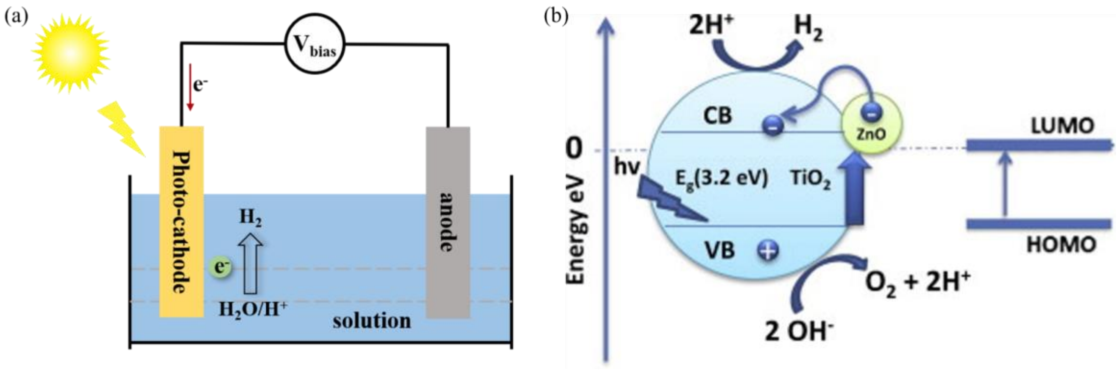

Figure 19 (a) Schematic illustration of a typical photocatalytic device and (b) working principle of TiO_2 photocatalytic water splitting. (Reproduced with permission from 66. Copyright 2012 Elsevier.)

In the cathodic reaction, as shown in Figure 19b, H ions or H_2O capture electrons and thus can be reduced to H_2. This reducing process requires activation energy (E_{act}), as can be seen in Figure 20.[64] The height of the E_{act} is largely depending on the interface of the reactants and catalysts. Thus, the function of catalyst is to maximally reduce this energy gap. The catalytic hydrogen reduction process can be divided into two primary steps. In acidic electrolytes, firstly, the H ions in the solution are absorbed on the surface of catalyst cathodes and reduced by an electron, fascinating to produce reduced hydrogen. Then, the producing H_2 needs to be desorbed from the catalysts.

$$H_{(aq)}^{+} + e^{-} \rightarrow H_{ads} \tag{1-9}$$

$$2H_{ads} \rightarrow H_{2(g)} \tag{1-10}$$

Since these two processes are adverse in thermodynamics, catalyst materials that have a significant decrease of Gibbs free energy in one process must have difficulties completing the other one. Thus, thermal neutral catalyst materials are ideal for the HER, meaning the ΔG_{H*} should approach zero. The interaction between catalysts and hydrogen should not be too weak or strong.[67] Besides, according to Norskov's theory, the more neutral adsorption/desorption of hydrogen, the higher exchange current can obtain in the reducing process.[68] Based on this criterion, Pt and its alloys are the optimal choice for HER due to their excellent catalytic activity and high exchange current during the catalytic reducing process. However, Pt is a noble metal and the content on the earth is quite rare. It is unrealistic to commercialize on a large-scale. Thus, the development of a cheap and excellent catalyst electrode is very important.

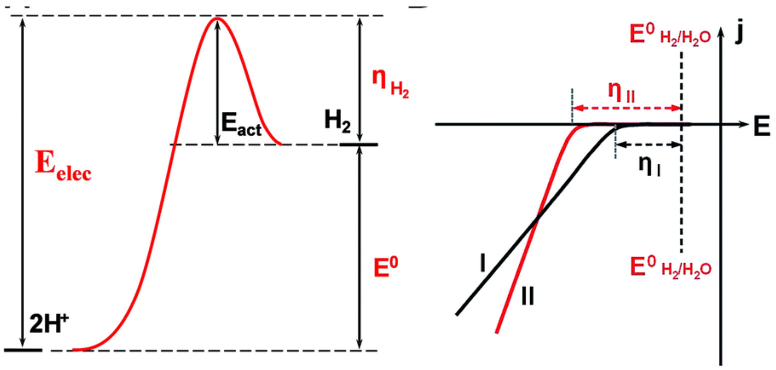

Figure 20 Schematic illustration of the HER energetics (Reproduced with permission from [64]. Copyright 2013 Royal Society of Chemistry.)

1.4.2 OMH Perovskite for PEC applications

Numerous studies focusing on the improvement of photoelectrode materials. However, it can also easily be noticed that most transition oxide and sulfide semiconductors possess a relatively small bandgap, resulting in their absorption range located in the UV range, which is only around 9% of the solar light. Hybrid perovskites are promising PEC materials which hold merits that are typically absent in the conventional inorganic semiconductors. Other than their tunable electronic properties but suitable bandgaps can absorb most visible and NIR portion of the solar energy. In the perovskite-based PEC hybrid configuration, hybrid perovskite solar cells are used as additional light absorbers, combining with typical photoelectrodes and extending the light absorption wavelength to the IR region.[69] In this design, perovskite solar cells normally sit behind the photoelectrodes and absorb the sunlight that penetrates through the front photoelectrodes, thereby greatly enhancing the sunlight utilization. At the same time, perovskite solar cells can provide photovoltage over 1V, facilitating the photoelectrodes to achieve unbiased water splitting on their surfaces.

2.0 Research Hypothesis and Scope

Based on the statement of the importance of solar energy industry and review on the solar cell system development, this research is expected to make progress on the promotion of PSC devices improvement including their PCE, stability as well as the light management and carrier dynamic optimization. Further, we have extended the application of the OMH materials into the water splitting application and hope this can contribute to the evolution of solar energy storage and renewable technologies.

2.1 Chapter 3: Effect of NIR Plasmonic Particles on PSC Device

It has been discovered that the incomplete utilization of IR or NIR solar portion is one of the main obstructions for perovskite based solar devices to achieve theoretical performance. Long-wavelength photons possess relatively low energy lying on the electric band edge of the OMH. Therefore, both corresponding absorption and photon-generated carriers in the perovskite based active layer are weak in this range. Though there have been several research focused on the plasmon enhancing perovskite optoelectrical devices including PSCs, the improvement focused on the near-band edge solar energy utilization is still off the table. Herein, NIR plasmon enhancing PSC structures aimed at the near-band edge light harvesting strengthening have been proposed:

1. A thin outer layer of semiconductor materials can passivate the direct contact of metal and OMH materials and avoid parasite reactions which may destroy the PSC layers.

2. Investigation of plasmon PSC device structure with particle embedding position and concentration can optimize the plasmon enhancement effect on optical and electrical performance of the final devices.
3. The selective enhancement in the NBE range of the PSC devices can be proved by IPCE measurement, wavelength-depended electric field calculation and photoluminescence (PL)/time-resolved PL analysis.

2.2 Chapter 4: Interfacial Modification for SnO_2 based Planar PSC device

Meanwhile, we are devoted to exploiting new types of PSCs with electron transport materials of higher developing potential. As we have mentioned previously, SnO_2, compared with traditional TiO_2, has held more advantages as the ETL material such as a more straightforward fabrication process without high temperature and superior charge transport mobility. However, the solution-process SnO_2 without annealing retains surface defects, inducing massive non-radiative recombination. Herein, a novel interfacial modification strategy using PbS quantum dots between the ETL SnO_2 and $FAPbI_3$ based perovskite active layer has been proposed to fabricate PSC devices with high efficiency and long stability:

1. PbS coating modulates the surface state of SnO_2 and there is a better energy alignment between perovskite and SnO_2 ETL.
2. PbS pre-deposited underlying the PVK, favoring the growth of photoactive perovskite phase.
3. PbS interlayer passivates the interfacial contact defects, reducing non-radiative recombination.

2.3 Chapter 5: Hybrid Perovskite based Photocathode

Further, PSC devices are introduced into solar-driven water splitting systems to fully take advantage of their light absorption and conversion ability. For feasible OMH material based photoelectrodes, the passivation of the device compatible with chemical solvent environment and the assembly of a co-catalyst for efficient electrochemical reactions are two essential issues on the horizon. As we concluded in part 1.4, there is a lack of study and design which bridge the convenient perovskite-based photo-electrochemical devices and high-performance earth-abundant co-catalyst materials. Herein, naturally extended from the previous passivation strategy and progress of noble metal free catalysts, a versatile and nimble hybrid photocathode structure has been proposed and evaluated:

1. Molybdenum carbide (Mo_2C) is a potential catalyst material for hydrogen evolution reaction (HER) due to its low value of ΔG_H. The synthesized Mo_2C nanomaterials with the structural support of carbon material and single atom Titanium (Ti) element dopant can considerably decrease the HER overpotential for more effective electron transfer and the decrease of the ΔG_H.
2. Commercial metal (Ti) foil can be assembled on the top of inverted PSC devices with silver paste at the room temperature. The Ti foil can act as a conductive layer for long stability protection. Meanwhile, Ti foil is electrochemically stable and thus can be the substrate for the cheap catalytic nanomaterials which connect the catalytic part for the PSC devices for the final photocathode devices.
3. The enhancing HER performance of Mo_2C based catalytic material can be tested using LSV, ESCA and impedance spectra measurements. Moreover, the performance and

stability of the final hybrid perovskite-based photocathode with Mo_2C based co-catalyst can also be demonstrated correspondingly.

3.0 Near-Band-Edge Enhancement in Perovskite via Surface Plasmons

This Chapter includes the following published contents:

Liu, Y., Lee, S., Yin, Y., Li, M., Cotlet, M., Nam, C.-Y., Lee, J.-K., Near-Band-Edge Enhancement in Perovskite Solar Cells via Tunable Surface Plasmons. Adv. Optical Mater. 2022, 2201116. https://doi.org/10.1002/adom.202201116

(Full text reproduced with permission from 70. Copyright 2022 Wiley-VCH GmbH.)

3.1 Background and Motivation

Solution-based organometal halide perovskite solar cells (OMH PSCs) has attracted continuous attention since past decade due to their proper bandgap (~1.6 eV), high absorption coefficient, long carrier diffuse length, low-cost solvent engineering, and compositional flexibility.[17, 71, 72] However, practical future applications of the PSCs still require further improvements of their performance, such as power conversion efficiency (PCE), stability, and compatibility with other types of photovoltaics for a high-efficiency tandem application. Therefore, numerous efforts have been made to improve CH_3NH_3 (MA) or $CH(NH_2)_2$ (FA) based PSC devices. For instance, the hole and electron transport layers (HTL and ETL) are modified, an interface layer is inserted for favorable energy level alignment, pre- or post-treatment of the active layer is tested, and antisolvent and stabilizer are added into the perovskite layer.[54, 56, 73] Such optimizations are expected to enhance the light absorption and/or carrier dynamics of the devices.[30]

There is a simple and versatile method that can enhance the light absorption and manage the carrier transport simultaneously which is the insertion of plasmon particles into the solar cell device structures. The embedded metallic structures can confine the electromagnetic (EM) field via the localized surface plasmon resonance (LSPR) effect and act as effective light-matter interaction centers inside the solar cells and the optical and electric properties of the solar cells to increase the PCE.[54]

Tunable metal plasmonic particles have been applied into PSCs of different device configurations and the contribution of LSPR to the improved PCE is explained using radiative and nonradiative aspects.[53, 56, 73, 74] For example, Huang et al. have demonstrated that the Au@Ag nano-cuboids in the different layers of PSCs can increase PCE via LSPR enhanced light absorption and optimized scattering management.[75] Moreover, the incorporation of plasmonic particles are also claimed to be able to change the carrier dynamics, which include reducing exciton binding energy,[76] suppressing the electron-hole recombination,[53, 77, 78] and increasing the carrier collection efficiency at the interface.[54] Nevertheless, potential negative effects of integrating plasmonic particles are non-negligible, posing challenges against the plasmonic enhancement. A high particle density in active layer can reduce perovskite loading and metallic surface may degrade under a high process temperature or corrosive solvent, which causes a detrimental impact on charge transport.[75] Due to this complex effect on the light absorption and charge collections, delicate design of the plasmon PSC structure (e.g., shape, position, passivation) is required.[55] Accordingly, previous studies report the use of different types of plasmonic particles inserted in a few different locations within the device. For example, gold nanoparticles embedded into the HTL can cause a considerable improvement of photocurrent resulting from a metallic plasmonic contribution. Huang et al. exploited the insertion of titania/benzoic-acid-fullerene shell decorated Ag nanoparticles into the perovskite layer to enhance light absorption and carrier extraction through the synergistic combination of electric and optical effects.[55]

However, most of these previous studies exploited spherical Ag or Au based plasmonic nanoparticles usually exhibiting narrow plasmonic excitation bands centered at high-energy zone (300~550 nm) to boost the efficiency of solar cells, which overlap with the strong extinction zone of the organic-inorganic metal halide perovskites. Thus, the plasmonic light enhancement effect is become less important and the relatively low long-wavelength absorption of the active material is not addressed. As shown in Figure 21, Lee et. al. recently embedded gold nanoparticles into the hole transfer layer (HTL) of PSC to improve the properties.[76] However, based on the absorption check of the whole device, it is noticed that the dominate contribution to the low-energy zone of plasmonic PSCs is the enhancement of electrical conductivity of the HTL rather than plasmon-induced absorption enhancement.

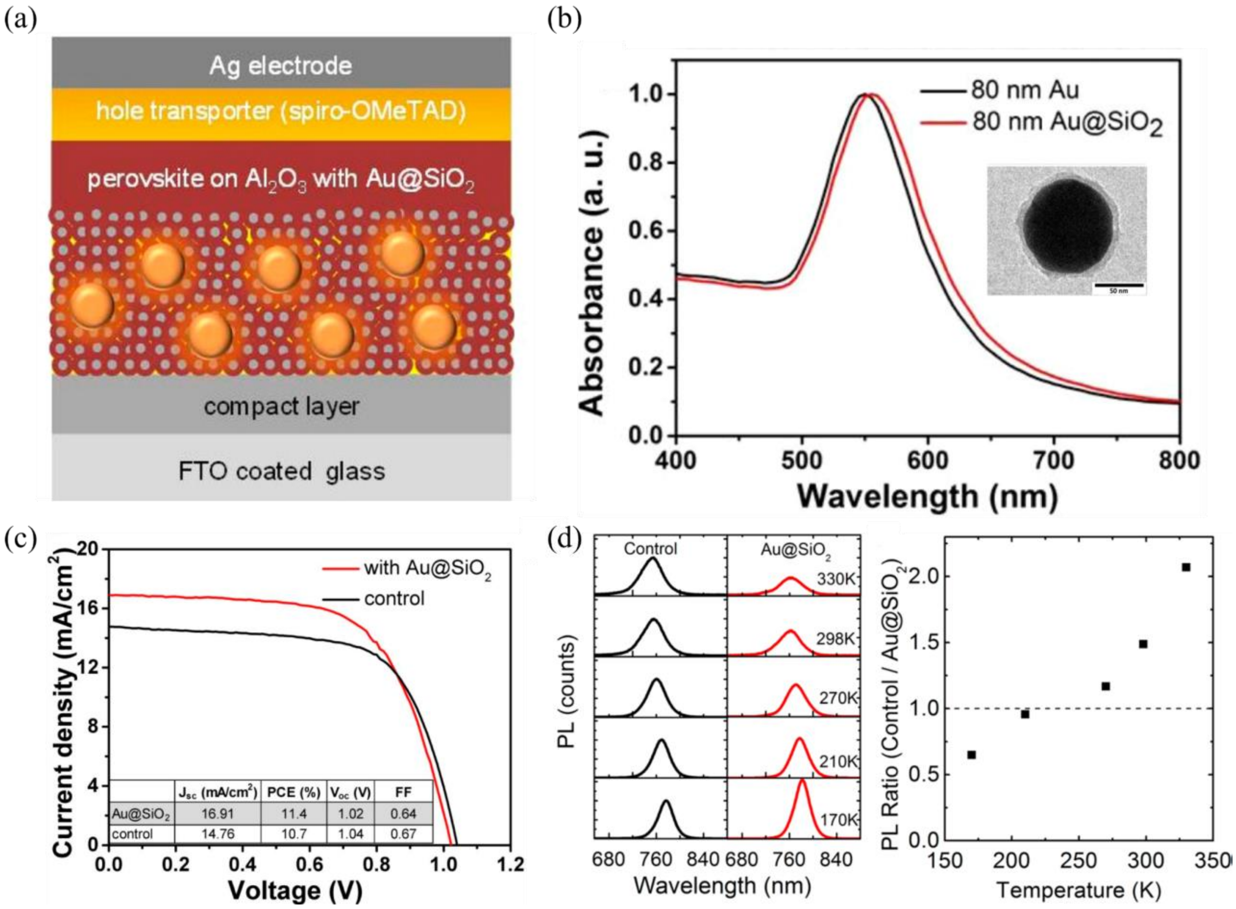

	J_{sc} (mA/cm^2)	PCE (%)	V_{oc} (V)	FF
Au@SiO_2	16.91	11.4	1.02	0.64
control	14.76	10.7	1.04	0.67

Figure 21 (a) Illustration of device structure with plasmon particles, (b) UV-Vis spectra of plasmon particles, (c) *J-V* curves and (c) temperature dependence of PL spectra and (d) corresponding ratio with and without plasmons. (Reproduced with permission from 76. Copyright 2013 American Chemical Society.)

As to the material choice used for plasmonic particles in PSCs, most studies chose Ag or Au based plasmons exhibiting LSPR bands in a visible range (400 < λ < 600 nm), where the light extinction coefficient of the halide perovskite is already large. Given that the light extinction coefficient is small near the near-band-edge (NBE), it would be of great importance to explore the NBE light management of the halide perovskite by modifying the physical structure of the plasmonic particles.[75] This near-infrared (NIR) light possesses low photon energy and interacts with the halide perovskite weakly, resulting in the weak light absorption and low carrier extraction rate.[75, 76] In this regard, it would be beneficial to explore the science-guided design of new surface plasmonic particles, which can boost the performance of PCSs in the NIR region corresponding to weak absorption NBE region. It is particularly necessary to thoroughly investigate the impact of these new NIR plasmonic particles on both the optical and charge transport properties in PSCs.

To achieve this goal, we have studied a SiO_2@Ag@Ag_2S (SAA) sandwich plasmonic shell particles whose LSPR wavelength is positioned in NIR region to strengthen the light-matter interaction at NBE of the halide perovskite ($600 < \lambda < 800$ nm). Ag shell on silica cores with a diameter of 100 nm is employed for the redshift of silver plasmons.[52, 79] Ag_2S layer is coated on the Ag shell by reacting the outer surface of Ag layer. This top Ag_2S layer prevents the trapping and annihilation of carriers at the interface between the Ag shell and the surrounding halide perovskite matrix.[80] SAA particles are added into different locations of PSCs and their effects on PCE are comprehensively examined. It is found that the plasmonic particles within the perovskite layer improves the performance of PSCs the most. There is an optimum amount of embedded plasmonic particles which increases the light absorption while suppressing the carrier recombination simultaneously. This synergistic combination of the two effects significantly boosts the photon-to-charge carrier conversion in NIR range without sacrificing the open circuit voltage (V_{OC}) and fill factor (FF) of the PSC devices. Consequently, in comparison to conventional PSCs, the surface plasmons increase the quantum efficiency of PSCs in the NIR region by 15% and the champion plasmonic device reaches short-circuit current density (J_{SC}) of 24.7 mA/cm^2 and PCE of 19.83%.

3.2 Experimental

3.2.1 Synthesis of SiO_2@Ag Core@Shell particles

Silica (SiO_2) nanoparticles were synthesized by Stöber method.[81] Ethanol was mixed with 9 ml ammonium hydroxide solution. Then, 4.5 ml TEOS was added into the solution and vigorously stirred for 24 hours at room temperature. Then, obtained SiO_2 particles and 1 ml APTMS were put in a three-neck bottle and distilled at 80^{o}C overnight twice. The diameter of monodisperse silica particles was 100 nm (Figure 22a).

A thin and uniform Ag shell was coated on the surface of SiO_2 by seed mediated Zsigmondy method. The silica-gold seed solutions were first prepared for silver shell coating. Typically, 1.5 ml 0.2 M NaOH solution and 1ml THPC solution were added into 45.5 ml water and stirred for 5 min. 2 ml $HAuCl_4$ solution was injected into it very quickly. Subsequently, SiO_2 nanoparticles were added dropwise (Figure 22b). The gold-decorated silica particles were mixed with a fresh 0.15 mM solution of $AgNO_3$ and stirred vigorously.

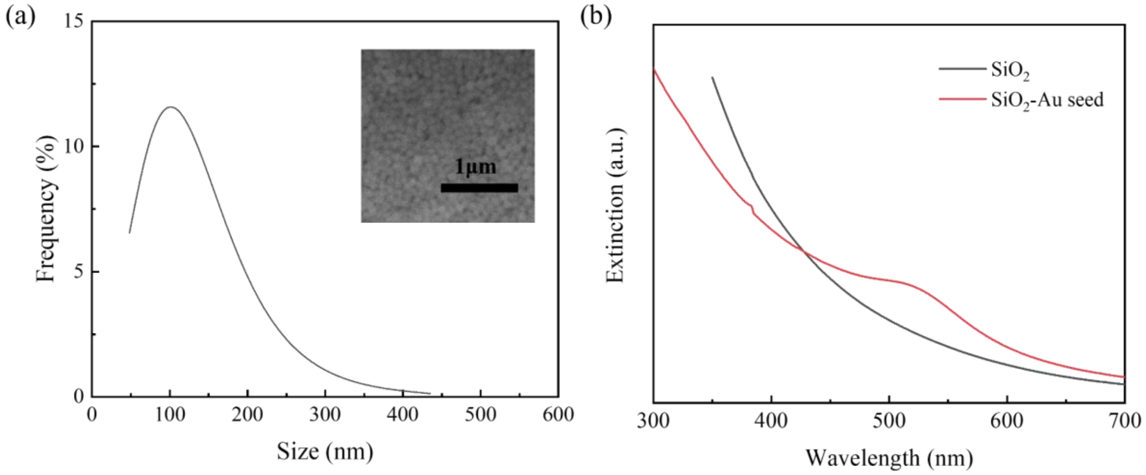

Figure 22 (a) DLS distribution of SiO_2 core nanoparticles (average size; 106.8nm) and (b) UV-vis extinction spectra SiO_2 and Au seed nanoparticles decorated SiO_2 particles.

Then, 50 ml of formaldehyde solution was added to the stirred mixture to reduce silver onto the gold-decorated silica particles. This step was followed by adding ammonium hydroxide (typically 20~50 ml). Color of the solution changed between 30 and 60 s, which is the evidence of shell formation. The addition of ammonium hydroxide into the sample solution caused a rapid increase in the pH of the solution, which facilitated the reduction of Ag^+ to Ag^0 that was deposited onto the surface of the seed particles, forming silver shells. The surface of SiO_2@Ag core-shell particles was passivated with Ag_2S film. For the deposition of a thin sulfide nanoshell, the core-shell particles were redispersed in a 0.5 M Na_2S solution and the solution was continuously stirred for 2 hours at room temperature. During the stirring, 3 nm thick Ag_2S layer was slowly formed on the surface of Ag shell. The resultant SAA particles were washed in ethanol and separated via centrifugation. The collected SAA particles were kept in a vacuum overnight to completely dry the solvent before they were further used. For the fabrication of plasmonic PSCs, different amount of the SAA particles were dispersed in DMF and added to the different locations of PSCs.

3.2.2 Mesoporous PSC Fabrication

Perovskite Solar Cell Fabrication: A compact TiO_2 (c-TiO_2) layer was deposited on FTO glass substrates by spin coating the mixture of TTIP and 1-butanol at 3000 rpm for 30 s. The densely coating layer was heated at 150 °C for 10 min in the ambience. TiO_2 paste dispersed in ethanol (1:4 w/w) was spin-coated at 4000 rpm for 30 s on the c-TiO_2 layer and annealed at 500 °C for 1 hour. To prepare the perovskite layer with or without SAA, 159 mg MAI and 469 mg PbI_2 were first dissolved into a mixture solvent of DMSO and DMF (1:8 v/v). Then, 50 μL of precursor solution with or without SAA was dripped onto meso-TiO_2 layer and spun at 4000 rpm for 20 s. After the coated precursor was spun for 9 s, 0.5 ml diethyl ether was dropped using a pipette. The film was then annealed on a hot plate at 60 °C for 3 min and 100 °C for 20 min sequentially. Spiro-OMeTAD solution, which was prepared by mixing 72 mg/ml of Spiro-OMeTAD in chlorobenzene with 28.8 μL of t-BP and 17.6 μL of Li-TFSI salt (720 mg/ml in acetone) was deposited on top of the perovskite layer at 4000 rpm for 30 s as HTL. Finally, 50 nm-thick Au electrodes were thermally evaporated.

3.2.3 Material Characterization

Characterizations and Measurements: The microstructure of the devices was analyzed using scanning electron microscope (FEI Apreo SEM). The crystal structure was examined using X-ray diffraction (XRD; Bruker D8 Dsicover SRD). A radiation source was Cu Kα radiation (λ = 0.15406 nm). Photovoltaic properties were measured using an electrochemical workstation (CHI660D, CHI).

3.2.4 Device characterization

Photocurrent density-voltage (*J-V*) curves were measured under one sun illumination with a basic FTO/ETL/perovskite/HTL/Au structure. The external quantum efficiency (EQE) or incident-photon-to-current efficiency (IPCE) was measured in a direct current (DC) mode without an external bias using TracQ Basic Spectroscopy Instrument.

3.2.5 Static and Time-Resolved Photoluminescence Spectra

Photoluminescence (PL) spectroscopic experiments were performed with a Fluotime 200 spectrometer (time-resolved PL, Picoquant Germany) and an Ocean Optics QE65000 fiber optics spectrometer (steady-state PL) using the 450 and 700 nm pulsed light output from a Pharos/Orpheus OPA/LYRA ultrafast laser system (Light Conversion Systems, 45 kHz repetition rate).

3.2.6 FDTD Simulation

The full-wave electromagnetic simulations were conducted with a commercial Lumerical suite Finite-Difference Time-Domain (FDTD) simulator, which is commonly used to simulate the LSPR of plasmonic nanoparticles. When performing the numerical simulations, the total-field scattering-field source was used to get the extinction cross sections as well as the electric field distributions at the longitudinal and transverse resonant wavelengths. In all calculations, the frequency dependent permittivity of materials was modeled using the experimental data of Johnson and Christy with linear interpolation. The simulation domain was finely meshed with the smallest size of 1.5 nm in the metal region to ensure the accuracy of the calculated results.

3.3 Design and Preparation of NIR Plasmonic Particles

To take advantages of the surface plasmons for better performance of PSCs at the NBE wavelength, several conditions need to be satisfied: 1) to match the LSPR wavelength with the band gap energy of light absorber;[75, 80] 2) to avoid carrier trapping and annihilation at the metal component of the plasmonic structure;[56, 76] 3) to control the positions and concentrations of embedded plasmonic particles to maintain good intrinsic properties of perovskite layer, including high absorption coefficient in ultraviolet-visible (UV-vis) range, long charge diffusion length and so on.[80, 82]

SiO_2@Ag@Ag_2S (SAA) core-shell nanoparticles were prepared through two steps as shown in Figure 23a. A smooth and continuous silver shell was moderately reduced from Ag^1 to Ag^0 assisted by gold seeds.[79, 83] To eliminate the carrier annihilation on the metal surface and stabilize the silver shell, another ultrathin dielectric Ag_2S shell was formed by sulfurating the outer surface of Ag. [84] The details of the plasmonic particle synthesis procedure can be found in the Experimental section. Figure 23b shows the SEM image of as-prepared SAA (SiO_2 core diameter: 100 nm, Ag shell thickness: 17 nm, Ag_2S thickness: 3 nm) core-shell nanoparticles. The extinction spectra of SA and SAA nanoparticles in DMF are shown in Figure 23c. Two curves are similar except a slight difference in the resonance peak wavelength (725 nm vs. 767 nm), which demonstrates that the minor sulphuration of Ag does not change the LSPR of the Ag shell. Optical features at the NIR region were also well maintained. Inset optical photographs in Figure 23c also show that the coating of the outer shell did not change the color of the plasmonic particles.

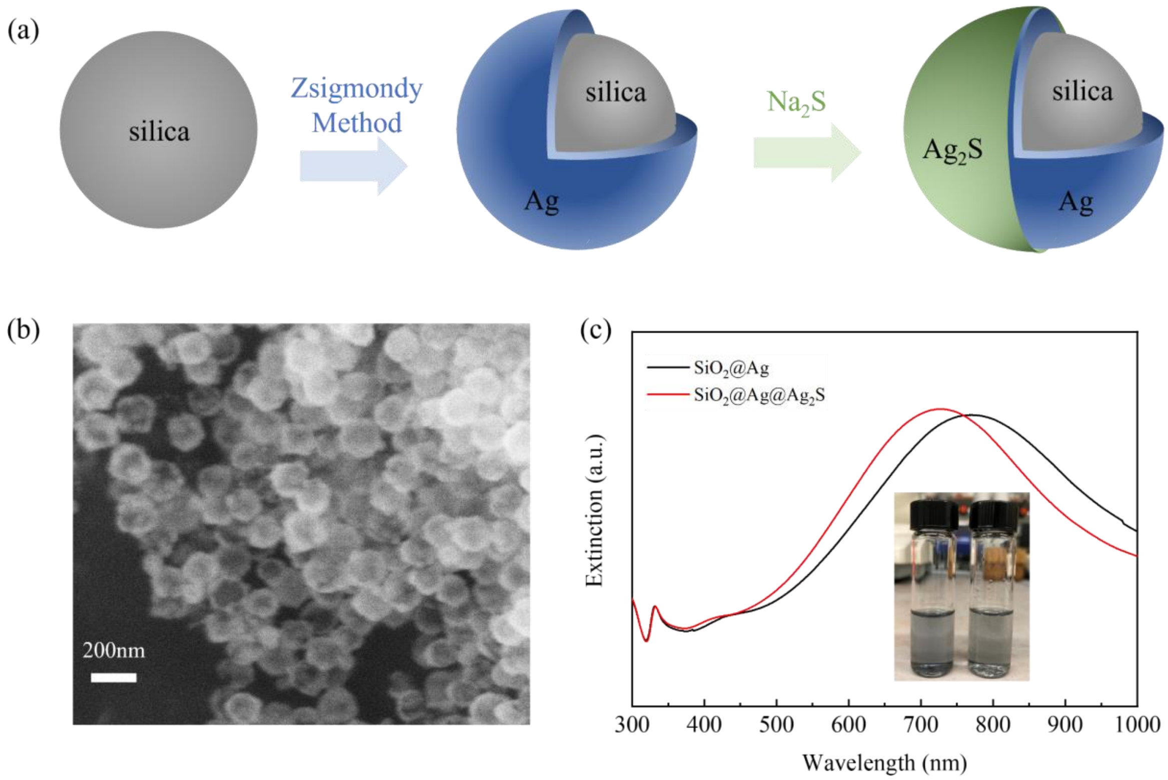

Figure 23 (a) Schematic of the synthesis of the core-shell SiO_2@Ag@Ag_2S (100@17@3 nm) plasmonic particles; (b) SEM images of the SAA particles; (c) Extinction spectra particles in DMF with the concentration of ~2× 10^{-10} M (inset: Optical photograph of plasmonic particle solutions, SAA on the left and SA on the right).

3.4 Plasmon PSC Device Optimization

These SAA nanoparticles were incorporated into different locations of PSCs (mesoscopic TiO_2/$MAPbI_3$/Spiro-OMeTAD). Figure 24a illustrates three configurations of the plasmonic devices; (position #1) inside the $MAPbI_3$ perovskite layer, (position #2) at the interface of perovskite/HTL (i.e., on the surface of perovskite layer), and (position #3) inside the HTL layer. Since the incident light comes from TiO_2 side of the device, the plasmonic particles are not expected to have dual scattering or up-conversion emission effects.[75, 85] Figure 24b shows the corresponding cross-sectional SEM image of control devices. The typical J-V curves of different plasmonic PSCs are shown in Figure 24c, and the corresponding photovoltaic parameters are tabulated in Table 2 and Figure 25 for direct comparison. The surface plasmons increased J_{SC} in comparison to the control devices. However, inserting the SAA particles at the perovskite/HTL interface or within HTL worsened V_{OC} and FF. To further investigate the effects of SAA particles, IPCE of the plasmonic PSCs was measured to find out the dependence on the incident photon energy, as shown in Figure 24d. SAA inside the perovskite layer and the HTL could obviously improve IPCE within the whole absorption spectrum. Moreover, the PSC with SAA embedded only inside the active layer showed a more obvious enhancement in the longer wavelength region (>500 nm). This is due to the near-field effect and the suppression of the non-radiative recombination, which is further explained in a following section. However, inserting the SAA particles at the perovskite/HTL interface or in the HTL did not lead to an effective enhancement of IPCE in the NBE region. This is likely caused by the energy level mismatch between Ag_2S of SAA particles and HTL, impeding the carrier transport from perovskite to HTL.[80, 86]

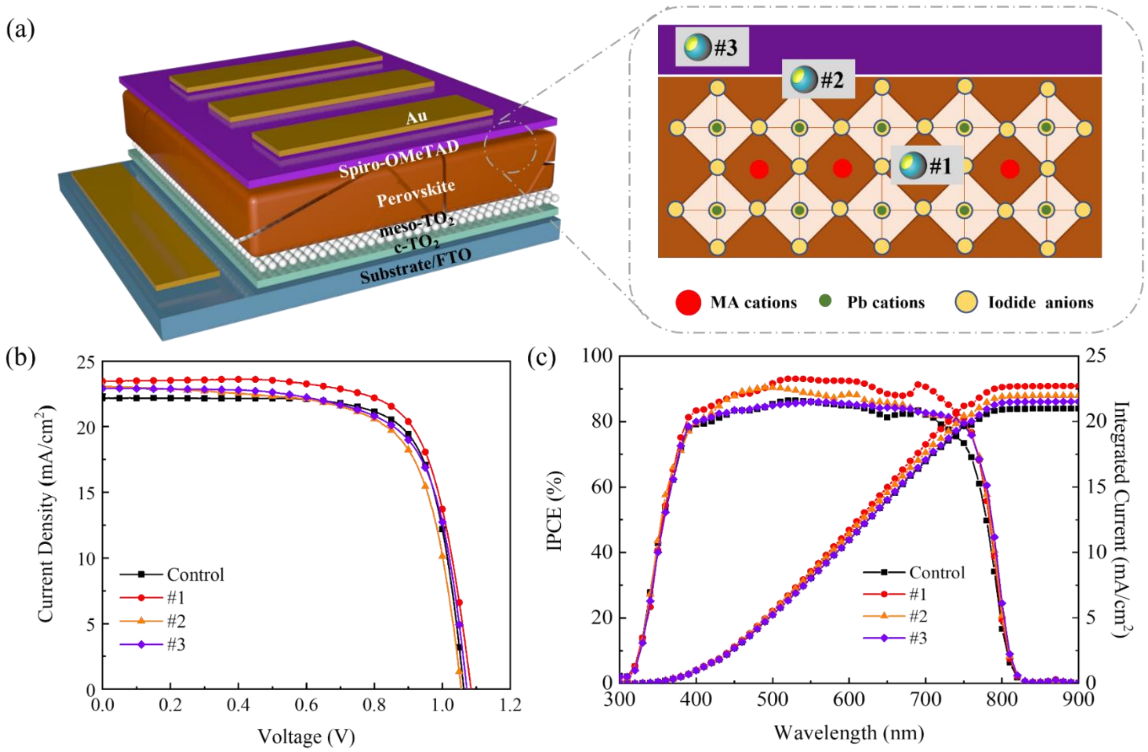

Figure 24 (a) Illustration of plasmonic SAA particles incorporated in different positions of PSCs and the positions are noted as #1 (inside the perovskite layer), #2 (at the interface of perovskite/HTL), #3 (inside the HTL); (b) *J-V* characteristics of PSCs with or without SAA under one sun illumination and (c) corresponding IPCE and integrated current of the PSCs.

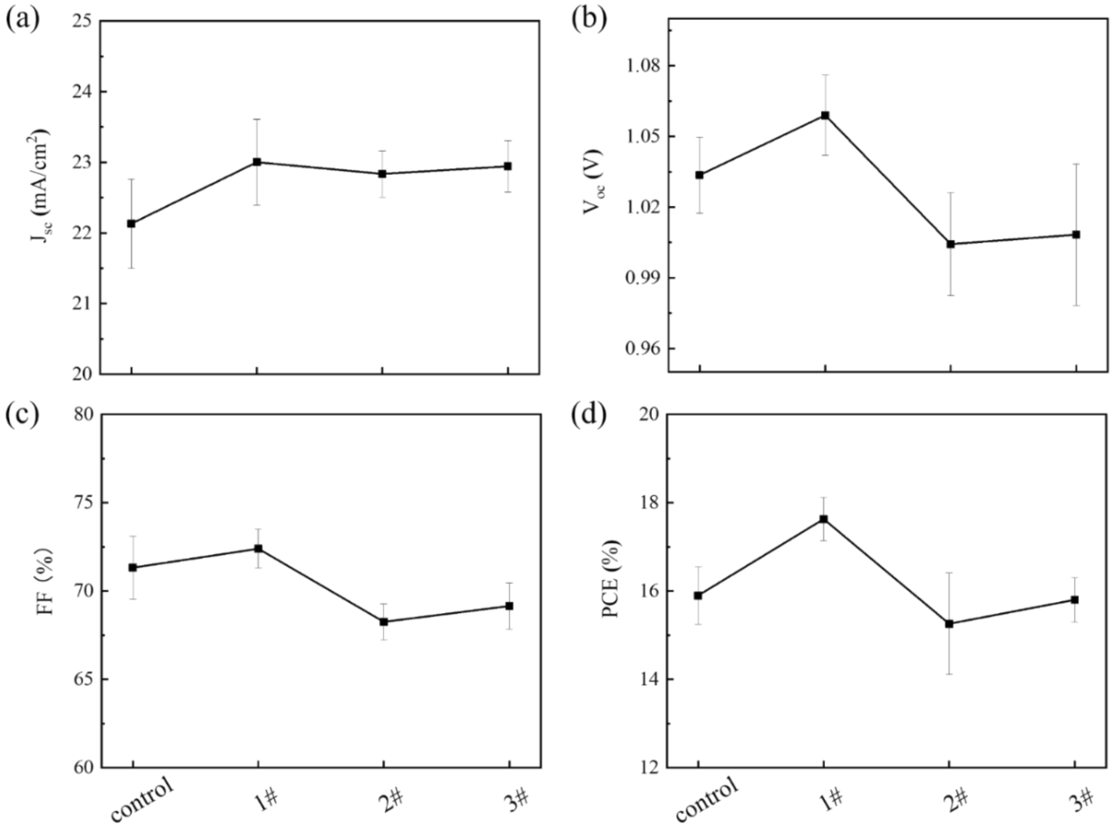

Figure 25 Statics of photovoltaic performance of the PSCs incorporated with SAA at different positions: (a) J_{SC}, (b) FF, (c) V_{OC}, and (d) PCE of the PSCs. (14 devices were measured for each of the conditions)

Table 2 Summary of the *J-V* parameters of the plasmon PSC devices incorporated in different positions (from 14 devices for each type)

	J_{SC} [mA/cm^2]	V_{OC} [V]	FF [%]	PCE [%]
control	22.17 (22.13±0.63)	1.063 (1.052±0.016)	74.3 (71.3±1.7)	17.49 (16.60±0.68)
#1	23.43 (23.00±0.61)	1.065 (1.059±0.017)	72.7 (72.4±1.1)	18.37 (17.63±0.49)
#2	23.11 (22.83±0.33)	1.055 (1.022±0.022)	68.8 (68.3±1.0)	16.77 (15.93±0.50)
#3	22.91 (22.94±0.37)	1.072 (1.026±0.030)	69.7 (69.2±1.3)	17.12 (16.28±0.47)

Based on results in Figure 24, the device structure of #1 was chosen to further investigate the effect of the plasmonic particles on the light absorption and carrier dynamics. Different concentrations of SAA particles were added into the perovskite layer. Figure 26a shows the champion J-V curves of PSCs (#1 structure) with 0, 1, 3, 5 wt.% SAA. In the control device, the PCE, JSC, VOC, and FF were 17.49%, 22.17 mA/cm^2, 1.063 V, and 74.3%, respectively. When 1 wt.% SAA particles were added, the PCE of the plasmonic PSC reached 18.37% with J_{SC}, V_{OC} and FF of 23.43 mA/cm^2, 1.065 V and 72.6%, respectively. The detailed photovoltaics parameters and other statistics are shown in Table 3 and Figure 27. As the SAA concentration increased, we found that the PCE and JSC first increased (at 3 wt.%) but then decreased (at 5 wt.%). Thus, the addition of 3 wt.% SAA particles improved the device performance the most (PCE = 19.88% and JSC = 24.66 mA/cm^2). Figure 26b shows IPCE and the corresponding integrated photocurrent. They are consistent with JSC values in Figure 26a. Figure 26c shows a difference in IPCE between the plasmonic and control devices (ΔIPCE). Though the enhancement of IPCE was observed in the entire spectral range, it was very pronounced where the surface plasmons were excited. Specifically, ΔIPCE was 15~20% in the NIR region ($600 < \lambda < 800$ nm). The optical effect of the SAA plasmon on the light absorption of perovskite layer was also investigated. Figure 26d shows the absorbance spectra of the perovskite layer embedded with SAA particles. In comparison to the control sample, the SAA addition clearly increases the absorption of the perovskite layer in the NBE region. It can be seen that as the insertion plasmon concentration increased from 1 to 3 wt.%, the absorbance increased at the range of 500-800nm. However, when further increasing the plasmon to 5 wt.%, there is an increase at 600-750nm while a decrease at 750-800nm range. This can be ascribed to partial aggregation effect of the particles during the film coating and thus the plasmon resonance peak is kind of blue shift.[49] The increasing Ab curves witness the best NBE light harvesting of the perovskite under 3 wt.% condition, supporting the notion that the device PV performance is improved due to the enhanced light absorption by the LSPR of SAA particles (Figure 23c). Although more plasmon insertion (with 5 wt.%) caused highest absorption at 600~750nm range, the result showed least enhancing effect. This is because over plasmon insertion will cause PbI_2 formation and decrease the quality of the active perovskite layer which will be discussed more. Further, it can be seen that compared with light harvesting, there is a blueshift of the enhancing peak of increasing IPCE (Figure 26c). The inconspicuous enhancement is due to the strong light extinction capacity of $MAPbI_3$ in this zone where the incident light is of high photon energy.[62]

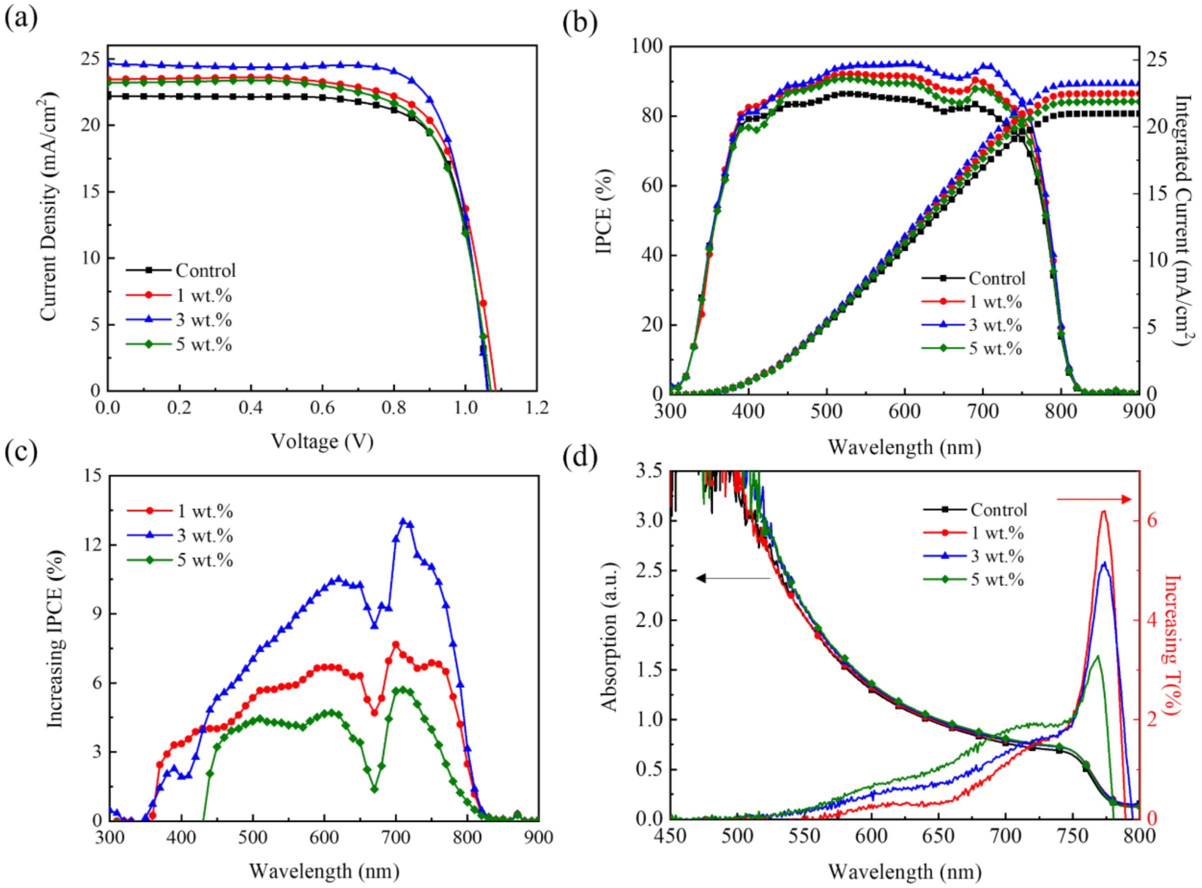

Figure 26 (a) *J-V* characteristics of PSCs with different concentrations of SAA NPs in the active layer of PSC under one sun illumination; (b) corresponding IPCE of the PSC devices with different amounts of incorporated plasmonic particles, (c) increasing IPCE and (d) UV-vis absorption spectra and the increasing absorption value of plasmonic PSC devices.

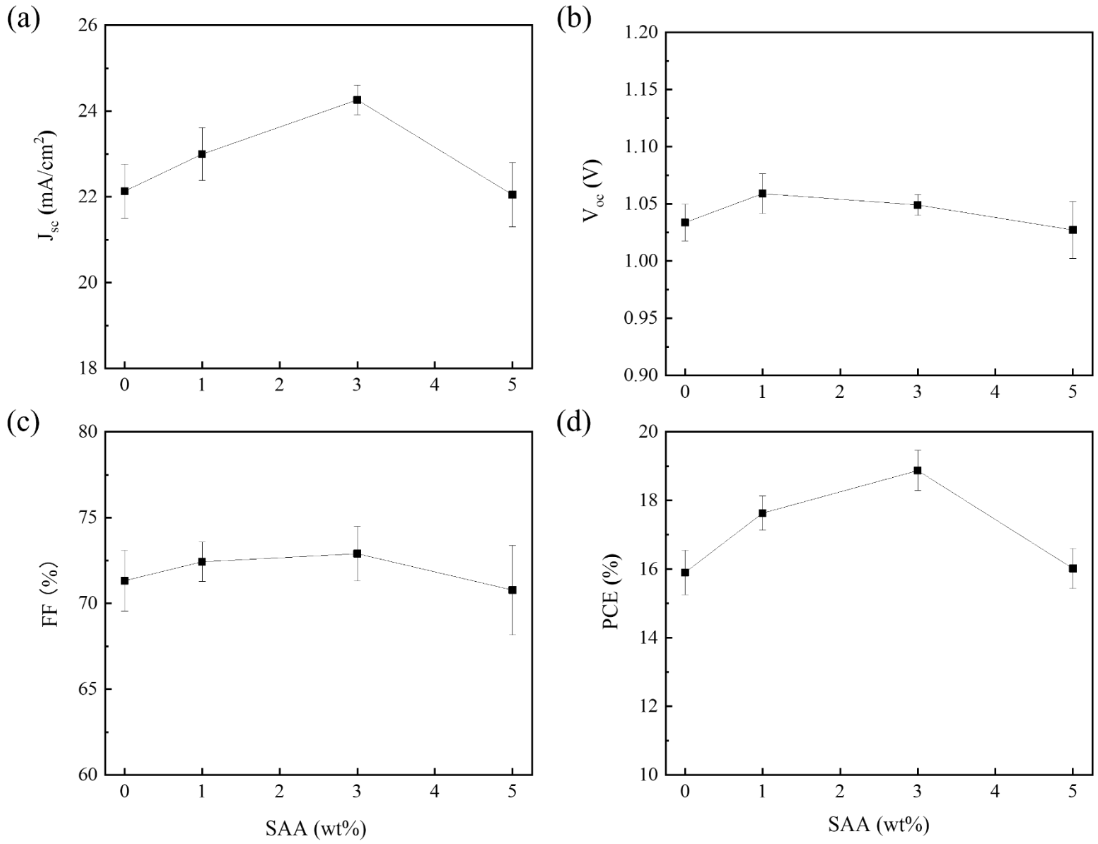

Figure 27 Statics of photovoltaic performance of the PSCs with various SAA concentrations (0, 1, 3, 5 wt.%): (a) J_{SC}, (b) V_{OC}, (c) FF, and (d) PCE of the PSCs.

Table 3 Summary of the *J-V* parameters of the plasmon PSC devices with different amounts of plasmonic particle incorporation (from 14 devices for each type).

	J_{SC} [mA/cm^2]	V_{OC} [V]	FF [%]	PCE [%]
control	22.17 (22.13±0.63)	1.063 (1.052±0.016)	74.3 (71.3±1.7)	17.49 (16.60±0.68)
1 wt.%	23.43 (23.00±0.61)	1.065 (1.059±0.017)	72.7 (72.4±1.1)	18.37 (17.63±0.49)
3 wt.%	24.66 (24.26±0.34)	1.061 (1.067±0.013)	76.0 (72.9±1.6)	19.88 (18.87±0.59)
5 wt.%	23.21 (22.13±0.81)	1.047 (1.027±0.025)	71.3 (70.8±2.6)	17.71 (16.08±0.71)

3.5 Origin of NBE Enhancement

Figure 28 shows the XRD patterns of $MAPbI_3$ films on FTO substrates with and without SAA nanoparticles. Diffraction peaks located at 14.1°, 28.4°, and 31.7° are assigned to (110), (220), and (310) planes of tetragonal $MAPbI_3$ crystal structure. There was no change in the crystal structure of the perovskite layer which was added with 1wt.% and 3wt.% SAA particles. When 5 wt.% SAA was added,[87] a new peak appeared at $2\theta = 12.8^o$, one of the main peaks of PbI_2. This observation indicates an excessive addition of SAA particles (e.g., 5 wt.%) prevents the crystallization of $MAPbI_3$ and deteriorates the carrier transport within PSCs.[80] This is consistent with previous studies reporting an optimal amount of the plasmonic particles inside the perovskite layer for improving the light absorption without deteriorating the carrier dynamics.[78, 88]

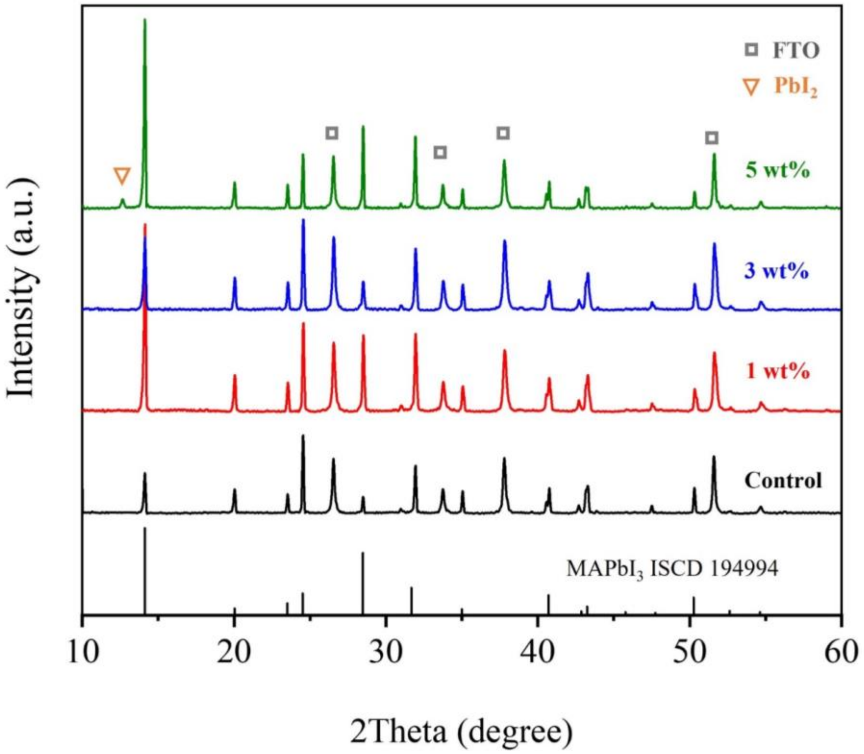

Figure 28 XRD spectra of perovskite layers with plasmon SAA incorporation.

In principle, the remarkable improvement in perovskite device light harvesting by plasmonic particle incorporation has been attributed to the enhancement of optical scattering and local field distribution.[56] The scattering effect can be refected and proven by the optical absorption strengthen [56, 89] as shown previously in Figure 26. Moreover, we has demonstrated the near electric field concentration at the vicinty of the plasmon structures in the semiconductive absorption material using FDTD calculation. The best plasmon enhanced device in our simulation work uses an optimal doping concentration of 3 wt.% for SiO_2@Ag@Ag_2S core-shell particles in the perovskite precursor solution. Note that the effective plasmon concentration is ultralow and the average distance between paticles should be several micrometers and the local field enhancing region is usually tens of nanometers. Thus, the local field distribution are performed with a simplified single particle method without any aggregations.[90]

Figure 29 illustrates the EM field distribution around the SAA particle embedded in the perovskite layer at different incident photon wavelengths. This simulation result supports the considerable enhancement of IPCE of the plasmonic device for NBE photons, as observed in our experiment. We are investigating the EM response under the wavelength range in the perovskite wavelength range (400~800nm) with a ~100nm interval. To further examine the enhanced NBE absorption via the excitation of the surface plasmons in the NIR region, further simulations were performed at five representative incident photon wavelengths (794, 702, 594, 496, and 398 nm). The resulting EM field distributions are shown in Figure 29a-e. They show that the local field in the vicinity of the silver shell becomes stronger at all the tested wavelengths, but the intensity and spatial extension of the EM field decrease with decreasing the wavelength. When the wavelength of incident photons is 794 nm, the near-field intensity in the vicinity of the Ag shell (up to 50 nm from the surface of the Ag shell) increases by around 15 times (Figure 30). At 398 nm, the near-field effect of the SAA particles becomes negligible. This indicates that the LSPR of our SAA particles could manage the light absorption more effectively and produce more excitons in the NIR region than in the blue region. The wavelength-dependent IPCE variation is not as significant as wavelength-dependent plasmon light harvesting. The increasing IPCE is more complicated and usually a smaller IPCE in the control device leading to a higher increasing value. More important, IPCE is not only related to the light harvesting efficiency but also the carrier kinetics including carrier trapping and recombination.

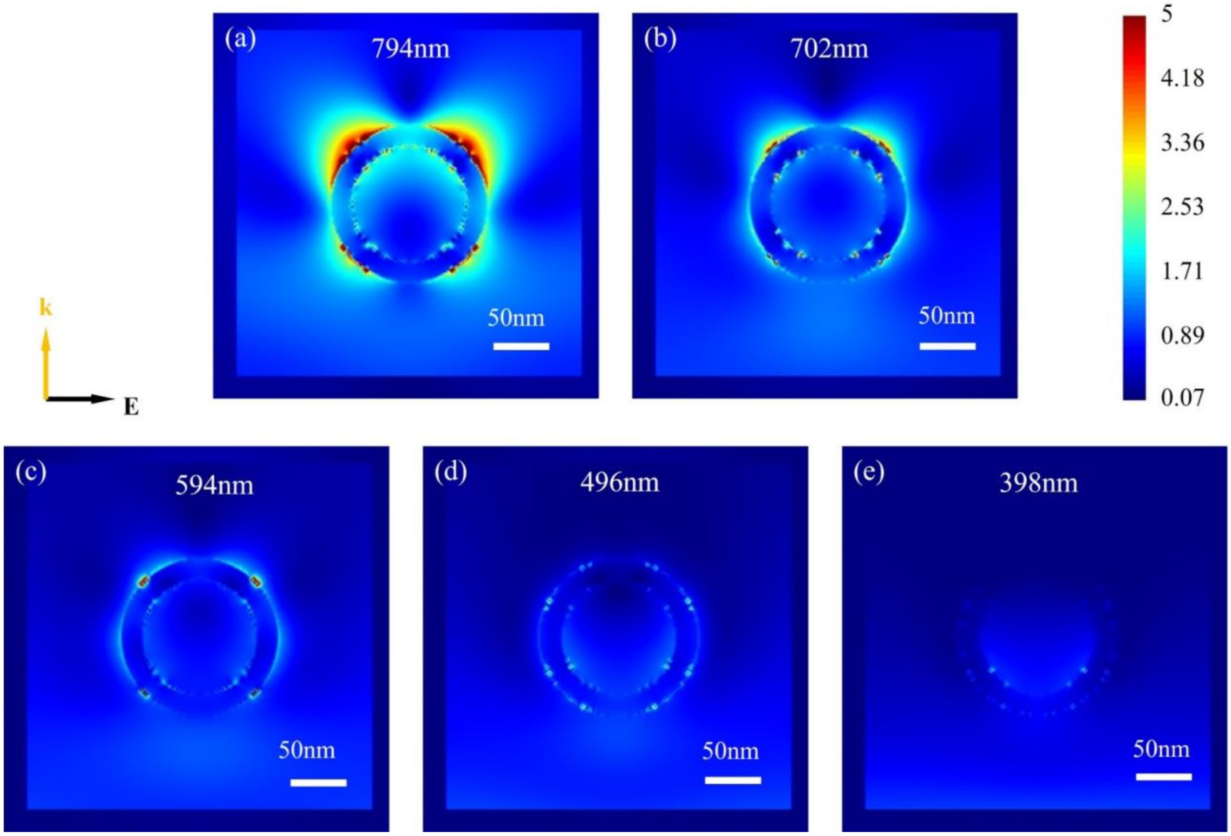

Figure 29 Simulated electric field distribution of $MAPbI_3$ layer incorporated of SAA plasmon corresponding different resonance wavelengths at 794(a), 702(b), 594(c), 496(d) and 398 nm(e) respectively.

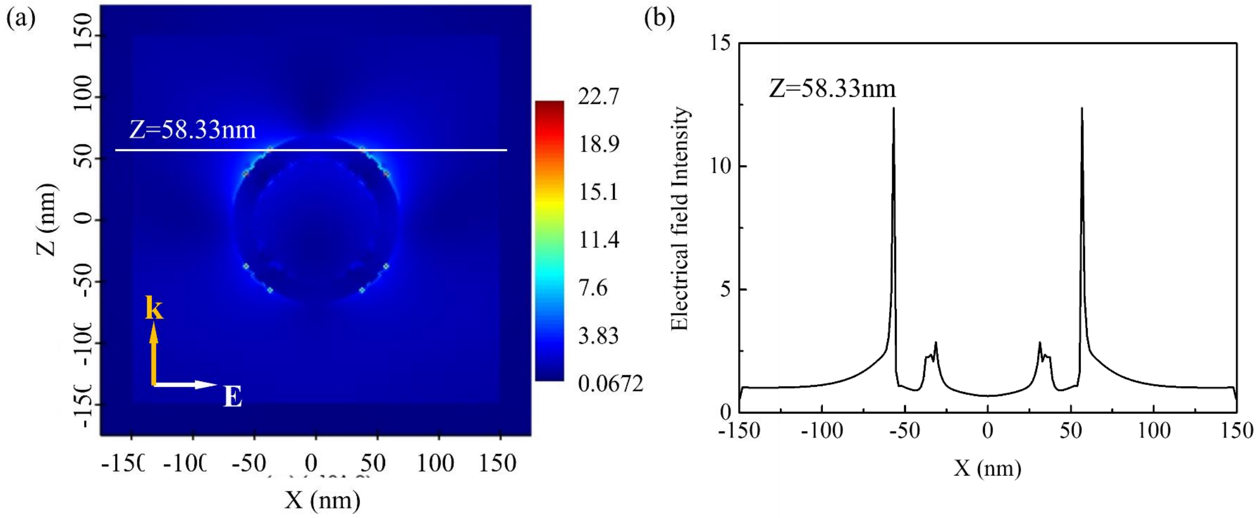

Figure 30 (a) Simulated electric field distribution of MAPbI₃ layer incorporated of SAA plasmon and (b) The X-axis electric field intensity (Z=58.33 nm) at 794 nm wavelength.

According to the previous studies on the plasmonic effects of the PSCs, the LSPR or surface plasmons could also influence the IPCE of the solar cell by changing the carrier dynamics.[53, 77] To examine this for our case, the steady-state PL and time-resolved PL (TRPL) spectra of the perovskite layer with and without 3 wt.% SAA particles were measured. Figure 31 shows the results of two different perovskite layers on quartz glass substrates. Two representative excitation wavelengths at 450 nm (2.76 eV) and 700 nm (1.77 eV) were selected to compare the effect of SAA nanoparticles in the visible and NIR regions. We find that the incorporation of the SAA particles does not change the PL spectral shape, the maximum PL peak position. Interestingly, the broad PL bands which exhibited an excitation-wavelength-dependent shift, could be deconvoluted into two sub-band Gaussian peaks at 770 nm (1.61 eV) and 798 nm (1.55 eV).[91, 92] The emission peak at 770 nm originates from the optical bandgap of tetragonal $MAPbI_3$ is ~1.6 eV.[93] Meanwhile, the observed broadening of the PL band (~56 meV) is likely attributed to the Urbach energy of localized states associated with shallow defects sites. The mechanism underlying the excitation-wavelength-dependence of the PL in this study seems more complicated. Scattering, reabsorption, and re-emission caused the dual-emission or shift of PL peaks, which is referred to as photon-recycling processes.[92, 94] Herein, both Figure 31a and c show fluorescence enhancement in the presence of plasmonic particles. The PL intensity enhancement via plasmon was almost two times larger for 700 nm excitation than 450 nm excitation. The larger effect of the 700 nm excitation is due to the match of the excitation wavelength (700 nm) with the LSPR wavelength of our SAA particles.[95] [77, 88] To further examine the role of SAA nanoparticles, the PL decay profiles of the plasmon and control films were measured using 450 nm excitation and 700 nm excitation, as shown in Figure 31c and d. The corresponding effective PL lifetimes were obtained by fitting the decay data to a double-exponential function. The 450 nm excitation slightly decreased the lifetimes of SAA-added film (from τ_1 =1.28 ns and τ_2 = 7.23 ns to τ_1 = 0.88 ns and τ_2 = 5.10 ns). This indicates that the slight increase in the PL intensity under the 450 nm excitation is due to only the slightly increased light absorption by SAA nanoparticle, as has been shown in our results (Figure 26). Interestingly, the addition of SAA particles rendered both time constants of the plasmonic film significantly longer than those of the control sample (from τ_{avg} = 5.133 ns to τ_{avg} = 8.757 ns) (Table 4). These longer lifetimes suggest that the 700 nm excitation of the plasmonic film not only promotes the light absorption but also increases the carrier lifetime.[96] The overall comparison of our PL, TRPL, and IPCE spectra results have shown that the incorporation of NIR SAA nanoparticles facilitates the photon-to-charge carrier conversion process by suppressing the carrier non-radiative recombination as well as enhancing the light absorption, similar to prior reports.[77, 97]

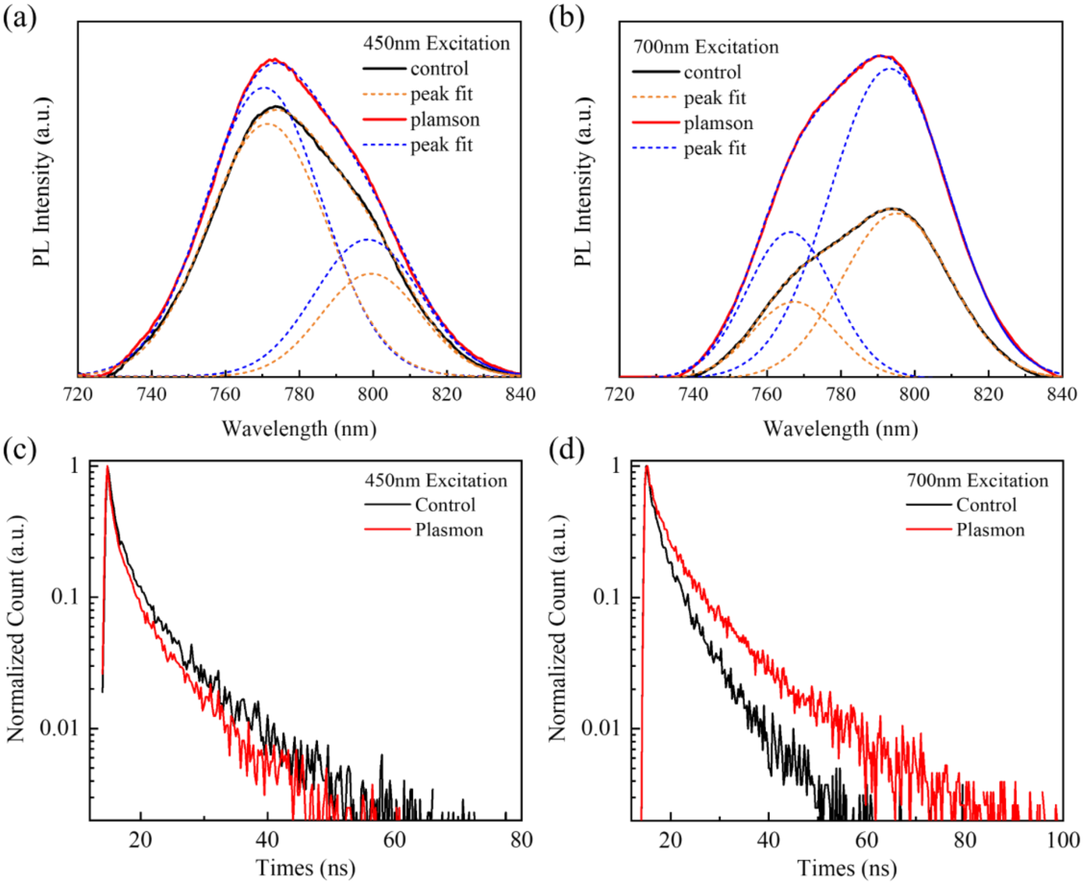

Figure 31 PL spectra (a and b) and TRPL lifetime (c and d) of perovskite layers with and without plasmonic particles excited by 450nm and 700nm, respectively.

Table 4 Parameters of the TRPL spectra of perovskite films with and without plasmon particles under two excitation wavelengths.

Excitation Wavelength [nm]		τ_{avg} [ns]	τ_1 [ns]	I_1 [%]	τ_2 [ns]	I_2 [%]
450	Control	5.441	1.284	30.11	7.232	69.89
	Plasmon	3.911	0.877	28.16	5.101	71.84
700	Control	5.133	1.756	32.67	6.771	67.33
	Plasmon	8.757	2.859	34.06	11.803	65.94

Finally, we also found that the device J-V hysteresis and stability could be improved by incorporating SAA particles. We quantified the J-V hysteresis of the fabricated PSC devices with and without SAA particles by using the hysteresis index (HI) which is defined as[98]:

$$HI = \frac{J_{RS}(0.8V_{OC}) - J_{FS}(0.8V_{OC})}{J_{RS}(0.8V_{OC})} \tag{3-1}$$

where $J_{RS}(0.8V_{OC})$ and $J_{FS}(0.8V_{OC})$ are the photocurrent densities at 80% of the V_{OC} for reverse and forward J-V scans, respectively. As shown in Figure 32a, the PSC devices with and without the SAA nanoparticles in the perovskite layer showed HI of 0.21 and 0.35, respectively, thus a ~40% reduction in hysteresis by SAA nanoparticles. Electron trapping has been suggested as one of main reasons for the hysteresis and less trapping of charge carriers in the plasmonic devices may reduce the hysteresis. Furthermore, the plasmonic PSCs showed an improved performance stability, retaining 90% of the initial PCE after 500 hours storage in a dark and inert environment, as opposed to 82% retention of PCE for the control device without PAA particles (Figure 32b). This is consistent with previous studies that reported the retarded aging of the time-dependent device performance or even a certain level of the improvement by the incorporation of plasmonic particles within PSCs. By avoiding the carrier accumulation at the interface and grain boundary, the retention rate of the initial photovoltaic performance is increased in the plasmonic PSCs.

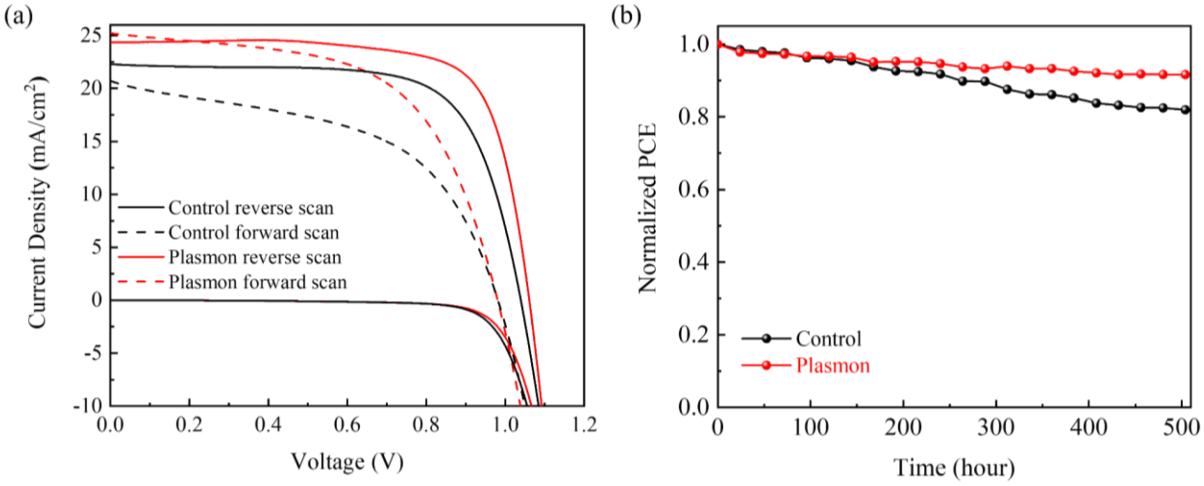

Figure 32 (a) The hysteresis behavior and (b) stability of the device with and without plasmon particles.

3.6 Conclusion

In summary, SAA plasmonic particles with intense LSPR at the NIR range were successfully synthesized and incorporated into $MAPbI_3$ PSCs. We demonstrated the 10% enhancement of J_{SC} and PCE by optimizing the location and concentrations of SAA particles in the PSC devices, particularly by adding SAA particles within the perovskite layer. This improvement in the power conversion of PSCs was accompanied by the reduced J-V hysteresis and aging of the device. We found that the surface plasmons of SAA particles enabled the near-field absorption of the NBE photons in the perovskite layer, resulting in the effective utilization of the low-energy photons. Moreover, the SAA particles significantly increased the carrier lifetime in the perovskite film under NBE excitation due to the suppressed nonradiative recombination of carriers via the LSPR effect. The results demonstrate that the plasmonic SAA particles designed for the LSPR at the NIR range concurrently improve the light absorption and subsequent carrier dynamics of the PSCs at the NBE region. The intrinsic working mechanism of the NIR plasmon in PSCs revealed in this study should also be helpful for guiding the application of tunable plasmons to other photovoltaic devices and optical sensors.

4.0 Surface Engineering of SnO_2 Electron Transport Layer via PbS Quantum Dots

4.1 Background and Motivation

Due to the outstanding properties and solution processability, organometal halide perovskite solar cells (PSCs) rapidly emerge as a high-efficiency and low-cost photovoltaic technology. PSCs have shown a rapid increase in power conversion efficiency (PCE) from 3.8% to over 25% within a short period.[18, 30] The architecture of regular PSCs includes a mesoporous TiO_2 electron transport layer (ETL).[17, 99] Though TiO_2 ETL enables the high PCE, it requires high-temperature annealing to fully convert the precursor to a crystalline film.[33] And TiO_2 ETLs cause electron trapping at the interface,[100] hysteresis of current density-voltage (J-V) curves,[101] and rapid aging of perovskite (PVK) layer due to their photocatalytic properties. Therefore, there has been intensive research to develop alternative ETLs utilizing a simple and low-temperature process. Among them, SnO_2 is a candidate of enormous potential for its high transmittance, suitable electronic band structure, high electron mobility (approximately 10^{-3} $cm^2/(V \bullet s)$, and low-temperature fabrication process. Recently, planar n-i-p PSCs using SnO_2 thin film as ETL have achieved certificated PCE of 25.5% and high operational stability.[18, 102]

Efficient electron extraction is more difficult in PSCs of the thin ETLs than in PSCs of the mesoporous structures, due to a small contact area between the ETL and PVK. In addition, there are structural defects like oxygen vacancies ($V_O^{\cdot\cdot}$) in the thin SnO_2 film made out of a colloid solution.[103] These defects deteriorate the performance of ETL, because $V_O^{\cdot\cdot}$ defects will leave Sn dangling bonds on the surface of SnO_2.[104] And such surface defects can be the electron trap sites as well as easily absorb the water and hydroxyl groups in the air. Thereafter, various modification strategies have been reported to passivate the defects of SnO_2 film. They include halide salt ionization,[105] organic and inorganic functional group decormation[106] and interfacial layer shaping.[102] It is worth noting that the interface engineering is a straightforward method which can effectively reduce electron accumulation and nonradiative recombination loss in the device.[104, 107] Recently, quantum dot (QD) materials have been applied to SnO_2 films to optimize the ETL electrical properties and thus improve the PCE and stability of corresponding planar PSCs. For instance, Chen *et al.* fabricated a novel SnO_2 ETL using red carbon QDs (RCQs).[34] The SnO_2-RCQ ETL achieved excellent electron mobility by passivating the trapping sites and defects at the ETL/PVK interface (Figure 33). Meanwhile, QD materials such as CdS of tunable optoelectronic performance have been proven to modulate the work function of SnO_2 and increase the open-circuit voltage (V_{OC}) of PSCs.[108]

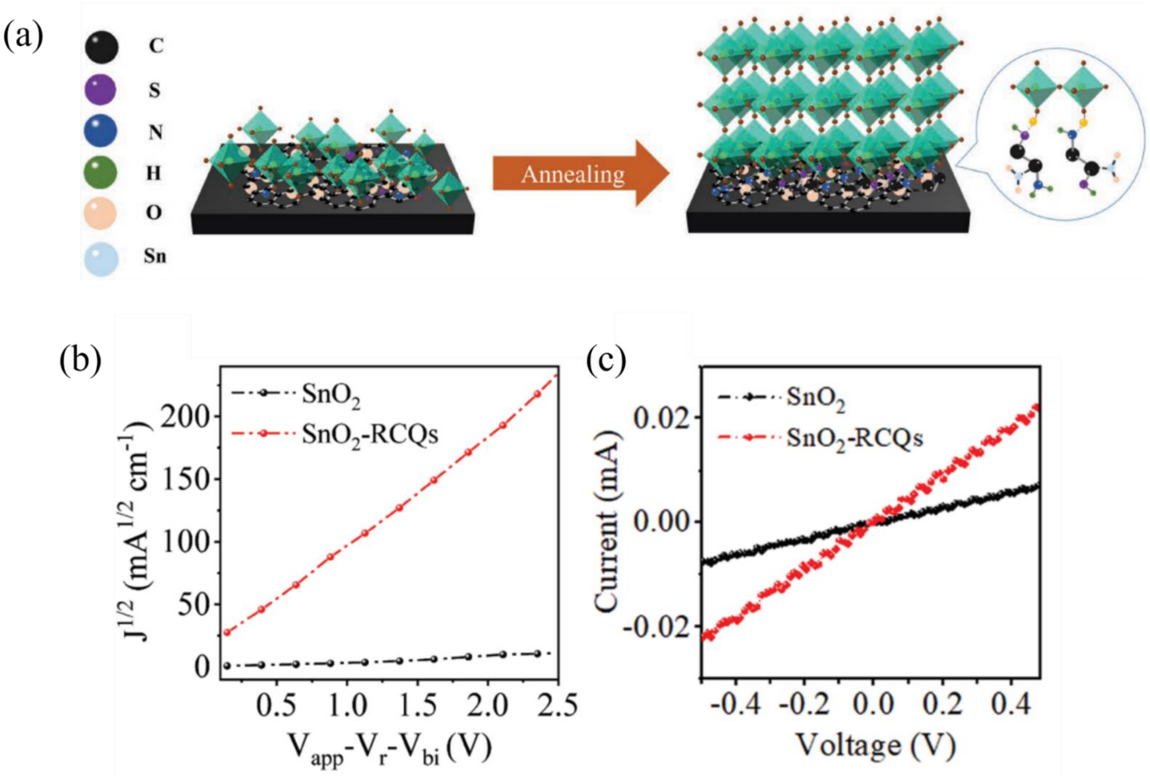

Figure 33 (a) Crystalline mechanism of a perovskite grown on SnO_2 ETLs modified by RCQs. (b) *J-V* characteristics of the electron-only devices and (c) conduction properties of the SnO_2 films with and without RCQs. (Reproduced with permission from 34. Copyright 2019 WILEY-VCH Verlag GmbH & Co. KGaA, Weinheim.)

Moreover, the surface treatment of ETL also has an effect on the crystallization and grain-growth in the PVK layer. If the material using for ETL surface passivation enhances the crystallinity of PVK at once, it can further improve the quality of the PVK layer as well as decrease the defects at ETL/PVK interface. Choy et al. have proved there is a strong inetraction between the halide anions and PbS QDs (Figure 34). This solid ionic interaction can inhibit iodide ions mobilization in the PVK film and thus increase the crystallization quality and stability of the final PSC devices.[109] However, PbS QDs have not been applied to the surface of SnO_2 ETL to obtain high-performance n-i-p PSCs.

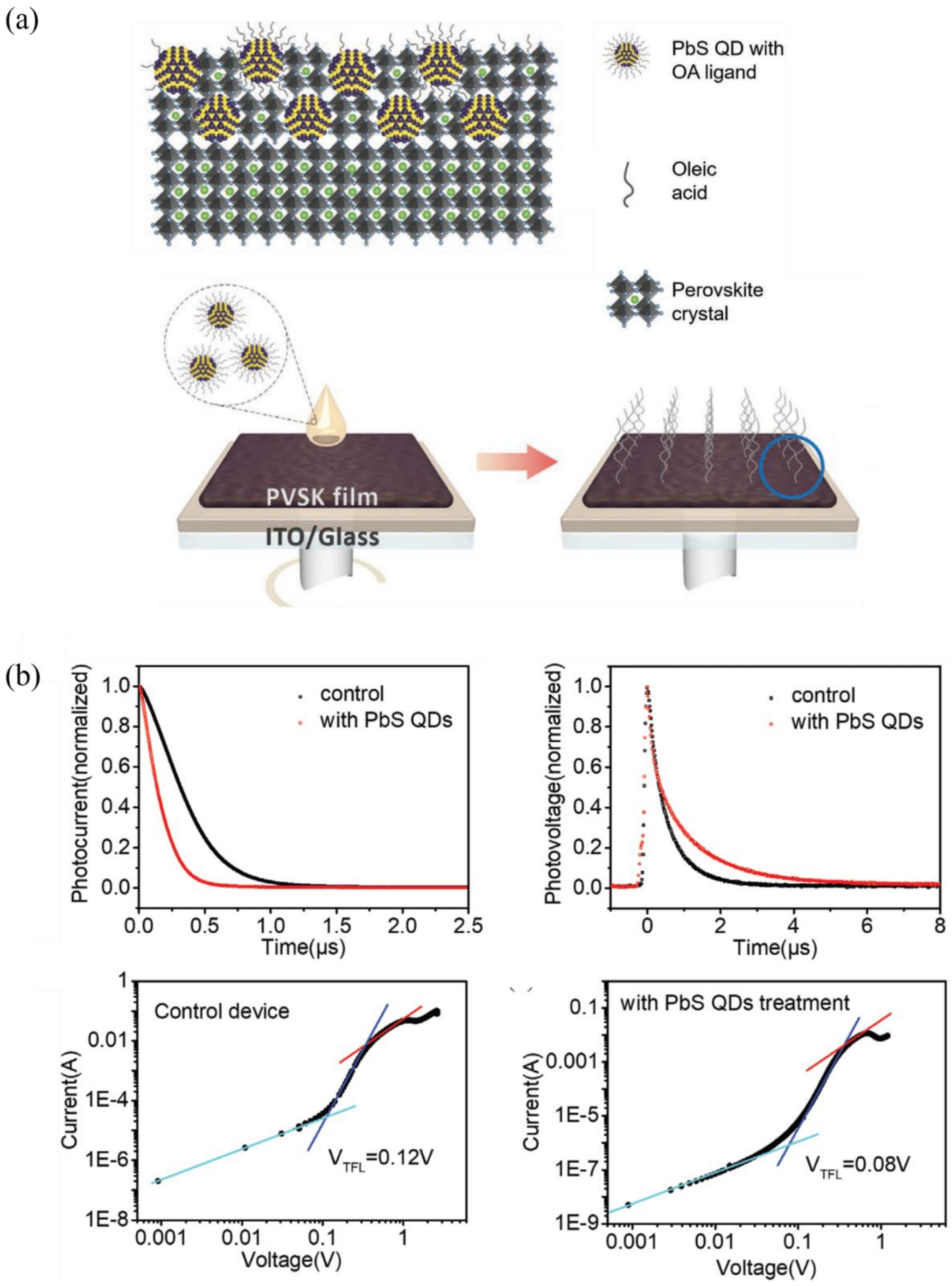

Figure 34 (a) schematic diagram of PbS QDs incorporated perovskite film and the interaction between perovskite and PbS QDs and (a) carrier dynamic analysis of the devices. (Reproduced with permission from 109. Copyright 2020 Wiley-VCH GmbH.)

In this study, we engineered the SnO_2/PVK interface by introducing a thin PbS QD interlayer and explored the dual roles of PbS QDs in the passivation of SnO_2 ETL and the crystallization of the active PVK layer. A solution of PbS QDs was drop-casted on the SnO_2 film to passivate dangling Sn bonds on the surface of SnO_2. The modified ETL (SnO_2-PbS) has fewer trap sites and its conduction band edge matches better with that of the PVK layer. In addition, the PbS QDs underlayer assists the nucleation of PVK by stabilizing the intermediate phase between δ and α-$FAPbI_3$ phases. The PVK layer grown on the SnO_2-PbS ETL has a better morphology and crystallization. All of them improve the extraction/transportation of photogenerated electrons in PSCs with the configuration of FTO/SnO_2-PbS/$(FAPbI_3)_{0.95}(MAPbBr_3)_{0.05}$(OAI)/spiro-OMeTAD/Au. The short-cut current density (J_{SC}) and V_{OC} increase to 24.02 mA/cm^2 and 1.14 V, leading to the best PCE of 21.66%. Moreover, the PbS QD coating increases the stability of PSCs. After 1000 hour-long operation in ambient air, the PCE of the PbS QD treated PSCs decreased only by 7%, while that of the control sample decreased by 12%. This work offers a new interface engineering method to achieve the full potential of SnO_2 ETLs of PSC devices.

4.2 Experimental

FTO glass (TEC15, purchased from MSE Supplies LLC) was cleaned sequentially with acetone, deionized (DI) water and ethanol for 15 minutes in ultrasonic system. The aqueous solution of SnO_2 (diluted in DI water at a mass ratio of 2.67 wt.%) was deposited on FTO substrates at 3000 rpm for 30 seconds and after that the substrates were annealed at 150 ^{o}C for 30 minutes to form the electron transport layer (ETL). In the case of PbS QD modification, as prepared PbS QD solution was spin coated on the surface of ETL at 4000 rpm for 20 seconds just before the perovskite layer deposition. 70 μL of a mixed organic metal halide solution (889 mg $FAPbI_3$, 16.5 mg $MAPbBr_3$ and 16.5 mg MACl in 1 ml mixed solvent: DMF/DMSO=8:1, v/v) was spin-coated on SnO_2 layer at 4000 rpm for 20 seconds. Anisole was used as an antisolvent in the last 10 seconds. As-deposited films were later transferred onto a hot plate and then annealed at 140 °C for 10 minutes. Subsequently, OAI (4 mg/ml in IPA) was spin coated on the surface of perovskite films for passivation at 4000 rpm for 20 seconds and the films were then annealed at 100 ^{o}C for 10 minutes. 1 ml Spiro-OMeTAD (72.3 mg/ml in CB) solution was mixed with 28.8 μL 4-tBP and 19.6 μL Li-TFSI (360 mg ml-1 in AN) for hole transport layer deposition. The Spiro-OMeTAD was deposited at 3000 rpm for 30 seconds. All the layer deposition and annealing processes were conducted in ambient air with relative humidity (RH) of 25%. Finally, the 70 nm Au was deposited by the Plassys Electron Beam Evaporator.

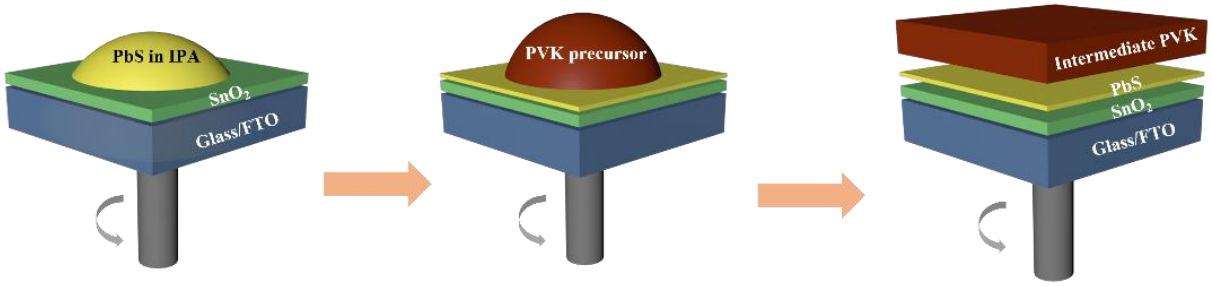

Figure 35 Schematic illustration of deposition of PbS interlayer between SnO_2 and perovskite.

4.3 SnO_2 ETL surface modification

As shown in Figure 35, SnO_2 colloid and PbS QD solutions were sequentially spin-coated before the $(FAPbI_3)_{0.95}(MAPbBr_3)_{0.05}$ active layer was deposited. As-synthesized PbS QDs of a long alkyl ligand oleic acid (OA) surfactant (Figure 36a) are dispersed in toluene solvent. As seen in Figure 36b, the PbS coating does not change the transmittance or the bandgap (E_g) of SnO_2 based ETLs and the corresponding PVK layers. In addition, the decoration of PbS QD did not change the electron conductivity of ETL (Figure 36c) which is an essential property of ETL.

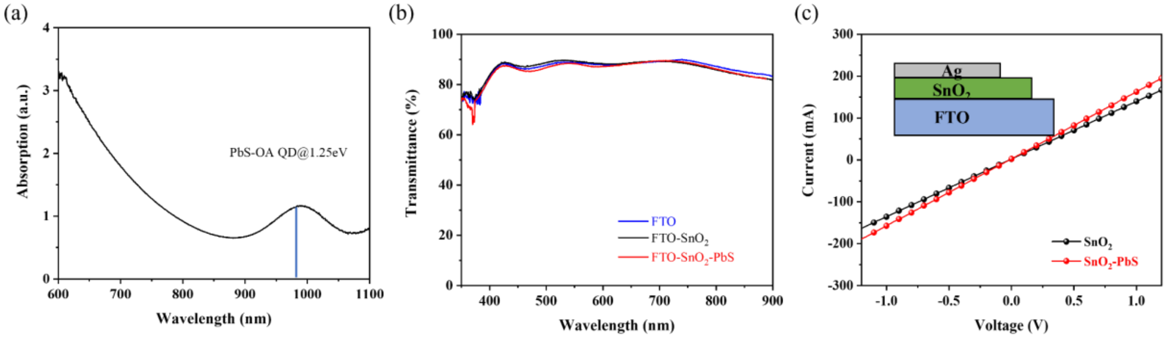

Figure 36 UV-vis spectra of (a) QD PbS with OA ligand in Hexene absorbance, (b) transmittance spectra of FTO (black), SnO_2 (blue) and SnO_2-PbS (red) deposited on FTO and (c) conductivity measurements of SnO_2 (black) and SnO_2-PbS (red).

Ultraviolet photoelectron spectroscopy (UPS) was used to examine the band structure of SnO_2 with and without PbS coating. Figure 37a shows the measured band structures of SnO_2 and SnO_2-PbS films. It ca be seen that PbS coating slightly decreases the work function (W_f) of the ETL. The conduction band edge of SnO_2, SnO_2-PbS, and PVK films were -4.42 eV, -4.24 eV, and -4.15 eV, respectively. Since there is a better energy level match between the PVK/SnO_2-PbS than PVK/SnO_2, improved interfacial energetics are obtained and more efficient electron extraction is expected at the interface.[18, 110] UPS spectra and the detailed analysis results are shown in Figure 37b-e and Table 5.

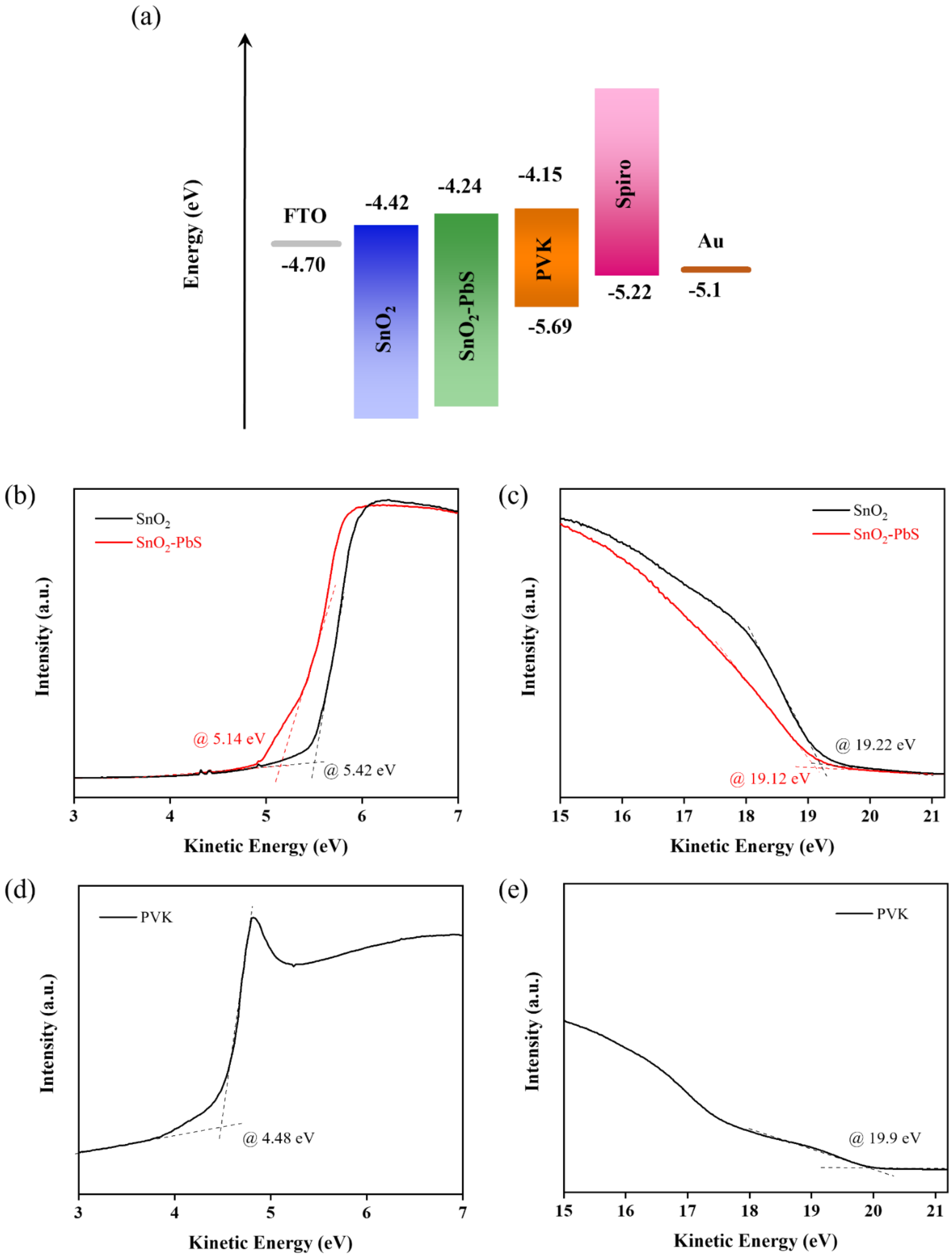

Figure 37 (a) Illustration of band energy structure of the individual layers in a PSC device and kinetic energy spectra of (b&c) SnO_2 (black) and SnO_2-PbS (red) and (d&e) PVK deposited on ITO substrate.

Table 5 UPS analysis data (Unit: [eV])

ETLs	E_g	W_f	KE at high energy	VBM
SnO_2	3.00	5.42	19.22	2.02
SnO_2-PbS	3.00	5.14	19.12	2.12
PVK	1.54	4.48	19.9	1.21

Furthermore, we measured the chemical states of SnO_2 and SnO_2-PbS ETLs using X-ray photoelectron spectra (XPS). Figure 38a and b show their Sn 3d peaks and O 1s peaks. The $3d_{5/2}$ peak of Sn^{4+} is 487.2 and 487.3 eV with and without PbS coating. The spin-orbit splitting energy between Sn $3d_{5/2}$ and $3d_{3/2}$ is 8.4 eV.[35, 111] The shift of the core-level spectrum of Sn by PbS QD coating indicates that the dangling Sn is passivated by the sulfide ions of PbS.[112] Two dominant peaks in the O 1s spectrum are assigned to O-Sn^{4+} and chemisorbed nonlattice oxygen (O^{chem}) such as O^{-}, O^{2-}, and OH^{-} peaks. The area ratio of O^{chem} in O 1s peaks is 22.9 and 17.3% for SnO_2-PbS and SnO_2. The higher O^{chem} content is compelling evidence testifying that the OA ligand of PbS QDs is attached to the SnO_2.[113, 114] Figure 38c and d further shows the Pb 4f and S 2p peaks of the surface PbS QD coating. [109, 115]

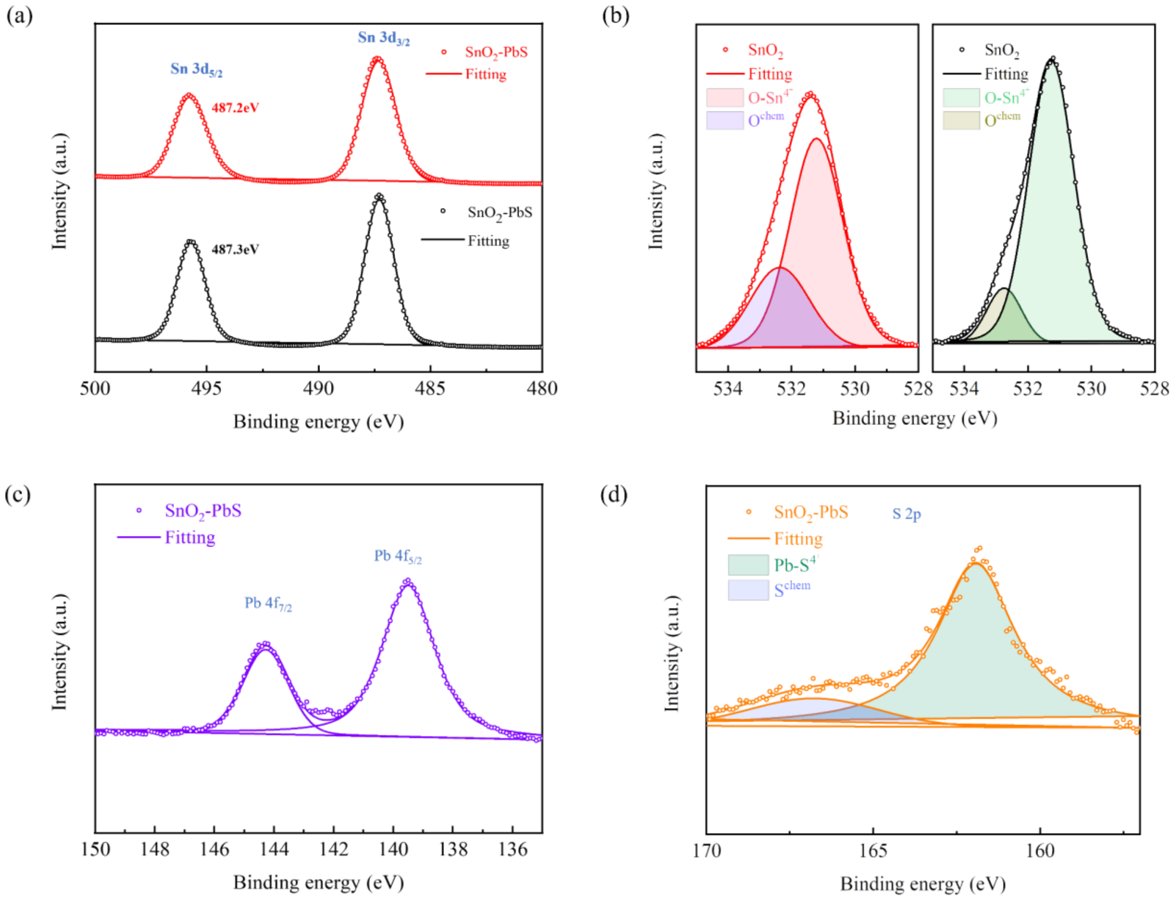

Figure 38 PVK layers and deconvoluted XPS peaks of (a) Sn 3d and (b) O 1s states in as-prepared SnO_2-PbS and SnO_2 films and (c) Pb 4f and (d) S 2p in SnO_2-PbS film.

X-ray diffraction (XRD) and scanning electron microscopy (SEM) are used to examine the crystal structure and microstructure of PVK films that are coated on SnO_2-PbS and bare SnO_2. The XRD spectra are shown in Figure 39. Regardless of the PbS QD concentration in a coating solution, PVK films exhibit the similar crystallinity of photo active α $FAPbI_3$ phase with a high purity.[28, 30] The three main peaks posited 13.92°, 28.04° and 42.63° are corresponding to (100), (200) and (300) peaks of the cubic perovskite phase. Notably, there is a small peak at 12.7° that is assigned as (001) peak of the PbI_2 phase in the PVK deposited on bare SnO_2 (Figure 39b).[29] When PbS QDs coated underlay, there is a decrease of the PbI_2 phase. This suggests that PbS QDs on SnO_2 layer can suppress the formation of the second phase in the final active layers. Furthermore, in the top-view morphology of SEM images in Figure 40, the average grain size of all smooth PVK crystal is around 1.5 µm. Though the average grain size does not change as coating the QDs, the increase concentration of the PbS coating solution decreases the distribution of small grains and a number of pinholes.

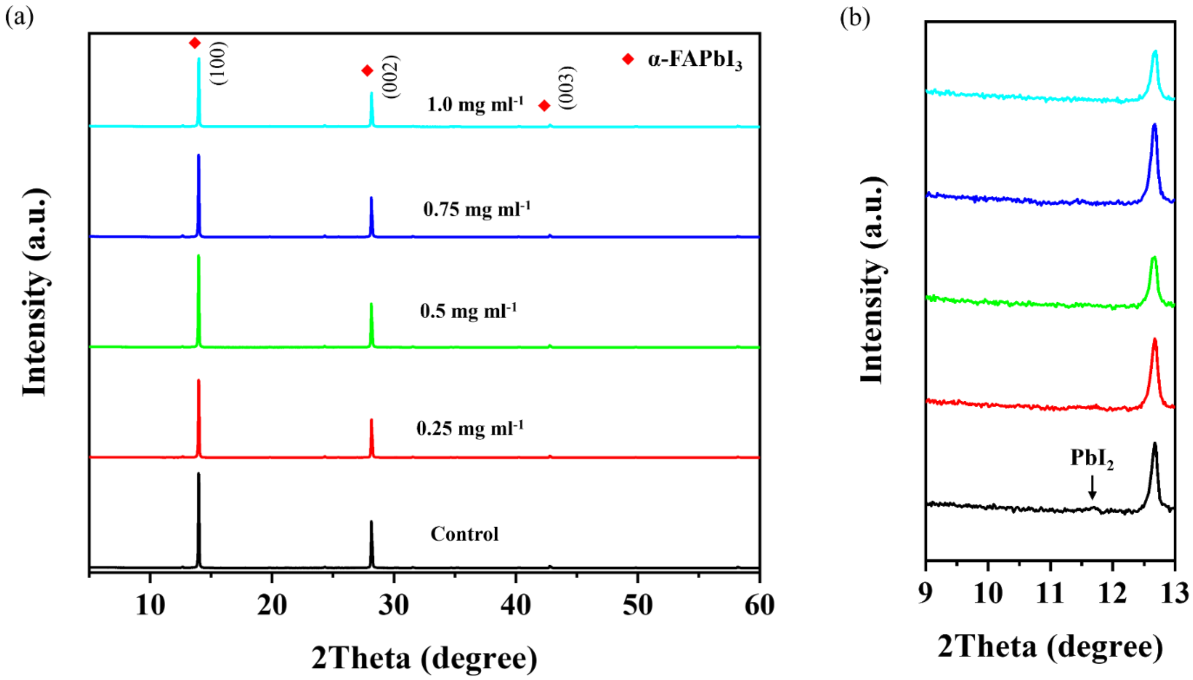

Figure 39 XRD patterns of PVK films on SnO_2 with PbS coating of different concetartions after annealing at 140 °C for 10 min.

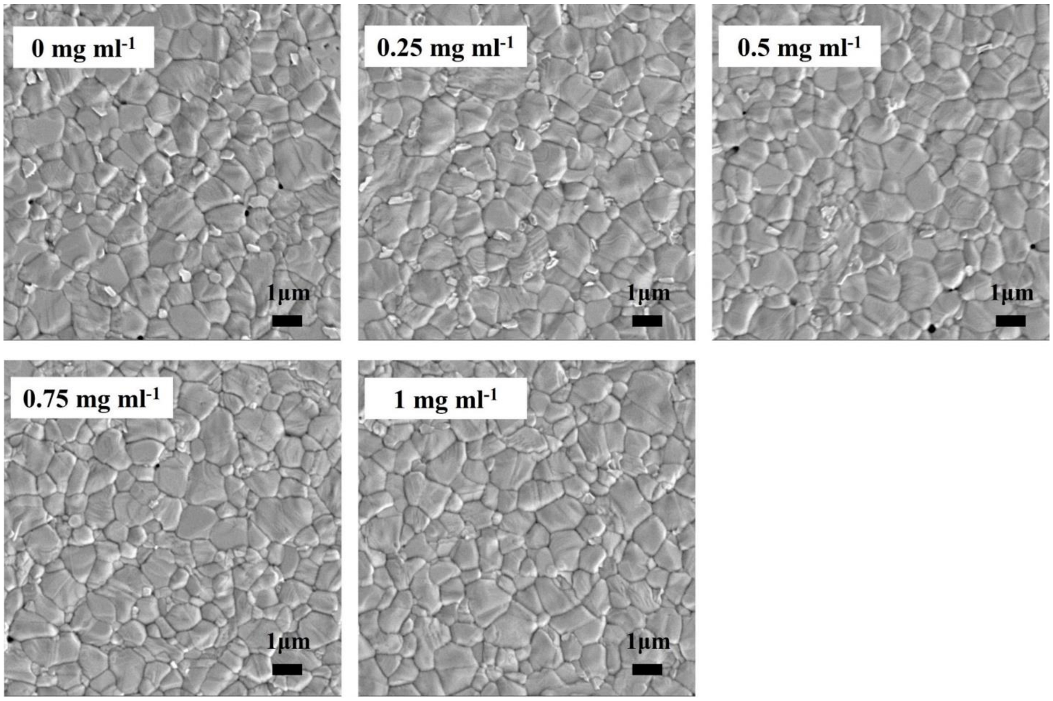

Figure 40 SEM image of PVK films on SnO_2 with PbS coating of different concetartions after annealing at 140 ^{o}C for 10 min.

Herein, the effect of PbS QD coating of SnO_2 and PVK films has been concluded, as illustrated in Figure 41a. Firstly, before coating PbS QDs, which is (I), the dominant defects of bare SnO_2 is $V_O^{\cdot\cdot}$ and the surface of SnO_2 film has the high density of Sn dangling bonds. [116] These defects are easily adsorb the water and hydroxyl groups in the air and can also be treated as the electron trapping sites.[117] After coating PbS QDs, at the stage (II), XPS results in Figure 1c and d have shown a strong interaction between PbS and SnO_2. The coating of SnO_2 films by the octahedral PbS QDs passivate these Sn dangling bonds with the sulfide atoms on (001) facet.[118] And the Pb atoms on(111) face of PbS QDs were passivated by OA ligand. Subsequently, after PbS QDs were contacted with dropped PVK precursor, the OA ligands are desorbed in polar solvent DMF and exchanged by halide ions on the PbS surface. Afterwards, the PVK can grow on the surface of PbS QDs at the stage (III). To confirm the nucleation of PbS QDs in the PVK fabrication procedure. Intermediate PVK phase without annealing were investigated to discover the details of the growth process. As shown in Figure 41b and d, the XRD patterns and morphology images of as-deposited intermediate PVK films on SnO_2 and SnO_2-PbS (0.5mg/ml) are presented. With a small amount of stabilizers ($MAPbBr_3$ and MACl) added in the PVK precursor solution, the coated films are crystallized to α-phase of $FAPbI_3$ without thermal annealing.[29, 30] However, the pre-coated PbS QDs on SnO_2 can further promotes the crystallization to cubic α phase and decreases the content of residual non-photoactive hexagonal δ $FAPbI_3$ phase from the precursor solution.[119] The stabilization of intermediate phase is vital for the final PVK quality because the δ phase will inhibit the complete phase transformation to α PVK and easily induce the degradation.[29, 30] This supports our claim that the PbS QD interlayer helps the crystallization of α-phase in the as-deposited film. Likewise, the morphology of intermediate PVK films on SnO_2 and PbS-QD/SnO_2 is shown. It can be seen that the initial growth stage of PVK on SnO_2-PbS is more induced and active. The more compact and uniform film without any pores indicate more nucleation due to the PbS QDs. Thereafter, the more crystallization and compact grains of the final PVK films can be obtained after annealing in Figure 41c and e. Experimental observations indicate that the PbS QDs facilitates the growth and crystallization processes of the PVK film using the antisolvent-assisted solution-based method.

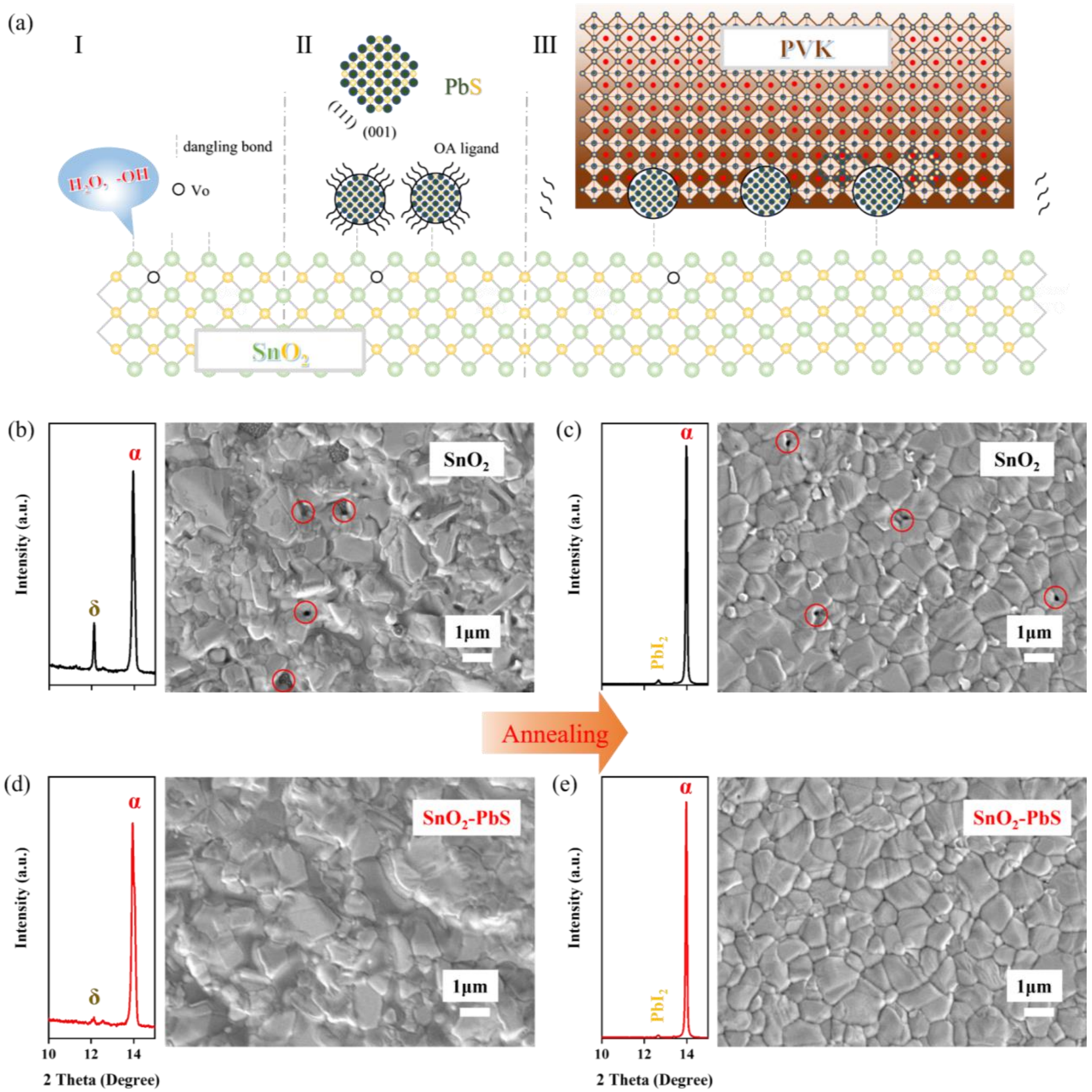

Figure 41 (a) Schematics of the effect of PbS QDs on the PVK growth mechanism; XRD patterns and top-view SEM images of the intermediate PVK on (b) SnO_2 and (d) SnO_2-PbS before annealing and final PVK on (c) SnO_2 and (e) SnO_2-PbS ETLs after annealing at 140 °C for 10min.

4.4 Fabrication of perovskite solar cells

To investigate the PbS coating on the final device performance, we fabricated PSCs with the structure of FTO/ETL/PVK/Spiro-OMeTAD/Au (Figure 42). The thickness of the PVK film is about 500 nm, exhibiting a vertical grain boundary. The direct connection of ETL and HTL by a single grain offers benefits for charge transport within the active layer.[120]

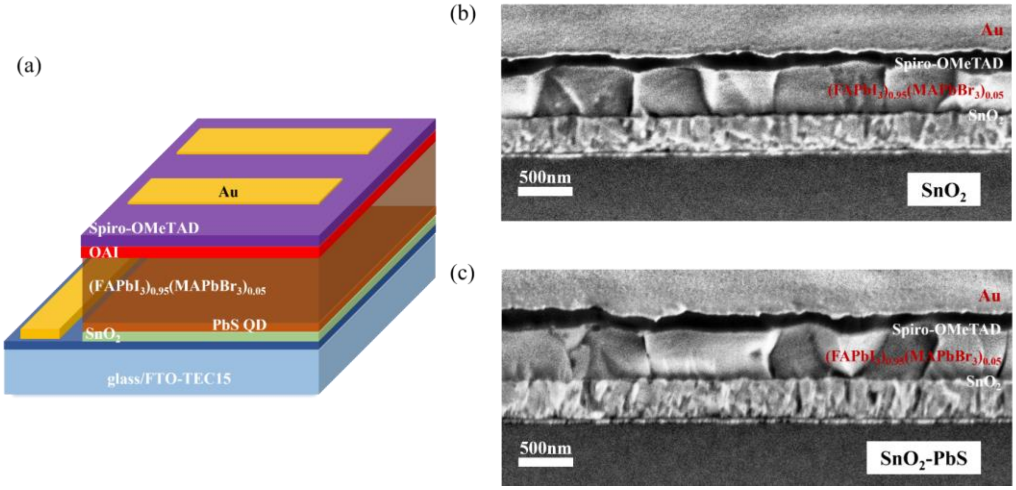

Figure 42 (a) Schematic of the n-i-p configuration of the PSC devices. Cross-section of PSC devices employing (b) SnO_2 and (c) SnO_2-PbS ETLs.

Figure 43 shows the J-V curves of PSCs using coating solutions of different PbS concentrations. Photovoltaic performance parameters of these devices are summarized in Table 6. As the PbS QD concentration increases from 0 to 0.5 mg/ml, the performance is continually improved. However, the device performance degrades when further rising the concentration. This is because the excess PbS QDs are hardly fully mixed with PVK precursor, and the OA ligands which cannot be exchanged by iodide ions. The residual OA molecules are insulated and will terminate the electron transfer.[121]

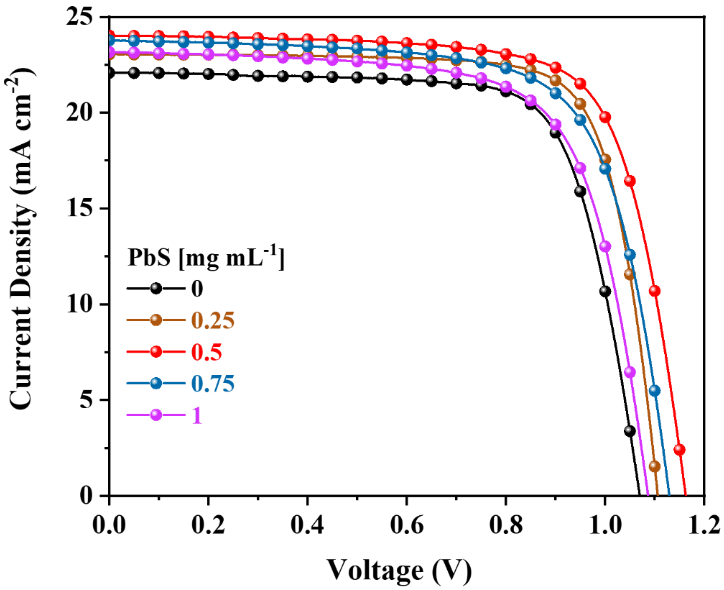

Figure 43 ***J-V*** **curves of device with PbS coating of different concentrations.**

Table 6 Photovoltaic parameters of PSC devices using different concentrations of PbS QD solution.

Concentration [mg/ml]	J_{SC} [mA/cm^2]	V_{OC} [V]	FF [%]	PCE [%]
0	22.08	1.070	73.6	17.40
0.25	23.04	1.106	77.0	19.62
0.5	24.02	1.144	78.1	21.66
0.75	23.77	1.129	70.5	18.92
1	23.16	1.086	69.9	17.60

The J-V curves of control PSC on SnO_2 and champion PSC on SnO_2-PbS are compared in Figure 44a: J_{SC} and V_{OC} are improved from 22.08 to 24.02 mA/cm^2 and 1.070 to 1.144 V, with the hysteresis index (HI) reduced from 0.27 to 0.04. Consequently, the PCE increased from 17.40 to 21.66% (Table 7). Figure 44b shows the external quantum efficiency (EQE) spectra of the control and champion devices. The champion device shows constant improvement of IPCE from 300 to 800 nm. An integrated current density is 21.32 mA/cm^2 for SnO_2-based PSCs and 23.67 mA/cm^2 for SnO_2-PbS-based PSCs, which suggests that better electron extraction is responsible for the improved PCE. This indicates that the PbS QD coating suppresses the nonradiative carrier recombination within PVK/ETL.

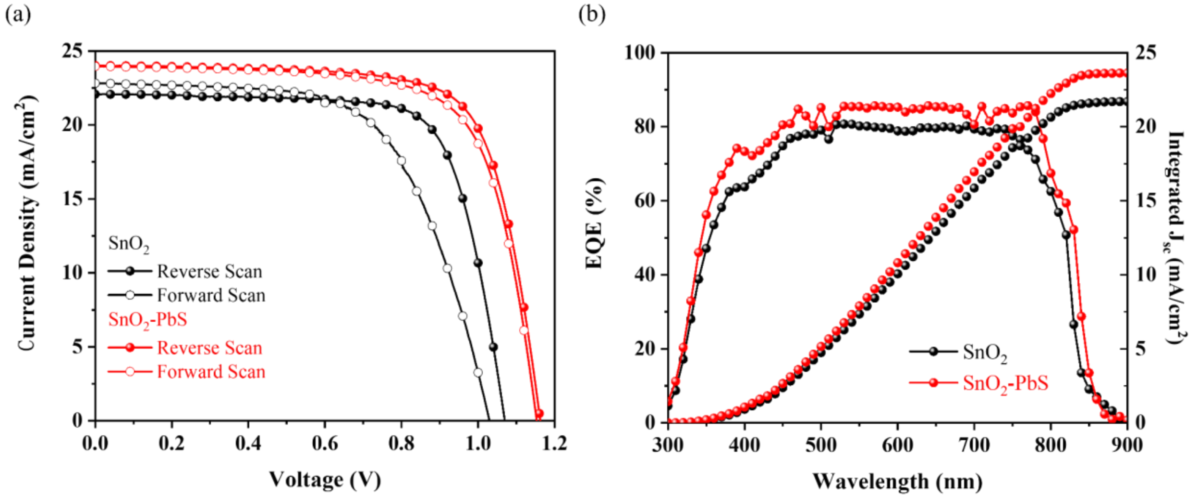

Figure 44 (a) A typical device under reverse and forward scan of PSC devices on SnO_2 and SnO_2-PbS and (b) EQE of and corresponding integrated J_{SC}.

Table 7 Photovoltaic parameters of the champion PSC device on different ETLs in reverse and forward scans

ETLs	direction	J_{SC} [mA cm^{-2}]	V_{OC} [V]	FF [%]	PCE [%]	HI
SnO_2	reverse	22.08	1.070	73.6	17.40	0.27
	forward	22.825	1.029	62.1	14.58	
SnO_2-PbS	reverse	24.02	1.144	78.1	21.66	0.04
	forward	23.56	1.135	75.7	20.26	

The reproducibility of PSCs based on pristine SnO_2 and SnO_2-PbS are shown in Figure 45. The average PCE increased significantly from 15.03 to 18.25%. The performance improvement is mainly due to the increase of V_{OC} and J_{SC}, indicating a substantial defects termination on the perovskite surface. The slight deviation of the device performance indicates high device reproducibility.

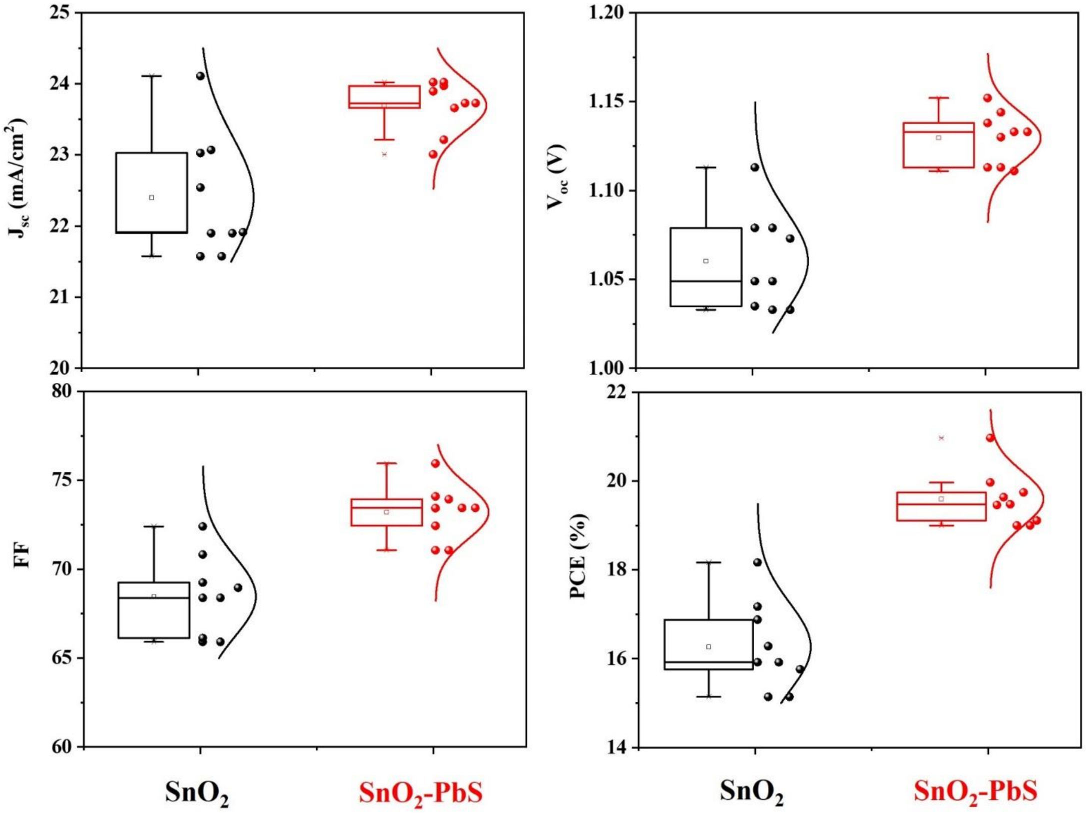

Figure 45 Statistical distributions of the J_{SC}, V_{OC}, FF and PCE of PSC devices with SnO_2 (black) and SnO_2-PbS (red) ETLs.

According to the reverse *J-V* curve of SnO_2-PbS based PSC in Figure 44a, the current density and voltage at MPP is 22.06 mA/cm^2 and 0.95 V, respectively. The steady-state current density of PbS assisted device tracking at maximum power point (MPP) displayed in Figure 46a is 22.06 mA/cm^2 corresponded a stabilized power output of 20.97% at a voltage of 0.95 V. It shows that PSCs using SnO_2-PbS ETL exhibit a more stable current density over time at MPP. Nevertheless, the power output of the control device (SnO_2 based PSC) decreases over time. However, there seems to be difficulty stabilizing the power output for the control device, probably due to severe ion migration within the device. Similar behavior was observed when the ion migration was severe in PSC devices.[122] The reducing of iodine migration can be attributed to the strong attraction of lead atoms on the (111) facets of PbS QDs.[123]

In addition to enhanced devices performance, our devices also show better stability than reference devices (Figure 46b). The SnO_2-PbS-based PSCs can retain over 93% of their initial efficiency after 1000 h in ambient air (relative humidity~30%). In contrast, the control devices retain ~88% of their initial efficiency, probably due to the better crystallization and less ion migration within the $FAPbI_3$ perovskite film.

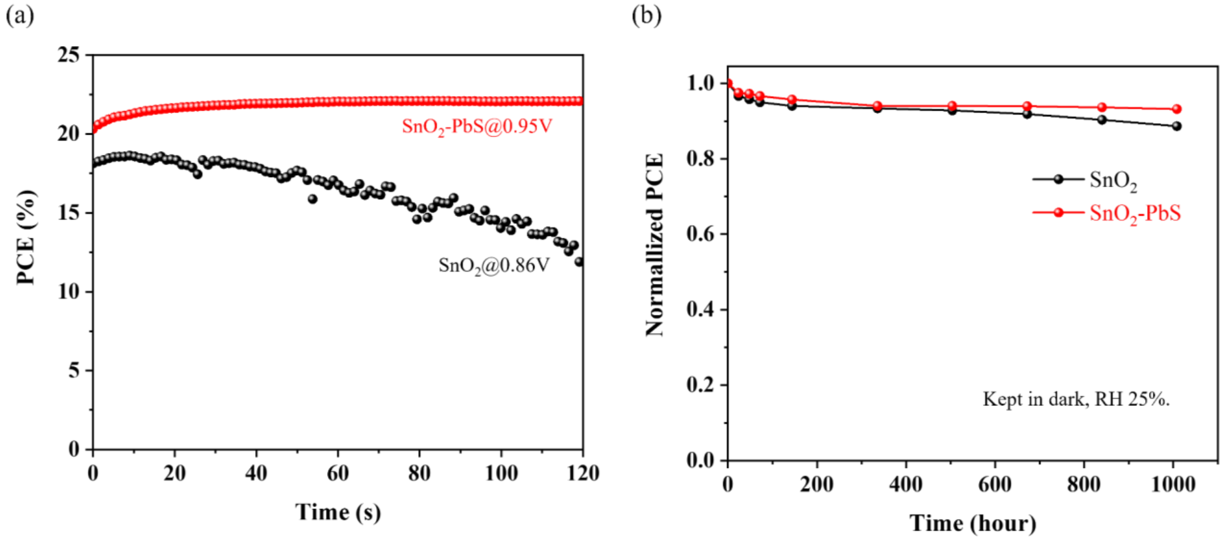

Figure 46 (a) Steady-state current density versus time for the devices measured at MPP and (b) PCE evolution of the unencapsulated devices exposed to the humidity of 30 RH% at room temperature in the dark condition.

4.5 Carrier Extraction and Recombination

So far, the results have confirmed that simply PbS QD as interlayer made a progress in accomplishing the final chemical state and films with high morphological quality. Another indispensable role of surface/interface passivation is to collect the electrons generated by light absorption of the PVK layer constructively while reducing the non-radiative recombination across the interface. To quantitatively estimate the bulk trap density in perovskite films, the space-charge-limited-current (SCLC) technique was applied to the electron-only devices with a structure of FTO/pristine SnO_2 (and SnO_2-PbS)/PVK/phenyl-C_{61}-butyric acid methyl ester (PCBM)/Ag as shown in Figure 47. The trap density N_t is calculated from the equation[110, 113]

$$V_{TFL} = eN_tL^2/2\varepsilon\varepsilon_0 \tag{4-1}$$

where e is the elementary charge, L is the thickness of perovskite film, ε is the relative dielectric constant, ε_0 is the vacuum permittivity, and V_{TFL} is the trap-filling limit voltage. The trap densities are calculated to be 1.24×10^{16} and 6.06×10^{15} cm^{-3} for perovskite films grown on SnO_2 and SnO_2-PbS composite, respectively.

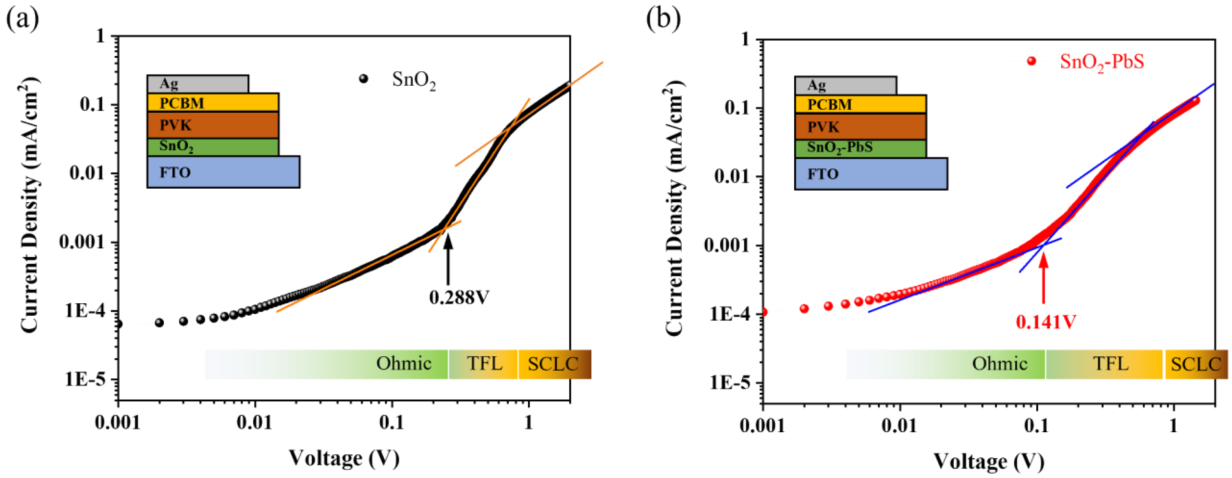

Figure 47 SCLC measurements of electron-only devices (inset) fabricated employing (a) SnO_2 and (b) SnO_2-PbS.

In order to gain further insight into the charge transport mechanism, the charge transfer processes in the perovskite devices were studied in detail. A lower dark saturation-current density was also observed for the target solar cell in Figure 48a, in agreement with the lower trap density for perovskite films grown on SnO_2-PbS. The carrier recombination rate in the PSCs was evaluated by the V_{OC} decay measurements. Figure 48b shows the V_{OC} decay curves of the PSCs based on different ETLs. It is apparent that the device on SnO_2-PbS exhibits the slower V_{OC} decay time compared to the devices based on pristine SnO_2, indicating that the devices with SnO_2-PbS have the lower charge recombination rate and the longest carrier lifetime, consistent with the highest V_{OC} for the device based on SnO_2-PbS by J-V measurements.[124]

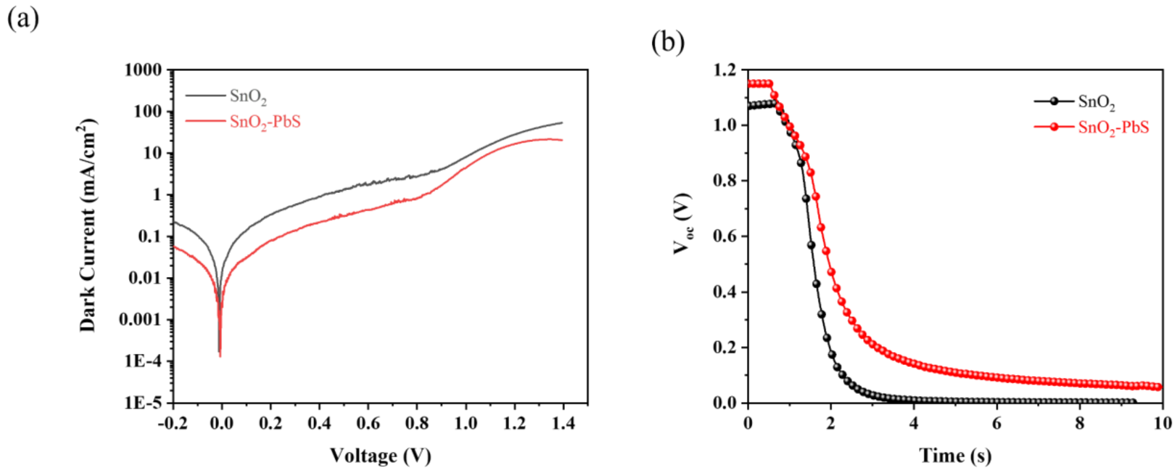

Figure 48 (a) Dark JV and (b) V_{OC} decay measurements of PSC devices with SnO_2 (black) and SnO_2-PbS (red) ETLs.

Figure 49 shows J_{SC} and V_{OC} versus light intensity of the PSCs using different ETLs. The J_{SC} line appears that all devices show a fitting correlation with the slopes very close to 1, indicating that the band-to-band recombination in the working devices is negligible. Figure 49b shows the light intensity dependent V_{OC} measurements for the PSCs. For both the control and target cells, they measured Voc was linearly dependent on the logarithm of the light intensity.[113] The diode ideality factor n_{id}, deduced from the slope described by $n_{id}k_BT/q$, where k_B is the Boltzmann constant and T is temperature, was 1.84 and 1.33 for the SnO_2 and SnO_2-PbS-based cells, respectively. The reduced n_{id} contributed to the increased FF of the target cell, as the FF critically depends on the n_{id}.[18] The reduced n_{id} is consistent with the SCLC, dark J-V and V_{OC} decay measurements, and unambiguously supporting the conclusion of reduced nonradiative recombination of the target PSC using SnO_2-PbS ETL. The substantial reduction of the trap-assisted nonradiative recombination is the main reason for the reduced V_{oc} deficit of our target device.

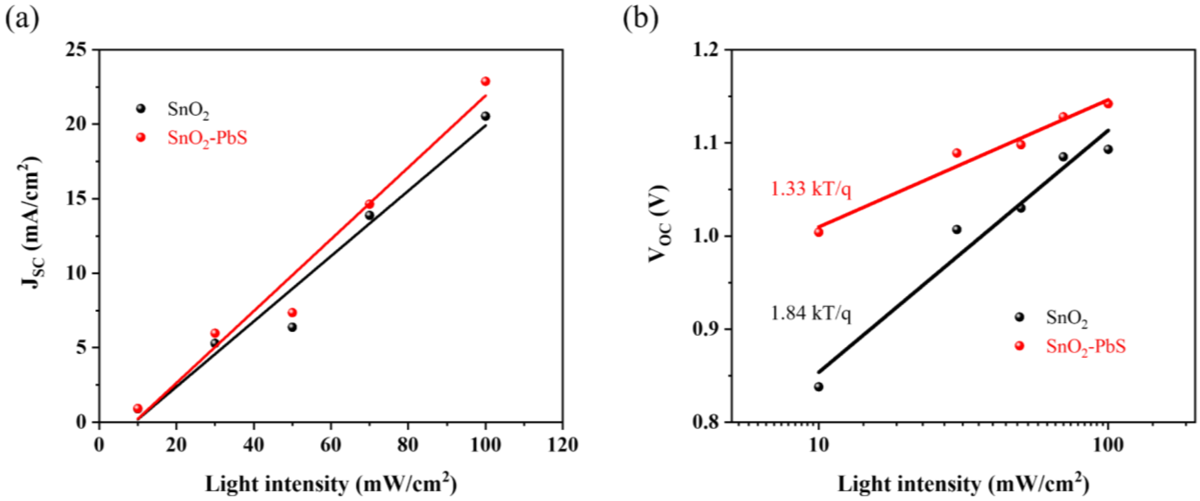

Figure 49 Light-dependent (a) V_{OC} and (b) J_{SC} for the PSCs with different ETLs.

The electrical impedance spectroscopy (EIS) was employed to extract transfer resistance in the PSC devices. Figure 50 shows the Nyquist plots of the devices using different ETLs measured at bias of 0.9V under dark conditions, with the equivalent circuit shown inset. It is known that in the EIS analysis, the high-frequency component is the signature of the transfer resistance (R_{tr}) and the low-frequency one for the recombination resistance (R_{rec}). The numerical fitting gives the device parameters, as listed in Table 8. Apparently, compared to control PSCs based on pristine SnO_2, the device with SnO_2-PbS shows a smaller R_{tr} of 120 Ω and a much larger R_{rec} of 513 Ω. The improved R_{rec} effectively resists charge recombination, which is in agreement with the observations discussed above. Combined, all the results confirm the more effective ETL SnO_2 with PbS coating for the planar-type PSC.

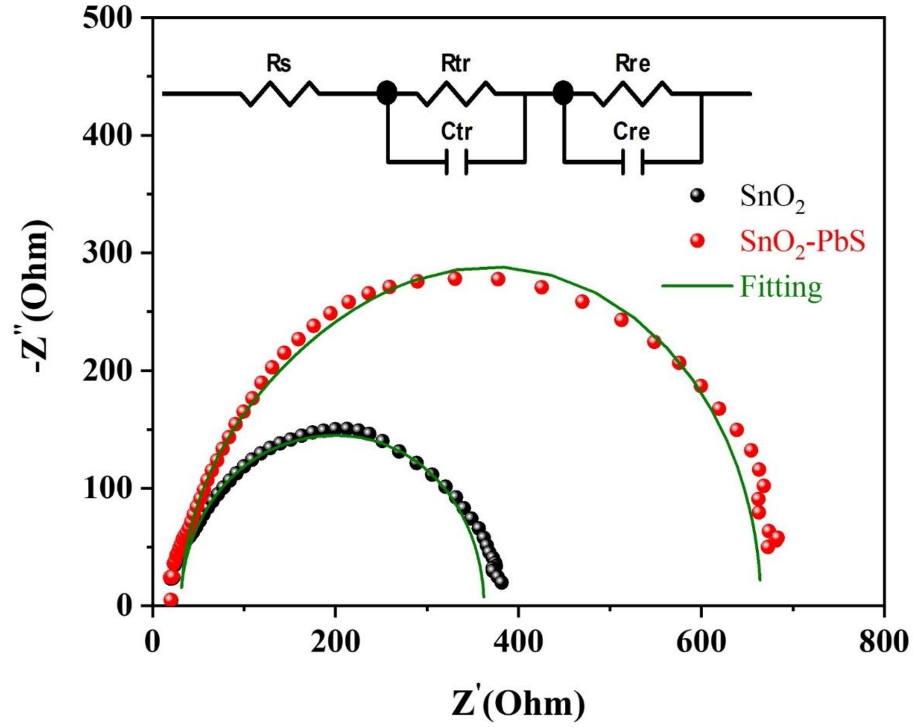

Figure 50 Impedence spectra for the PSCs with different ETLs.

Table 8 EIS spectra analysis

ETL	R_s [Ω]	R_{tr} [Ω]	C_{tr} [F]	R_{rec} [Ω]	C_{rec} [F]
SnO_2	30.49	150.8	3.7×10^{-8}	180.9	9.1×10^{-8}
SnO_2-PbS	31.23	120.9	5.5×10^{-8}	512.7	4.8×10^{-8}

4.6 Conclusion

We demonstrate that the PbS QD coating is an effective way to engineer the interface between SnO_2 and PVK and improve the performance of the n-i-p type PSC employing SnO_2 ETL. PbS QDs are well attached to the surface of SnO_2 and considerably decrease the interfacial trapping sites. In addition, PbS QDs promote the growth of columnar $FAPbI_3$ grains by providing more nucleation sites and suppressing the formation of the second phase. They contribute to enhancing carrier kinetics and stability of the PSC. PSC on PbS QD-SnO_2 exhibits J_{SC} and V_{OC} of 24.02 mA/cm^2 and 1.14V, resulting in a champion PCE of 21.66%. Moreover, the PCE of PSC on PbS QD-SnO_2 maintained more than 90% of the initial PCE after 1000 hours. This facile strategy utilizing PbS QD provides a path toward high-performance PSC on SnO_2 ETL.

5.0 Hybrid Perovskite Photocathode with Mo_2C Co-catalyst

5.1 Background and Motivation

Solar-driven water splitting has great potential to address a burgeoning need for green hydrogen production which will solve the pressing social issues such as fuel shortage, environmental pollution, and global warming.[125, 126] Materials for solar-fuel conversion require a wide bandgap to absorb visible and IR light [27], good charge separation and transportation abilities, low-cost manufacturing process, exceptional hydrogen evolution reaction (HER), and excellent operation stability.[126, 128]

Transition metal oxide and sulfide semiconductors have been extensively explored for solar-driven photoelectrochemical (PEC) systems due to their proper band structures which can harvest the sunlight and catalyze the water splitting to hydrogen and oxygen.[129] However, these materials such as TiO_2,[130] V_2O_5,[131] $SrTiO_3$,[132] CdS[133] have relatively large bandgap (2.5-3.5 eV) which mainly absorb the UV and blue portion of solar radiation (only 8-10% of incident solar energy). By contrast, recently emerging halide perovskite materials such as $CH_3NH_3PbI_3$ has a smaller bandgap (1.4-1.5 eV) and thus absorb a large portion of the solar energy. Incident photon-to-current efficiency (IPCE) of perovskite solar cells (PSCs) is over 80% in the visible range and output voltage of PSCs is over 1 V.[69, 134] Moreover, the halide perovskite materials have long carrier lifetime and charge diffusion length, leading to excellent carrier collection efficiency.[134-136] Because of these superior advantages, the efficiency of perovskite solar cells (PSC) has dramatically increased from 3.8% to 25.6% for the last decade.[12, 72, 137] However, there are problems applying the halide perovskite materials to the PEC application. They have low stability in a corrosive electrolyte system and poor catalytic efficiency. Therefore, several studies have been aimed to protect the halide perovskite layer from rapid degradation and enhance not only the stability but also the catalytic property. Water-resistant and/or electron conductive materials such as InBiSn alloy,[136] aluminum (Al)-doped ZnO (AZO) layer,[138] Ti foil,[135] ALD TiO_2,[139] and multiple carbon-derived films[140, 141] are tested to develop the stable perovskite photoelectrodes for PEC. On the other hand, to improve the catalytic ability of the perovskite photoanodes, co-catalysts boosting the water splitting have been implemented to the PEC system.[69, 136, 140] Most of perovskite-based PEC studies employed a thin platinum (Pt) layer as the catalyst due to the outstanding catalytic property of Pt and the compatibility of the e-beam deposition process with the vulnerable halide perovskite materials.[135, 136, 139] However, the e-beam process is hard to promote and apply on many earth-abundant catalysts. Very recently, more affordable HER co-catalyst including CoP and $FeNi(OH)_x$, are connected to the polymer encapsulated PSCs using metal.[69] Nevertheless, there are still few works directly combining the low-cost catalysts with the encapsulation layers through a simple method.

Therefore, we employed a dual functional assemble layer comprising commercial pure Ti foil (0.032mm thick, 99.7% metal basis) and Mo_2C nanoparticles on hybrid perovskite photocathodes, bridging the boundary between the perovskite PVs and the non-noble catalysts. This design can encapsulate the perovskite layer, assist electron transport, and catalyser-splitting. Ti and its alloys are widely demonstrated as high-quality structural materials for fuel and energy panels due to their high strength, low density, and excellent electrochemical stability. Moreover, is a promising and cheap HER catalyst candidate due to its unique surface electronic structure and recently gained great research attention. Lai et. al. successfully decreased the overpotential of the Ru doped Mo_2C electrocatalyst to 15 mV due to the excellent catalytic activity of Ru element (the

Gibbs free energy of Ru-H bond is very close to the free energy of Pt-H bond in the centre of HER volcanic map).[142]

In this study, we have demonstrated that the integration of Mo_2C nanoparticle coated Ti foil to PSCs is a simple and effective way to obtain PEC device with both excellent stability and catalytic performance. By optimizing the catalytic performance of the Mo_2C, the photoelectric performance of the PSC device can be well transferred to the photocathode. The hybrid integrating $CH_3NH_3PbI_3$ based photocathode shows a good photocurrent density of 14 mA/cm^2 at 0V versus (vs.) reversible hydrogen electrode (RHE) and can maintain over 60% of the initial performance over 10 h in 0.5M H_2SO_4 electrolyte solution under continuous 1 sun illumination, which is comparable to the state-of-the-art perovskite photocathode with Pt, as shown in Table 9. This is a facile and versatile method to integrate noble metal free and earth abundant catalyst into the perovskite photoelectrodes for further development of the solar fuel system.

Table 9 State-of-the-art Perovskite based Photocathode

Photocathode Configuration	Onset Potential (V) (at current density of 10mA/cm^2)	Photocurrent Density at 0V vs. RHE (mA/cm^2)	Stability (h)
ITO/NiO$_x$/Cs$_{0.05}$(MA$_{0.17}$FA$_{0.83}$)$_{0.95}$Pb(I$_{0.83}$Br$_{0.17}$)$_3$/PCBM/AZO/FM/Pt	0.38	14.3	18[138]
FTO/PEDOT:PSS/CH$_3$NH$_3$PbI$_3$/PCBM/PEIE/Ag/FM/Pt	--	9.8	1[136]
ITO/PEDOT:PSS/Cs$_{0.05}$(MA$_{0.17}$FA$_{0.83}$)$_{0.95}$Pb(I$_{0.83}$Br$_{0.17}$)$_3$/PCBM/ALD TiO$_2$/Pt	0.68	10.5	2[139]
ITO/NiO$_x$/MAPbI$_3$/PCBM/Ag/Ti Foil/Pt	0.64	18	12[135]

5.2 Experimental

5.2.1 Inverted Perovskite Solar Cell Fabrication

The solar cell was an inverted p-i-n structural configuration. Etched FTO glass substrates (TEC 7, 7Ω/sq, MSE Supplies) were ultrasonically cleaned by acetone, deionized water, and ethanol in sequence followed by 15 min UV-O$_3$ treatment for surface adsorption removal. Hole transport layer was a polymeric NiO$_x$. 10nm Ni layer was E-beam deposited on FTO followed by atmosphere oxidation at 550 ^{o}C for 6h. Then, 3mg/ml PTAA in toluene (Sigma-Aldrich) was spin-coated on the surface of NiO$_x$ at 4000 rpm for 30 s and heat at 100 ^{o}C for 10 min. Perovskite precursor solution was synthesized by dissolving 159mg MAI (Greatcell) and 461 mg PbI_2 (Sigma-Aldrich) in the mixed solvent of 76μl DMSO and 580μl DMF (Sigma-Aldrich). 50μl was dropped and spin-coated at 4000 rpm for 25s. After 9 s of the spinning, 0.5ml diethyl ether (Sigma-Aldrich) was dropped to remove the redundant DMSO. After spin coating, the film was annealed at 60 ^{o}C for 3 min and 100 ^{o}C for 20 min in sequence. Then, $PC_{60}BM$ (20mg/ml in di-chlorobenzene) was coated on perovskite at 2000 rpm and a very thin BCP layer was deposited on it for passivation. Then, 80nm Ag layer was coated on the top of the structure by E-beam system for electrode or passive layer for photocathode fabrication in the next.

5.2.2 Co-catalyst Mo_2C based Nanoparticle Synthesis

Mo-based precursor nanoparticle synthesis was obtained through a microwave-assisted solvothermal (MWSV) method. $MoCl_5$ (0.4g/ml in Ethanol) was mixed in urea and transferred into a Teflon tube for the microwave reaction at 400 W. The hydrothermal reaction was conducted at 150 ^{o}C for 10 minutes to obtain the precursor. For the synthesis of Mo_2C/GO and Ti doped Mo_2C/GO, the Mo source was mixed with 3wt.% graphene oxide (GO), GO and $TiCl_4$ in the solution before the MWSV. Subsequently, the powders were annealed in N_2 at 800 ^{o}C for 180 min. And the amorphous precursor was crystallized into Mo_2C (MC), Mo_2C/GO (MCG) and Ti doped Mo_2C/GO (TMCG) nanoparticles.

5.2.3 Perovskite Photocathode Integration

As-synthesized three kinds of Mo_2C based nanoparticles were mixed with 2 wt.% cellulous and terpineol and printed on Ti foil. Then the printed films were annealed at 250 ^{o}C to remove residual organics. Then, the coated Ti foil was attached on the top of the PSC device fabricated before using silver conductive paste with a blade. To dry the silver conductive paste then whole device was dried in the vacuum oven at 60 ^oC for over 30min.

5.2.4 Characterizations and Measurements

The surface morphology of samples was measured using a scanning electron microscope (SEM, SEM-ZEISS Sigma500 VP). The crystal structure was examined by X-ray diffraction (XRD, Bruker D8 XRD system) using Cu Kα radiation ($\lambda = 0.15406$ nm) as the radiation source.

The PV measurement was conducted using a CHI660D potential station. Device photocurrent density-voltage (*J*-*V*) curves were measured with a Keithley 2400 digital source meter under 1 sun illumination. The dark *J-V* measurement was also performed by this Keithley 2400 digital source meter under dark state to extract the trap state density with the basic p-i-n structure. The incident photon-to-current efficiency (IPCE) spectrum was measured with the TracQ Basic Spectroscopy system (MKS Instruments, Inc) in the DC mode without any voltage bias. J-V measurements were performed in 0.5 M H_2SO_4 (pH=0.33) using a CHI660D potential station. Photo-electrochemistry and electrochemistry measurements were conducted using a three-electrode configuration: perovskite working photocathode, Ag/AgCl reference electrode, and a rod-type carbon counter electrode. Epoxy resin was used to seal other parts of the device to protect the electrochemical cells from mechanical damage.

5.3 Co-catalyst of Mo_2C

Figure 51 shows the basic working principle and photocathode configuration of this PEC system and the corresponding three kinds of catalyst utilized here: pristine Mo_2C (MC), Mo_2C/GO (MCG) and Ti-Mo_2C/GO (TMCG). A versatile and facile method was used to prepare a perovskite photocathode which is compatible with nanoparticle catalyst coating. It consists of an inverted p-i-n structural PSC and a Mo_2C nanoparticle coated Ti foil. With the goal of waterproof and catalyst integration, as-synthesized Mo_2C based nanoparticles are coated on a commercial Ti foil. A cellulose-catalyst paste mixture is printed and annealed at 400°C to form a porous Mo_2C layer. Two components are bonded using Ag paste following the previous work.[135] The device is illuminated from the FTO substrate so that photogenerated electrons move toward Ti foil and reduce H^+ ions in water.

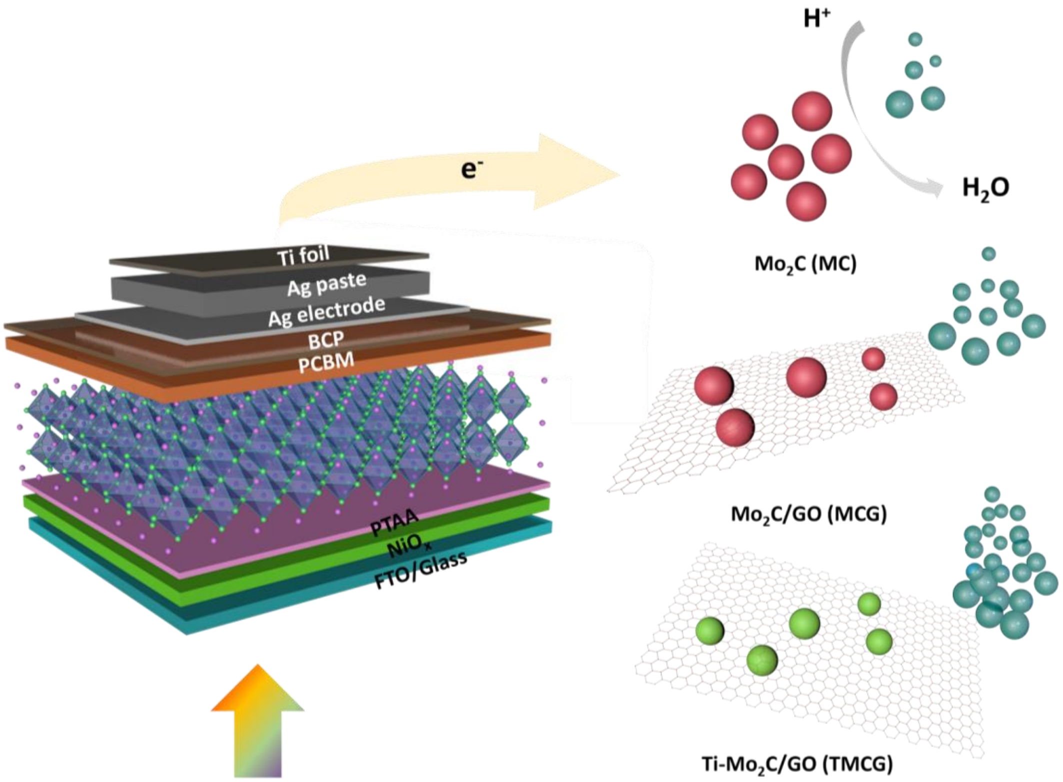

Figure 51 Schematic of representative solar driven hydrogen evolution configuration with $CH_3NH_3PbI_3$ perovskite.

Three kinds of Mo_2C based catalyst nanoparticles are synthesized here as shown in Figure 52a-c: rGO incorporated by the microwave-assisted solvothermal (MWSV) method from MG nanoparticles with 20nm diameter to MCG and TMCG nanoparticles with 10nm. The incorporation of graphene not only better disperse the nanoparticles with reducing particle size but provide good conductivity in the whole catalytic structure. Furthermore, based on the HER thermodynamic calculation, Ti element was chosen to dope into the Mo_2C molecular among a series of transition metal based on the calculation. Ti doping introducing thermoneutral sites are expected to be more HER active than that on the pristine β-Mo_2C (011) by $\Delta G_H = -0.1$ eV as shown in Figure 52d.

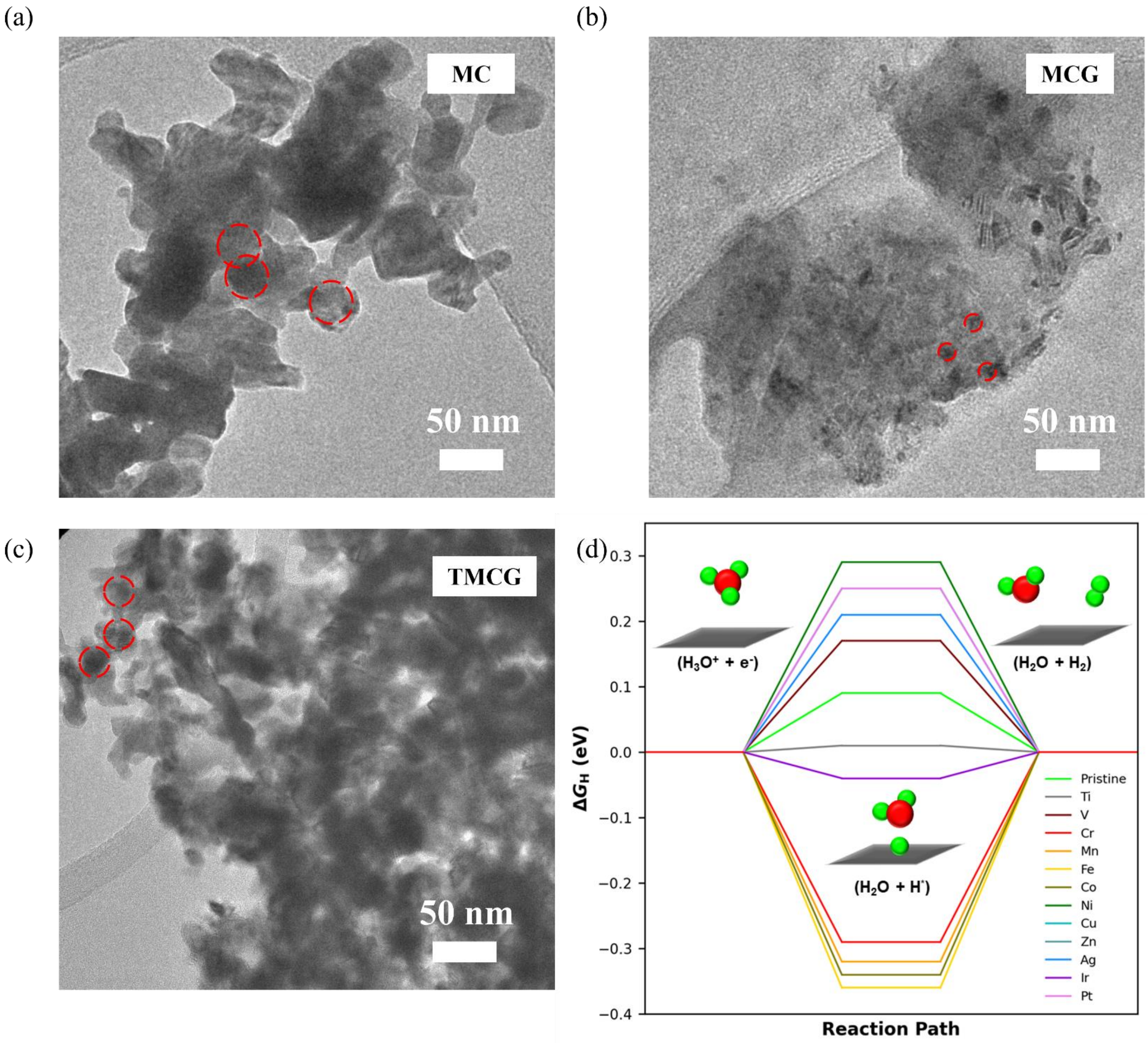

Figure 52 TEM micrographs of representative Mo_2C based catalysts: (a) pure Mo_2C (MC), (b) Mo_2C/GO (MCG), (c) Ti-Mo_2C/GO(TMCG) and (d) thermodynamic representation of the HER reaction pathway. (Reproduced with permission from 143. Copyright 2022 American Chemical Society.)

Figure 53 a and b show the crystal structure of $CH_3NH_3PbI_3$ deposited on FTO substrate. The compact morphology and uniform size of 300nm of PVK confirmed a good quality of film deposition. Further, the XRD peaks positing at 14.1°, 24.5°, 28.5° corresponding to (110), (202), (220) plane of tetragonal phase.[144] Correspondingly, the UV-vis absorbance of the perovskite layer on glass is shown in Figure 53c. At the wavelength from 500 nm to 800 nm, most incident UV-visible light is harvested. The estimated bandgap of the perovskite layer is 1.58 eV, which agrees perfectly with that of α-phase and the PL emission peak at the wavelength of 784 nm.[136, 145]

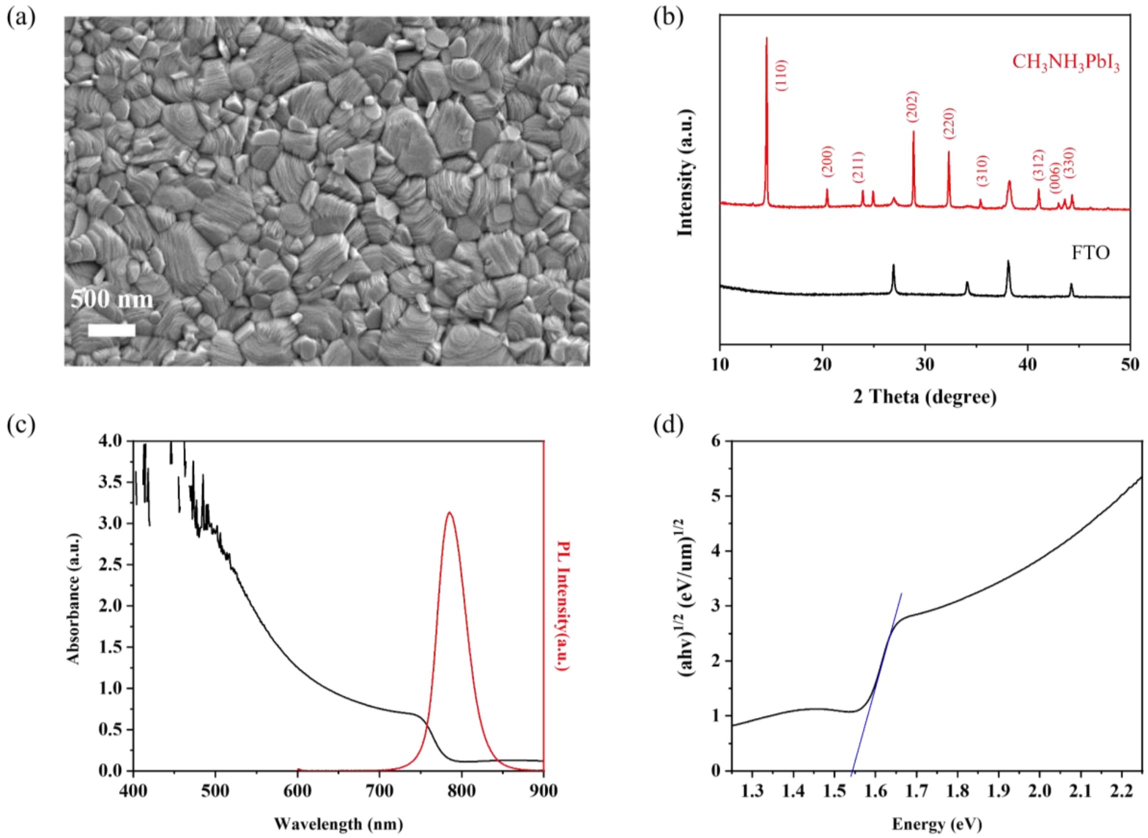

Figure 53 (a) SEM image and (b) XRD spectra of the $CH_3NH_3PbI_3$ layer deposited on FTO substrate. (c) Optical absorbance and PL spectra of $CH_3NH_3PbI_3$ thin film and (d) corresponding calculated Tacu's plot of $CH_3NH_3PbI_3$ thin film on glass. The estimated band gap is around 1.58 eV.

A corresponding cross-section SEM image of the PSC is shown in Figure 54a. A 20 nm thick poly[bis(4-phenyl)(2,4,6-trimethylphenyl)amine] (PTAA)/NiO multilayer is a hole transport layer (HTL). Methylammonium lead triiodide ($CH_3NH_3PbI_3$ denoted as $MAPbI_3$) is a light absorber. Bathocuproine (BCP) doped phenyl-C61-butyric acid methyl ester (PCBM) is an electric transport layer (ETL). To complete the fabrication of the PSC part of the PEC device, 80nm think Ag layer is deposited on top of PCBM layer. As shown in Figure 54a and b, light is incident through HTL of PSCs where light is converted to electrons and holes. Electrons are subsequently extracted to Mo_2C based catalyst for HER. The PV performance of the PSC was measured under simulated AM 1.5 G solar light (100 mW/cm^2). The current density-voltage (*J*-*V*) curve in Figure 54c showed that the typical device yielded a power conversional efficiency (PCE) of 15.18% with a short-circuit current density (J_{SC}) of 20.81mA/cm^2, an open-circuit voltage (V_{OC}) of 1.084 V, and a fill factor (FF) of 67.5%. The corresponding IPCE was more than 80% in a broad region from 350 to 750 nm (Figure 54d), consistent with the results of UV-Vis spectra and J-V curve.

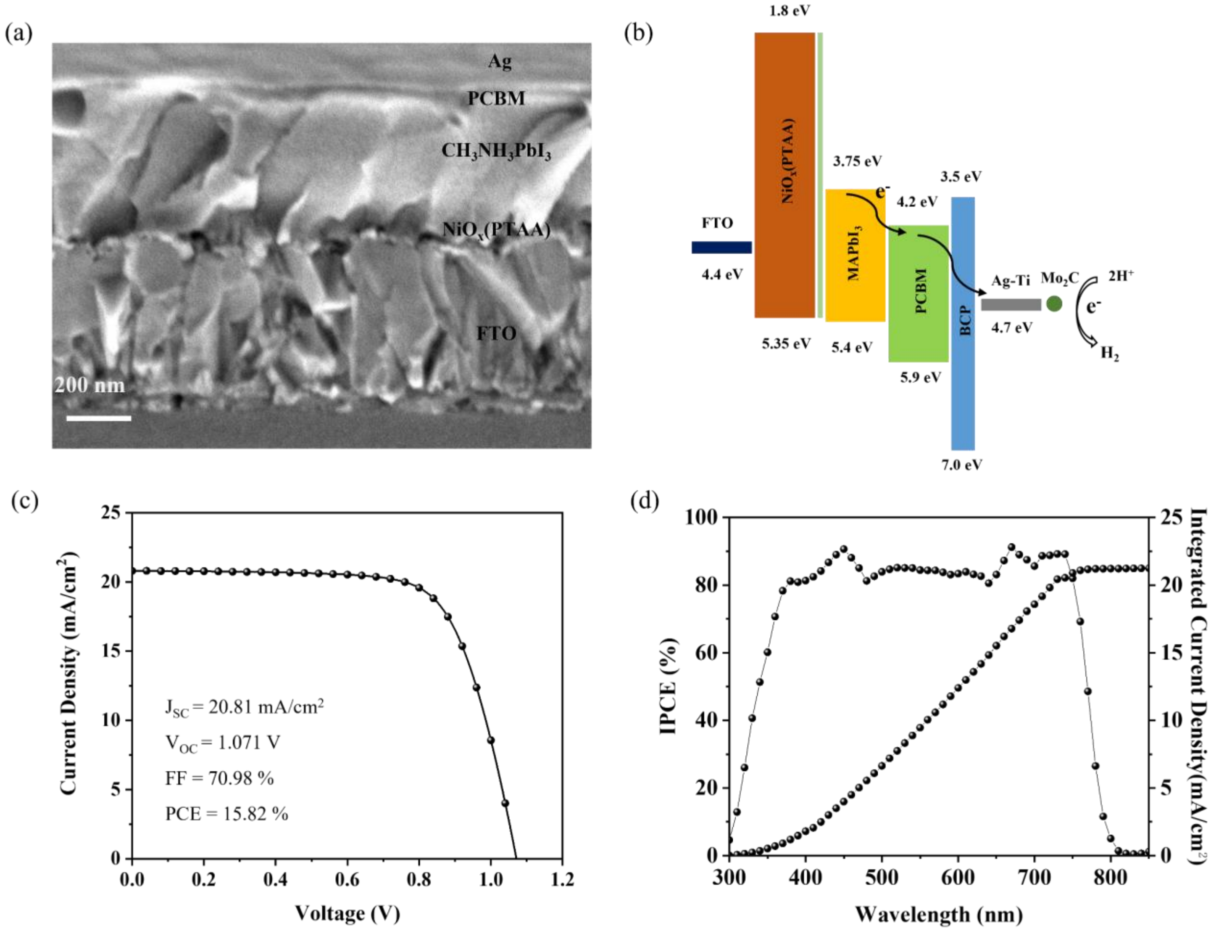

Figure 54 (a) SEM image of cross-sectional PSC structure and (b) energy diagram for photo-electrocatalytic hydrogen evolution. (c) Representative *J-V* curve of a PSC device recorded under 1 sun (100 mW/cm^2) and (d) IPCE spectra for the PSC of the same configuration.

The electrochemical HER performance of three kinds of Mo_2C based catalysts were evaluated using a standard three-electrode configuration in 0.5 M H_2SO_4 solution. The linear sweep voltaic (LSV) scan curves and corresponding Tafel plots were shown in Figure 55. As expected, the electrocatalytic activity increases as the trend of MC<MCG <TMCG, demonstrating that overall enhancement of catalyst comes from the introducing of GO and Ti element doping. Bare Mo_2C exhibits a metallic electronic structure like the Pt but shows a relatively low onset overpotential of 365mV to reach the current density of 10mA/cm^2. The introducing of the GO can

improve its conductivity, suppressing the carrier recombination and accelerating the electron transfer[146] and thus the onset overpotential can be improved to 125 mV. Further, it is worth noting that TMCG owns a more superior performance with the overpotential at 89 mV, which is 36 mV lower than Mo_2C-GO without Ti doping. To probe the HER kinetics of the catalysts, Tafel plots were fitted to the Tafel equation ($\eta=a+b\log(j)$), where b is the Tafel slope. As shown in Figure 55b, the bare Mo_2C catalyst exhibits a Tafel slope of 174 mV/dec. The Tafel slopes of MCG and TMCG are 120 mV/dec and 74mV/dec, respectively. The lower Tafel value suggest a higher HER rate and favorable kinetics with GO and Ti incorporation. [147, 148] In addition, Tafel slope falling within the range of 40~120 mV/dec indicating a Volmer-Heyrovsky mechanism working on the surface of the catalyst and the rate of the discharge step is consistent to desorption process. The exchange current density (j_o) was calculated by extrapolating the Tafel plot to an overpotential of 0V, which might profoundly reflect the intrinsic electrochemical reaction rate. As expected, the TMCG exhibits a j_o of 10mA/cm^2, which is much higher than those of MC and MCG.

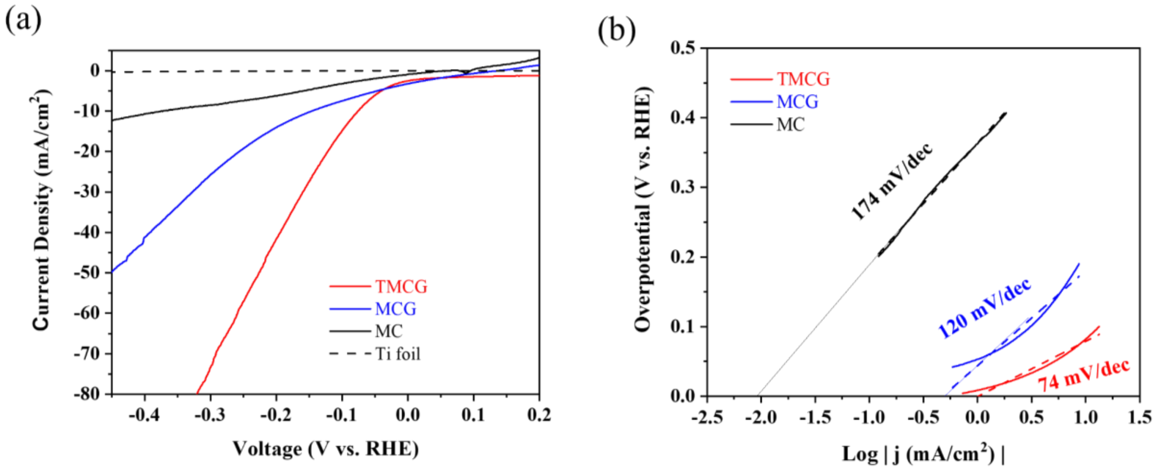

Figure 55 Electrocatalytic performance of Mo_2C based catalyst. (a) LSV of pristine MC, MCG and TMCG particles in 0.5M H_2SO_4 at a scan rate of 100mV/s and (b) the corresponding Tafel plots.

The Tafel plots derived from polarization curves are always affected by factors such as different choices of overpotential regions and different methods of IR compensation [142, 148]. Therefore, we further performed electrochemical surface area (ECSA) and electrochemical impedance spectroscopy (EIS) measurements to further explore the HER kinetics. Owing to the unclear capacitive behaviors of carbides, accurate ECSAs cannot be measured directly.[148] Double-layer capacitance (C_{dl}), which is proportional to the ECSA, was measured to provide a relative comparison.[149] Derived from the cyclic voltammograms (CV) with varied scan rates, TMCG presented the highest C_{dl} of 8.75 mF/cm^2 among the Mo_2C based catalysts (Figure 56a). This can be partially attributed to the increases of the active specific surface area of the catalyst with abundant active sites for HER pathway. In addition, it is more rational to normalize the current density by C_{dl} so the intrinsic activity can be accessed. Remarkably, the higher values over TMCG compared to MC and MCG indicate the intrinsic optimization of active sites (Figure 56b). As proved by our previous simulation, the doping of Ti atoms in to Mo_2C structure can promote the dissociation of H_2O and coordinate the adjustment of the free energy of adsorption and desorption of the reaction intermediates and products to facilitate the reaction. Additionally, measurements identified a low R_{ct} on TMCG, confirming the rapid electron transport for H_2 evolution as shown in Figure 56c. Overall, our results indicate that the HER kinetics are significantly improved by doping Ti into Mo_2C and mixing GO with Mo_2C.

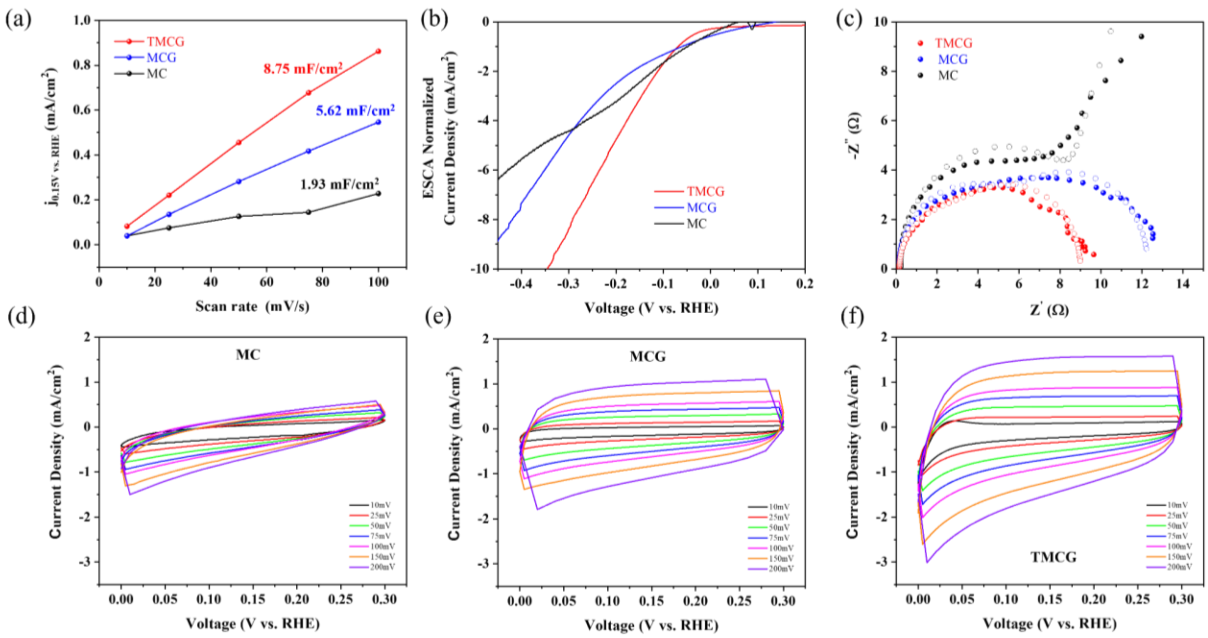

Figure 56 (a) Estimation of C_{dl} by plotting the current-density variation at 150 mV vs. RHE against the scan rate to fit a linear regression, (b) normalized LSV curves by C_{dl} and (c) Nyquist plots (scan rate=100 mV) of three catalysts. Electrocatalytic performance of catalyst and CV of (d) MC, (e) MCG and (f) TMCG catalysts in 0.5M H_2SO_4 at different scan rates.

5.4 Hybrid Perovskite based Photocathode

To fully evaluate the performance of the optimized device, the performance of the integrated perovskite hybrid photocathodes has been evaluated using a standard three-electrode configuration in 0.5 M H_2SO_4 solution. The catalysts and their effective contact with electrolyte also play an important role of in the PV driven electrolysis system. As schematic in Figure 57a, Figure 57b has shown the linear sweep voltaic (LSV) scan curves of photocathode with three kinds of Mo_2C at 20mV/s scan rate under 1 sun illumination and the bare photocathode protected by Ti foil without any catalyst has also drawn to compare. The hybrid photocathode combining with

TMCG has demonstrated the onset potential 514mV vs. RHE of the photocurrent density of 10mA/cm^2. Besides, at 0V vs. RHE, the photocurrent density can be up to 13.5 mA/cm^2. However, when the perovskite integrating with MCG and MC to form a photocathode, the photocurrent is decreased to 10.68 mA/cm^2 and 7.99 mA/cm^2, respectively. To better evaluate the practical potential of the photocathode, the applied bias photo-to-current conversion efficiency (ABPE) is derived from the current density-potential curve as shown in Figure 57b. The maximum power points of the hybrid perovskite photocathode with MC, MCG and TMCG was found to be at 325, 358 and 491mV versus RHE, respectively. At the peak point, the corresponding ideal ABPE are 1.63%, 2.97% and 5.17%, considerably increased by the GO incorporation and Ti doping, which can be comparable with Pt assisted photocathode.[12, 135] The increased PEC performance can be owed to the improved catalytic activity of the co-catalyst. Compared with the TMCG cathode without perovskite scanned in the same configuration, the onset potential shift is around 650mV, which can be seen as the potential provided by the PV device underneath. LSV curve exhibits relatively square waves under chopped light.

Figure 57c showed a similar square on-ff shape status under the chopped light for the optimized photocathode with TMCG catalyst. It can be proved that the improved proton reduction performance upon illumination is a photo effect. The quick switching and minimal transients further suggest rapid charge transport and minimal charging. Moreover, the response of the impressive photocurrent under different wavelength light at zero bias is shown in Figure 57d. The result represented a similar shape as the IPCE of the PV device, and the corresponding integrated current is 13.7 mA/cm^2, which is consistent with the result obtained from LSV curve. Taken together, our results demonstrate that the performance of the perovskite solar cells is successfully transferred to that of the PEC configuration. The photoelectron-catalytic property of our device utilizing the excellent Ti doped carbides complexing with GO (which is TMCG is compatible with those using Pt as co-catalyst.

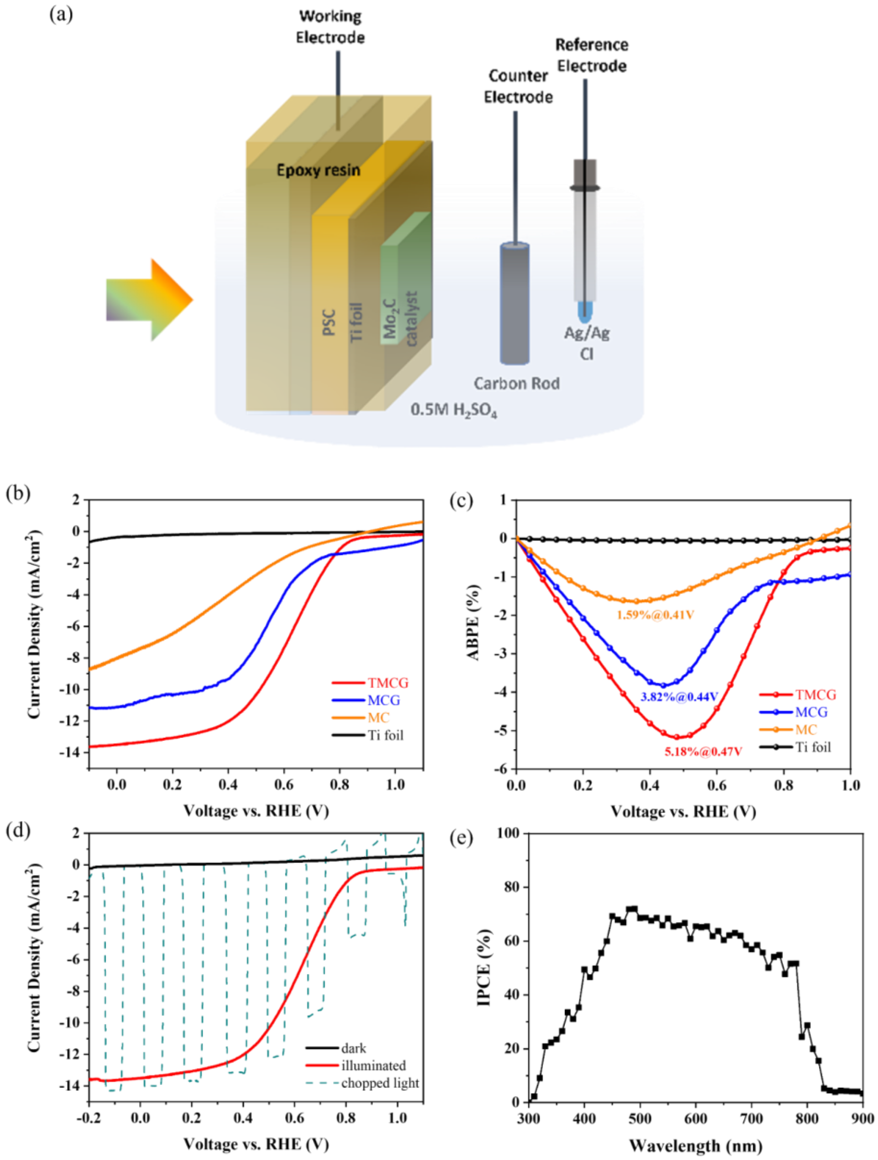

Figure 57 (a) Schematic of the PEC measurement usin three electrode system in 0.5M H_2SO_4. (b) The LSV comparison of photocathode with different catalysts: and (c) corresponding applied bias photon-to-current conversion efficiency (ABPE). (a) Optimzed photocathode with TMCG under dark, illumination under 1 sun (100 mW/cm^2) and chopped light and (b) corresponding IPCE measurement.

It is well known that a main remaining challenge in the development of the halide perovskite PVs is the stability of the devices.[150] Before the estimation of the stability of the hybrid photocathode, Figure 58 has shown the stability of this hybrid TMCG catalyst on Ti foil exhibiting an efficient working time over 16 hours. It suggests the dual layer for the catalyst can satisfy the requirement of the final long-term photoelectrodes.

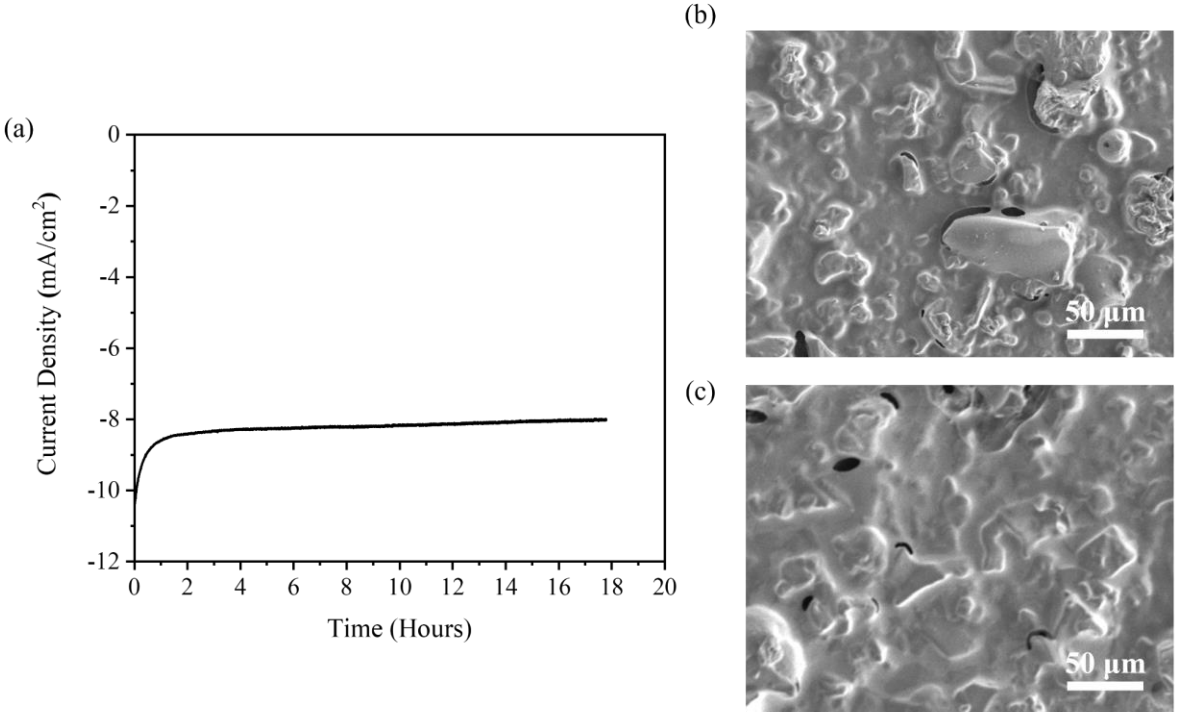

Figure 58 (a) Stability test of the coating foil at 98mV vs. RHE in 0.5M H_2SO_4; Morphology of TMCG electrode on Ti foil b) before and c) after the stability test.

Thereafter, the stability of the hybrid perovskite/TMCG photocathode device was also measured. A chronoamperometric measurement was performed under continuous one sun illumination and electrochemical bias (0 V vs RHE), as shown in Figure 59a. The photocathodes retained over 80% of the initial photocurrent density (13.5 mA/cm^2) after 11 h in a strong acidic solution. And for the first initial photoelectrochemical stability test, the photocurrent at 0 V vs.

RHE maintained over 90%. Even after 11hours, the final device can also show a good on-off sensibility under the chopped light, which indicates the excellent stability and potential for the further development of commercial hybrid photoelectrode Figure 59b.

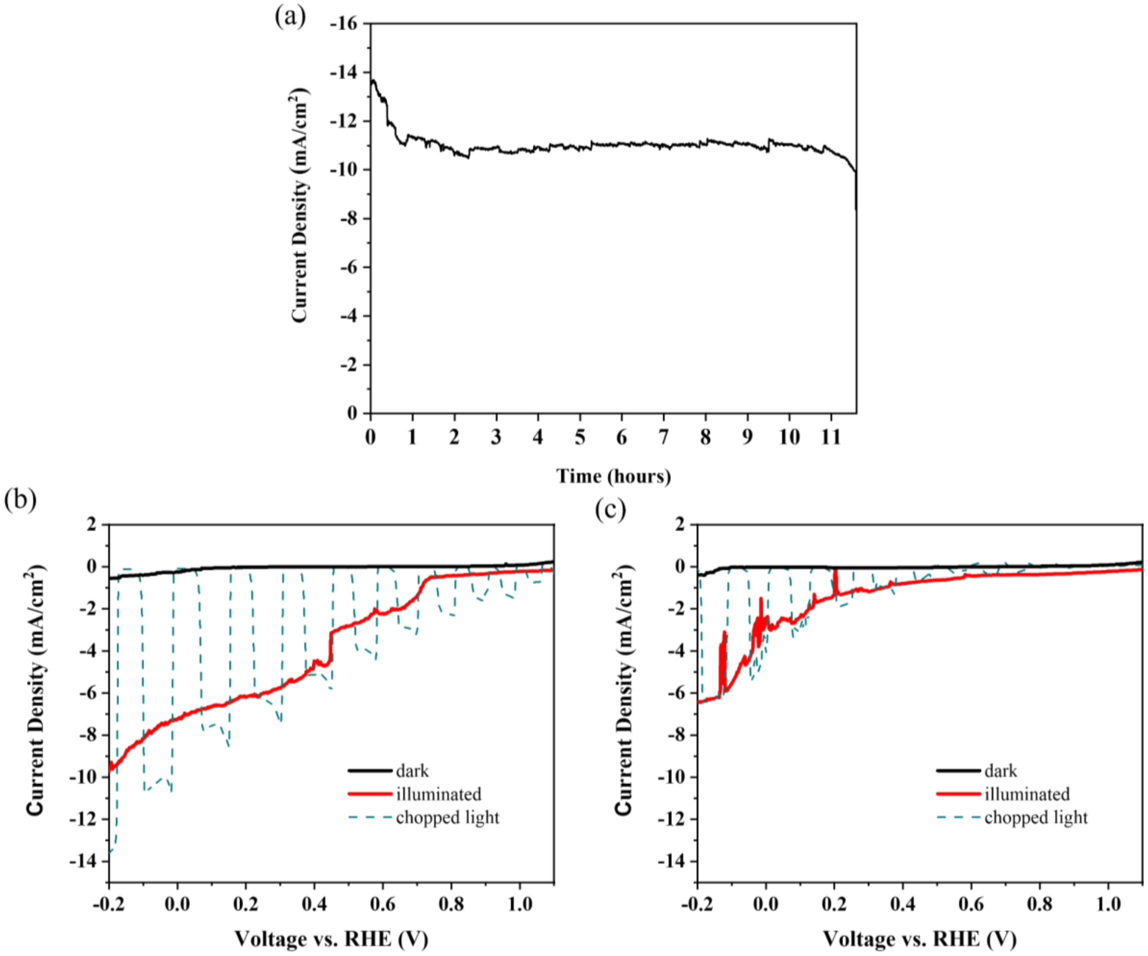

Figure 59 (a) Stability of the hybrid perovskite photocathode working under continuous 1 sun illumination. (The electrode potential was held at 0V vs. RHE.) and LSV of working hybrid perovskite photocathode under illumination under 1 sun in 0.5M H_2SO_4 after (b) 1 hour and (c) 11 hours.

5.5 Conclusion

The halide perovskite-based photoelectrode is a very promising candidate for solar-driven water splitting due to their appropriate bandgap (~1.58 eV) and rapid growing energy conversion efficiency which are comparable with commercial devices. However, the perovskite itself is quite moisture sensitive and easily degrades for further photoelectrode fabrication and light-harvesting directly in the solution. Herein, we have developed a versatile method to fabricate the $MAPbI_3$ based photocathode with non-noble metal co-catalyst for H_2 evolution directly immersed in acid. The perovskite was passivated by the Ti doped Mo_2C/GO (TMCG) catalyst coating metal layer. The effectively encapsulated photocathode has exhibited 13.5 mA/cm^2 without any bias and an onset potential as 0.68 V versus reversible hydrogen electrode. Furthermore, the whole device also demonstrated an excellent stability which can obtain over 60% photocurrent after more than 10 h continuous H_2 evolution in 0.5M H_2SO_4. This facile and versatile method can help remove the obstacle of the application of the halide perovskite in clean energy conversion, and more earth-abundant catalysts can be introduced to replace the noble metals for further potential low-cost photoelectrodes.

6.0 Summary and Outlooks

The objective of this study is to promote the development of organometal halide-based perovskite solar cell devices as well as their extended applications like water splitting. The study has shown the significant improvement of PSC devices by incident solar energy management and interfacial optimization with new kinds of transport layers. The incorporation of NIR plasmon particles into the photoactive perovskite layer enhanced the near-band edge (NBE) IPCE and corresponding short-cut current density of the PSC devices via increase of the light absorption and better carrier extraction in the long-wavelength light range. Besides the upgrade of the perovskite layer, the development of electron transport layer and better interface of PSCs are also of great importance. Better performance of $FAPbI_3$ based PSCs with planar SnO_2 ETL can be achieved with quantum dot-PbS layered modification. The interface layer can passivate the bottom-side trapping sites and stabilize the growth process of perovskite phase, resulting enlarged photocurrent, open-circuit voltage as well as small hysteresis and long stability. Extended application of the PSCs in the water splitting has also been investigated. Metal foil assemble assisted hybrid perovskite-based photocathode with Ti-Mo_2C/GO co-catalyst has shown a competitive photo-catalytic performance with Pt based co-catalyst and long stability in strong acid environment over 10hours.

In the future, one of the most important and urgent work on this topic is the evolution of the inverted structural PSC with extensive energy conversion efficiency and stability. Not only because the requirement for the inverted structural PSC in special application conditions (such as the electron extraction for HER in this paper), but compared with normal structure (FTO/ETL/perovskite/HTL/Au), inverted PSCs (FTO/HTL/perovskite/ETL/Ag) have some advantages such as simple fabrication process, negligible hysteresis effect, low-temperature solution preparation, and suitable for flexible solar cell fabrication. The basic principle for the inverted structure establishment is still in the direction of photoactive layer and interfacial layer development. We have also tried to replace $MAPbI_3$ with $FAPbI_3$ based perovskite due to their narrow bandgap and high phase stability. However, the photoactive α-$FAPbI_3$ fabrication from β-phase precursor-based solution requires higher annealing temperature at around 150^{o}C. Thus, the interfacial passivation is more necessary for layered compatibility. PTAA was applied for the polymeric passivation in the bottom side between NiO_x/perovskite. However, the traditional top side passivation of $FAPbI_3$ using 2D perovskite seems not applicable in the inverted PSCs. The PCBM solution cannot wet the passivation layer and thus continuous ETL layer is difficult to formed, which leads to non-ideal result. Herein, the development of a new feasible passivation strategy for our developing inverted PSC with the structure FTO/NiO_x(PTAA)/$FAPbI_3$/PCBM(BCP)/Ag should be investigated.

Appendix A Material and Chemicals

Appendix A.1 Perovskite Solar Cell

Titanium (IV) isopropoxide (TTIP, 97%), lead (II) iodide (PbI2, 99.999% trace metals basis, perovskite grade), dimethyl sulfoxide (DMSO, anhydrous, 99.9%), N, N-dimethylformamide (DMF, anhydrous, 99.8%), diethyl ether (anhydrous, ⩾99.7%), Acetone (⩾ 99.5%), chlorobenzene (anhydrous, 99.8%), 4-tert-butylpyridine (t-BP, 98%), bis(trifluoromethane)sulfonimide lithium salt (Li-TFSI, 99.95% trace metals basis) were purchased from Sigma-Aldrich. Methylammonium iodide (MAI ⩾99%) was purchased from the Great Cell Solar. TiO2 paste (electrode application, SC-HT040) was purchased from SHARECHEM. Spiro-MeOTAD (>99.8%) was purchased from Luminescence Technology Corp. 1-Butanol (>99.0%) was purchased from Tokyo Chemical Industry Co., Ltd. All chemicals and reagents were used as received without further purification. Fluorine-doped tin oxide (FTO) coated glass substrates (TEC7, 7-8 Ohm Sq-1) were purchased from MSE Supplies LLC.

Appendix A.2 SiO_2@Ag Core@Shell Particle

Ammonium hydroxide solution (28.0-30.0% NH3 basis), tetraethyl orthosilicate (TEOS, 98%), (3-Aminopropyl) trimethoxysilane (APTMS, 97%), tetrakis(hydroxymethyl)phosphonium chloride (THPC, 80% in H2O), gold (III) chloride hydrate (99.995% trace metals basis), silver nitrate (AgNO3 ⩾99.0%), formaldehyde solution (37%, stabilized with about 10% methanol for synthesis), Sodium hydroxide (NaOH, Technical, Spectrum™ Chemical), sodium sulfide (Na2S, anhydrous, Granular) were purchased from Fisher Scientific.

Appendix B Abbreviation List

organometal halide (OMH)

perovskite solar cell (PSC)

photovoltaic (PV)

Methylammonium lead halides ($MAPbI_3$)

Formamidinium lead halides ($FAPbI_3$)

power conversion efficiency (PCE)

silica@silver ($SiO_2@Ag$)

infrared (IR)

photoluminescence (PL)

Lead sulfide (PbS)

tin oxide (SnO_2)

electron transport layer (ETL)

ultraviolet (UV)

bandgap (E_g)

silicon (Si)

methylammonium lead bromine ($MAPbBr_3$)

hole transport layer (HTL)

scanning electron microscope (SEM)

titanium oxide (TiO_2)

electron mobility (μ_e)

space-charge-limited current (SCLC)

current-voltage (I-V)

shortcut-circuit current density (J_{SC})

incident-photon-to-current efficiency (IPCE)

external quantum efficiency (EQE)

open-circuit voltage (V_{OC})

localized surface plasmon resonance (LSPR)

atomic layered deposition (ALD)

hydrogen (H_2)

photoelectrochemical (PEC)

valence band (VB)

conductive band (CB)

electromagnetic (EM)

finite-difference time-domain (FDTD)

near-band-edge (NBE)

$SiO_2@Ag@Ag_2S$ (SAA)

Bibliography

(1) Celik, I.; Hosseinian Ahangharnejhad, R.; Song, Z.; Heben, M.; Apul, D. Emerging photovoltaic (PV) materials for a low carbon economy. *Energies* **2020**, *13*, 4131.

(2) Gielen, D.; Boshell, F.; Saygin, D.; Bazilian, M. D.; Wagner, N.; Gorini, R. The role of renewable energy in the global energy transformation. *Energy Strategy Rev.* **2019**, *24*, 38.

(3) Child, M.; Kemfert, C.; Bogdanov, D.; Breyer, C. Flexible electricity generation, grid exchange and storage for the transition to a 100% renewable energy system in Europe. *Renew. Energy* **2019**, *139*, 80.

(4) Meek, D.; Hatfield, J.; Howell, T.; Idso, S.; Reginato, R. A generalized relationship between photosynthetically active radiation and solar radiation. *J. Agronomy* **1984**, *76*, 939.

(5) Jiang, J.; Ling, C.; Xu, T.; Wang, W.; Niu, X.; Zafar, A.; Yan, Z.; Wang, X.; You, Y.; Sun, L. Defect Engineering for Modulating the Trap States in 2D Photoconductor. *Adv. Mater.* **2018**, *30*, 1804332.

(6) Fujiwara, H.; Kato, M.; Tamakoshi, M.; Miyadera, T.; Chikamatsu, M. Optical characteristics and operational principles of hybrid perovskite solar cells. *Phys. Status solidi (a)* **2018**, *215*, 1700730.

(7) Chen, J.; Park, N. G. Causes and solutions of recombination in perovskite solar cells. *Adv. Mater.* **2019**, *31*, 1803019.

(8) Marinova, N.; Valero, S.; Delgado, J. L. Organic and perovskite solar cells: Working principles, materials and interfaces. *J. Colloid Interface Sci.* **2017**, *488*, 373.

(9) Ehrler, B.; Alarcon-Llado, E.; Tabernig, S. W.; Veeken, T.; Garnett, E. C.; Polman, A. Photovoltaics reaching for the Shockley-Queisser limit. *ACS Energy Lett.* **2020**, *5*, 3029.

(10) Green, M. A. The path to 25% silicon solar cell efficiency: History of silicon cell evolution. *Prog. Photovolt.* **2009**, *17*, 183.

(11) Kojima, A.; Teshima, K.; Miyasaka, T.; Shirai, Y. Novel photoelectrochemical cell with mesoscopic electrodes sensitized by lead-halide compounds (2). *Meet. Abstr.* **2006,** *MA2006-02* 397.

(12) Kojima, A.; Teshima, K.; Shirai, Y.; Miyasaka, T. Organometal halide perovskites as visible-light sensitizers for photovoltaic cells. *J. Am. Chem. Soc.* **2009**, *131*, 6050.

(13) Kim, B.; Kim, J.; Park, N. First-principles identification of the charge-shifting mechanism and ferroelectricity in hybrid halide perovskites. *Sci. Rep.* **2020**, *10*, 1.

(14) Li, C.; Lu, X.; Ding, W.; Feng, L.; Gao, Y.; Guo, Z. Formability of ABX_3 (X = F, Cl, Br, I) halide perovskites. *Acta Crystallogr. B: Struct.* **2008**, *64*, 702.

(15) Green, M. A.; Ho-Baillie, A.; Snaith, H. J. The emergence of perovskite solar cells. *Nat. Photon.* **2014**, *8* (7), 506-514.

(16) Lu, H.; Liu, Y.; Ahlawat, P.; Mishra, A.; Tress, W. R.; Eickemeyer, F. T.; Yang, Y.; Fu, F.; Wang, Z.; Avalos, C. E. Vapor-assisted deposition of highly efficient, stable black-phase $FAPbI_3$ perovskite solar cells. *Science* **2020**, *370*, eabb8985.

(17) Jeong, M.; Choi, I. W.; Go, E. M.; Cho, Y.; Kim, M.; Lee, B.; Jeong, S.; Jo, Y.; Choi, H. W.; Lee, J. Stable perovskite solar cells with efficiency exceeding 24.8% and 0.3-V voltage loss. *Science* **2020**, *369*, 1615.

(18) Kim, M.; Jeong, J.; Lu, H.; Lee, T. K.; Eickemeyer, F. T.; Liu, Y.; Choi, I. W.; Choi, S. J.; Jo, Y.; Kim, H.-B. Conformal quantum dot-SnO_2 layers as electron transporters for efficient perovskite solar cells. *Science* **2022**, *375*, 302.

(19) Chueh, C.-C.; Li, C.-Z.; Jen, A. K.-Y. Recent progress and perspective in solution-processed Interfacial materials for efficient and stable polymer and organometal perovskite solar cells. *Energy Environ. Sci.* **2015**, *8*, 1160.

(20) Rong, Y.; Hu, Y.; Mei, A.; Tan, H.; Saidaminov, M. I.; Seok, S. I.; McGehee, M. D.; Sargent, E. H.; Han, H. Challenges for commercializing perovskite solar cells. *Science* **2018**, *361*, eaat8235.

(21) Kausar, A.; Sattar, A.; Xu, C.; Zhang, S.; Kang, Z.; Zhang, Y. Advent of alkali metal doping: a roadmap for the evolution of perovskite solar cells. *Chem. Soc. Rev.* **2021**, *50*, 2696.

(22) Sutherland, B. R.; Hoogland, S.; Adachi, M. M.; Kanjanaboos, P.; Wong, C. T.; McDowell, J. J.; Xu, J.; Voznyy, O.; Ning, Z.; Houtepen, A. J. Perovskite thin films via atomic layer deposition. *Adv. Mater.* **2015**, *27*, 53.

(23) Hwang, K.; Jung, Y. S.; Heo, Y. J.; Scholes, F. H.; Watkins, S. E.; Subbiah, J.; Jones, D. J.; Kim, D. Y.; Vak, D. Toward large scale roll-to-roll production of fully printed perovskite solar cells. *Adv. Mater.* **2015**, *27*, 1241.

(24) Taylor, A. D.; Sun, Q.; Goetz, K. P.; An, Q.; Schramm, T.; Hofstetter, Y.; Litterst, M.; Paulus, F.; Vaynzof, Y. A general approach to high-efficiency perovskite solar cells by any antisolvent. *Nat. Commun.* **2021**, *12*, 1.

(25) LaMer, V. K.; Dinegar, R. H. Theory, production and mechanism of formation of monodispersed hydrosols. *J. Am. Chem. Soc.* **1950**, *72*, 4847.

(26) Kirakosyan, A.; Kim, J.; Lee, S. W.; Swathi, I.; Yoon, S.-G.; Choi, J. Optical properties of colloidal $CH_3NH_3PbBr_3$ nanocrystals by controlled growth of lateral dimension. *Cryst. Growth Des.* **2017**, *17*, 794.

(27) Yan, K.; Long, M.; Zhang, T.; Wei, Z.; Chen, H.; Yang, S.; Xu, J. Hybrid halide perovskite solar cell precursors: colloidal chemistry and coordination engineering behind device processing for high efficiency. *J. Am. Chem. Soc.* **2015**, *137*, 4460.

(28) Wang, Z.; Zhou, Y.; Pang, S.; Xiao, Z.; Zhang, J.; Chai, W.; Xu, H.; Liu, Z.; Padture, N. P.; Cui, G. Additive-modulated evolution of $HC(NH_2)_2PbI_3$ black polymorph for mesoscopic perovskite solar cells. *Chem. Mater.* **2015**, *27*, 7149.

(29) Yang, G.; Zhang, H.; Li, G.; Fang, G. Stabilizer-assisted growth of formamdinium-based perovskites for highly efficient and stable planar solar cells with over 22% efficiency. *Nano Energy* **2019**, *63*, 103835.

(30) Kim, M.; Kim, G.-H.; Lee, T. K.; Choi, I. W.; Choi, H. W.; Jo, Y.; Yoon, Y. J.; Kim, J. W.; Lee, J.; Huh, D. Methylammonium chloride induces intermediate phase stabilization for efficient perovskite solar cells. *Joule* **2019**, *3*, 2179.

(31) Targhi, F. F.; Jalili, Y. S.; Kanjouri, F. $MAPbI_3$ and $FAPbI_3$ perovskites as solar cells: Case study on structural, electrical and optical properties. *Results Phys.* **2018**, *10*, 616-627.

(32) Jiang, Q., Zhang, L., Wang, H. et al. Enhanced electron extraction using SnO_2 for high-efficiency planar-structure $HC(NH_2)_2PbI_3$-based perovskite solar cells. *Nat. Energy* **2016,** 2, 16177.

(33) Noori, L.; Hoseinpour, V.; Shariatinia, Z. Optimization of TiO2 paste concentration employed as electron transport layers in fully ambient air processed perovskite solar cells with a low-cost architecture. *Ceram. Int.* **2022**, *48* (1), 320-336.

(34) Hui, W.; Yang, Y.; Xu, Q.; Gu, H.; Feng, S.; Su, Z.; Zhang, M.; Wang, J.; Li, X.; Fang, J. Red-carbon-quantum-dot-doped SnO2 composite with enhanced electron mobility for efficient and stable perovskite solar cells. *Adv. Mater.* **2020**, *32*, 1906374.

(35) Kim, S.; Yun, Y. J.; Kim, T.; Lee, C.; Ko, Y.; Jun, Y. Hydrolysis-Regulated Chemical Bath Deposition of Tin-Oxide-Based Electron Transport Layers for Efficient Perovskite Solar Cells with a Reduced Potential Loss. *Chem. Mater.* **2021**, *33*, 8194.

(36) Holman, Z. C.; Descoeudres, A.; De Wolf, S.; Ballif, C. Record infrared internal quantum efficiency in silicon heterojunction solar cells with dielectric/metal rear reflectors. *IEEE J. Photovolt.* **2013**, *3*, 1243.

(37) Ompong, D.; Singh, J. High open-circuit voltage in perovskite solar cells: The role of hole transport layer. *Org. Electron.* **2018**, *63*, 104.

(38) Song, S.; Kang, G.; Pyeon, L.; Lim, C.; Lee, G.-Y.; Park, T.; Choi, J. Systematically optimized bilayered electron transport layer for highly efficient planar perovskite solar cells (η= 21.1%). *ACS Energy Lett.* **2017**, *2*, 2667.

(39) Chen, P.; Bai, Y.; Wang, L. Minimizing voltage losses in perovskite solar cells. *Small Structures* **2021**, *2*, 2000050.

(40) Wu, C.; Xu, Q.-H. Stable and functionable mesoporous silica-coated gold nanorods as sensitive localized surface plasmon resonance (LSPR) nanosensors. *Langmuir* **2009**, *25*, 9441.

(41) Hammond, J. L.; Bhalla, N.; Rafiee, S. D.; Estrela, P. Localized surface plasmon resonance as a biosensing platform for developing countries. *Biosensors* **2014**, *4*, 172.

(42) Verger, F.; Pain, T.; Nazabal, V.; Boussard-Plédel, C.; Bureau, B.; Colas, F.; Rinnert, E.; Boukerma, K.; Compere, C.; Guilloux-Viry, M. Surface enhanced infrared absorption (SEIRA) spectroscopy using gold nanoparticles on As_2S_3 glass. *Sens. Actuators B Chem.* **2012**, *175*, 142.

(43) Hou, H., Wei, Y., Song, Y., Mi, L., Tang, M., Li, L., & Fan, Y. Metal Ions Play Different Roles in the Third-Order Nonlinear Optical Properties of d^{10} Metal-Organic Clusters. *Angew. Chem. Int* **2005,** *117*, 6221.

(44) Hao, F.; Sonnefraud, Y.; Dorpe, P. V.; Maier, S. A.; Halas, N. J.; Nordlander, P. Symmetry breaking in plasmonic nanocavities: subradiant LSPR sensing and a tunable Fano resonance. *Nano Lett.* **2008**, *8*, 3983.

(45) Pallavicini, P.; Chirico, G.; Collini, M.; Dacarro, G.; Donà, A.; D'alfonso, L.; Falqui, A.; Diaz-Fernandez, Y.; Freddi, S.; Garofalo, B. Synthesis of branched Au nanoparticles with tunable near-infrared LSPR using a zwitterionic surfactant. *Chem. Commun.* **2011**, *47*, 1315.

(46) Mortazavi, D.; Kouzani, A. Z.; Vernon, K. C. A resonance tunable and durable LSPR nano-particle sensor: Al_2O_3 capped silver nano-disks. *Prog. Electromagn. Res.* **2012**, *130*, 429.

(47) Chen, J.-J.; Wu, J. C.; Wu, P. C.; Tsai, D. P. Improved photocatalytic activity of shell-isolated plasmonic photocatalyst Au@ SiO_2/TiO_2 by promoted LSPR. *J. Phys. Chem. C* **2012**, *116*, 26535.

(48) Qu, Y.; Liu, F.; Wei, Y.; Gu, C.; Zhang, L.; Liu, Y. Forming ceria shell on Au-core by LSPR photothermal induced interface reaction. *Appl. Surf. Sci.* **2015**, *343*, 207.

(49) Oldenburg, S.; Averitt, R.; Westcott, S.; Halas, N. Nanoengineering of optical resonances. *Chem. Phys. Lett.* **1998**, *288*, 243.

(50) Peiris, S.; McMurtrie, J.; Zhu, H.-Y. Metal nanoparticle photocatalysts: emerging processes for green organic synthesis. *Catal. Sci. Technol.* **2016**, *6*, 320.

(51) Scaiano, J. C.; Stamplecoskie, K. G.; Hallett-Tapley, G. L. Photochemical Norrish type I reaction as a tool for metal nanoparticle synthesis: importance of proton coupled electron transfer. *Chem. Commun.* **2012**, *48*, 4798.

(52) Prodan, E.; Radloff, C.; Halas, N. J.; Nordlander, P. A hybridization model for the plasmon response of complex nanostructures. *science* **2003**, *302*, 419.

(53) Chan, K.; Wright, M.; Elumalai, N.; Uddin, A.; Pillai, S. Plasmonics in Organic and Perovskite Solar Cells: Optical and Electrical Effects. *Adv. Opt. Mater.* **2017**, *5*, 1600698.

(54) Laska, M.; Krzemińska, Z.; Kluczyk-Korch, K.; Schaadt, D.; Popko, E.; Jacak, W. A.; Jacak, J. E. Metallization of solar cells, exciton channel of plasmon photovoltaic effect in perovskite cells. *Nano Energy* **2020**, *75*, 104751.

(55) Yao, K.; Zhong, H.; Liu, Z.; Xiong, M.; Leng, S.; Zhang, J.; Xu, Y. X.; Wang, W.; Zhou, L.; Huang, H.; et al. Plasmonic Metal Nanoparticles with Core-Bishell Structure for High-Performance Organic and Perovskite Solar Cells. *ACS Nano* **2019**, *13*, 5397.

(56) Erwin, W. R.; Zarick, H. F.; Talbert, E. M.; Bardhan, R. Light trapping in mesoporous solar cells with plasmonic nanostructures. *Energy Environ. Sci.* **2016**, *9*, 1577.

(57) Liu, J.; Xiao, L.; Liu, Y.; Cao, L.; Shen, Z. Development of long-wavelength infrared detector and its space-based application requirements. *Chin. Phys. B* **2019**, *28*, 028504.

(58) Beltrán-Pérez, G.; López-Huerta, F.; Muñoz-Aguirre, S.; Castillo-Mixcóatl, J.; Palomino-Merino, R.; Lozada-Morales, R.; Portillo-Moreno, O. Fabrication and characterization of an optical fiber pH sensor using sol-gel deposited TiO_2 film doped with organic dyes. *Sens. Actuators B Chem.* **2006**, *120*, 74.

(59) Xie, Q.; Jiang, Y.-L.; Detavernier, C.; Deduytsche, D.; Van Meirhaeghe, R. L.; Ru, G.-P.; Li, B.-Z.; Qu, X.-P. Atomic layer deposition of Ti O_2 from tetrakis-dimethyl-amido titanium or Ti isopropoxide precursors and H_2O. *J. Appl. Phys.* **2007**, *102*, 083521.

(60) Zhu, S.; Pang, F.; Huang, S.; Zou, F.; Dong, Y.; Wang, T. High sensitivity refractive index sensor based on adiabatic tapered optical fiber deposited with nanofilm by ALD. *Opt. Express* **2015**, *23*, 13880.

(61) Mahltig, B.; Gutmann, E.; Meyer, D.; Reibold, M.; Bund, A.; Böttcher, H. Thermal preparation and stabilization of crystalline silver particles in SiO_2-based coating solutions. *J. Sol-Gel Sci. Technol.* **2009**, *49*, 202.

(62) Yong, K.-T.; Sahoo, Y.; Swihart, M. T.; Prasad, P. N. Synthesis and plasmonic properties of silver and gold nanoshells on polystyrene cores of different size and of gold-silver core-shell nanostructures. *Colloids Surf. A Physicochem. Eng. Asp.* **2006**, *290*, 89.

(63) Ohodnicki, P.; Wuenschell, J.; Buric, M.; Liu, Y.; Lee, J.-K. Optical-fiber based hydrogen sensing at high temperature using ALD coated oxide sensing layers. *Fiber Optic Sensors and Applications XVII*, **2021**,*11739*, 83.

(64) Zeng, M.; Li, Y. Recent advances in heterogeneous electrocatalysts for the hydrogen evolution reaction. *J. Mater. Chem. A* **2015**, *3*, 14942.

(65) Jafari, T.; Moharreri, E.; Amin, A. S.; Miao, R.; Song, W.; Suib, S. L. Photocatalytic water splitting-the untamed dream: a review of recent advances. *Molecules* **2016**, *21*, 900.

(66) Pérez-Larios, A.; Lopez, R.; Hernandez-Gordillo, A.; Tzompantzi, F.; Gómez, R.; Torres-Guerra, L. M. Improved hydrogen production from water splitting using TiO_2-ZnO mixed oxides photocatalysts. *Fuel* **2012**, *100*, 139.

(67) Wang, H.; Lu, Z.; Xu, S.; Kong, D.; Cha, J. J.; Zheng, G.; Hsu, P.-C.; Yan, K.; Bradshaw, D.; Prinz, F. B. Electrochemical tuning of vertically aligned MoS_2 nanofilms and its application in improving hydrogen evolution reaction. *PNAS* **2013**, *110*, 19701.

(68) Nørskov, J. K.; Bligaard, T.; Logadottir, A.; Kitchin, J.; Chen, J. G.; Pandelov, S.; Stimming, U. Trends in the exchange current for hydrogen evolution. *J. Electrochem. Soc.* **2005**, *152*, J23.

(69) Chen, H.; Zhang, M.; Tran-Phu, T.; Bo, R.; Shi, L.; Di Bernardo, I.; Bing, J.; Pan, J.; Singh, S.; Lipton-Duffin, J.; Wu, T.; Amal, R.; Huang, S.; Ho-Baillie, A. W. Y.; Tricoli, A. Integrating Low-Cost Earth-Abundant Co-Catalysts with Encapsulated Perovskite Solar Cells for Efficient and Stable Overall Solar Water Splitting. *Adv. Funct. Mater.* **2020**, *31*, 2008245.

(70) Liu, Y.; Lee, S.; Yin, Y.; Li, M.; Cotlet, M.; Nam, C. Y.; Lee, J. K. Near-Band-Edge Enhancement in Perovskite Solar Cells via Tunable Surface Plasmons. *Adv. Opt. Mater.* **2022**, 2201116.

(71) Yoo, J. J.; Seo, G.; Chua, M. R.; Park, T. G.; Lu, Y.; Rotermund, F.; Kim, Y.-K.; Moon, C. S.; Jeon, N. J.; Correa-Baena, J.-P. Efficient perovskite solar cells via improved carrier management. *Nature* **2021**, *590*, 587.

(72) Jeong, J.; Kim, M.; Seo, J.; Lu, H.; Ahlawat, P.; Mishra, A.; Yang, Y.; Hope, M. A.; Eickemeyer, F. T.; Kim, M. Pseudo-halide anion engineering for α-$FAPbI_3$ perovskite solar cells. *Nature* **2021**, *592*, 381.

(73) Li, Y.-F.; Kou, Z.-L.; Feng, J.; Sun, H.-B. Plasmon-enhanced organic and perovskite solar cells with metal nanoparticles. *Nanophotonics* **2020**, *9*, 3111.

(74) Siavash Moakhar, R.; Gholipour, S.; Masudy-Panah, S.; Seza, A.; Mehdikhani, A.; Riahi-Noori, N.; Tafazoli, S.; Timasi, N.; Lim, Y. F.; Saliba, M. Recent Advances in Plasmonic Perovskite Solar Cells. *Adv. Sci.* **2020**, *7*, 1902448.

(75) Fu, N.; Bao, Z. Y.; Zhang, Y.-L.; Zhang, G.; Ke, S.; Lin, P.; Dai, J.; Huang, H.; Lei, D. Y. Panchromatic thin perovskite solar cells with broadband plasmonic absorption enhancement and efficient light scattering management by Au@Ag core-shell nanocuboids. *Nano Energy* **2017**, *41*, 654.

(76) Zhang, W.; Saliba, M.; Stranks, S. D.; Sun, Y.; Shi, X.; Wiesner, U.; Snaith, H. J. Enhancement of perovskite-based solar cells employing core-shell metal nanoparticles. *Nano Lett.* **2013**, *13*, 4505.

(77) Chen, L.-C.; Tien, C.-H.; Lee, K.-L.; Kao, Y.-T. Efficiency Improvement of $MAPbI_3$ Perovskite Solar Cells Based on a $CsPbBr_3$ Quantum Dot/Au Nanoparticle Composite Plasmonic Light-Harvesting Layer. *Energies* **2020**, *13*, 1471.

(78) Gao, Y.; Zhang, J.; Zhang, Z.; Li, Z.; Xiong, Q.; Deng, L.; Zhou, Q.; Meng, L.; Du, Y.; Zuo, T.; et al. Plasmon-Enhanced Perovskite Solar Cells with Efficiency Beyond 21%: The Asynchronous Synergistic Effect of Water and Gold Nanorods. *Chempluschem* **2021**, *86*, 291.

(79) Jackson, J.; Halas, N. Silver nanoshells: variations in morphologies and optical properties. *J. Phys. Chem. B* **2001**, *105*, 2743.

(80) Qin, P.; Wu, T.; Wang, Z.; Xiao, L.; Ma, L.; Ye, F.; Xiong, L.; Chen, X.; Li, H.; Yu, X. Grain Boundary and Interface Passivation with Core-Shell Au@ CdS Nanospheres for High-Efficiency Perovskite Solar Cells. *Adv. Funct. Mater.* **2020**, *30*, 1908408.

(81) Stöber, W.; Fink, A.; Bohn, E. Controlled growth of monodisperse silica spheres in the micron size range. *J. Colloid Interface Sci.* **1968**, *26*, 62.

(82) Park, J.; Kim, K.; Jo, E.-J.; Kim, W.; Kim, H.; Lee, R.; Lee, J. Y.; Jo, J. Y.; Kim, M.-G.; Jung, G. Y. Plasmon enhanced up-conversion nanoparticles in perovskite solar cells for effective utilization of near infrared light. *Nanoscale* **2019**, *11*, 22813.

(83) Duff, D. G.; Baiker, A.; Edwards, P. P. A new hydrosol of gold clusters. 1. Formation and particle size variation. *Langmuir* **1993**, *9*, 2301.

(84) Levard, C.; Hotze, E. M.; Colman, B. P.; Dale, A. L.; Truong, L.; Yang, X.; Bone, A. J.; Brown Jr, G. E.; Tanguay, R. L.; Di Giulio, R. T. Sulfidation of silver nanoparticles: natural antidote to their toxicity. *Environ. Sci. Technol.* **2013**, *47*, 13440.

(85) Park, J.; Kim, K.; Jo, E. J.; Kim, W.; Kim, H.; Lee, R.; Lee, J. Y.; Jo, J. Y.; Kim, M. G.; Jung, G. Y. Plasmon enhanced up-conversion nanoparticles in perovskite solar cells for effective utilization of near infrared light. *Nanoscale* **2019**, *11*, 22813.

(86) Stolterfoht, M.; Caprioglio, P.; Wolff, C. M.; Márquez, J. A.; Nordmann, J.; Zhang, S.; Rothhardt, D.; Hörmann, U.; Amir, Y.; Redinger, A. The impact of energy alignment and interfacial recombination on the internal and external open-circuit voltage of perovskite solar cells. *Energy Environ. Sci.* **2019**, *12*, 2778.

(87) Ma, X.; Ma, B.; Yu, T.; Xu, X.; Zhang, L.; Wang, W.; Cao, K.; Deng, L.; Chen, S.; Huang, W. Indepth Studies on Working Mechanism of Plasmon-Enhanced Inverted Perovskite Solar Cells Incorporated with Ag@ SiO_2 Core–Shell Nanocubes. *ACS Appl. Energy Mater.* **2019**, *2*, 3605.

(88) Kim, H.; Byun, H. R.; Kim, B.; Jeong, M. S. Gold Nanoparticles-embedded $MAPbI_3$ Perovskite Thin Films. *J Korean Phys Soc* **2018**, *73*, 1725.

(89) Chan, K.; Wright, M.; Elumalai, N.; Uddin, A.; Pillai, S. Plasmonics in organic and perovskite solar cells: optical and electrical effects. *Adv. Opt. Mater.* **2017**, *5*, 1600698.

(90) Yao, K.; Zhong, H.; Liu, Z.; Xiong, M.; Leng, S.; Zhang, J.; Xu, Y.-x.; Wang, W.; Zhou, L.; Huang, H. Plasmonic metal nanoparticles with core-bishell structure for high-performance organic and perovskite solar cells. *ACS nano* **2019**, *13*, 5397.

(91) Ball, J. M.; Petrozza, A. Defects in perovskite-halides and their effects in solar cells. *Nat. Energy* **2016**, *1*, 1.

(92) Wang, Q.; Wu, W. Temperature and excitation wavelength-dependent photoluminescence of $CH_3NH_3PbBr_3$ crystal. *Opt. Lett.* **2018**, *43*, 4923.

(93) Shojaee, S.; Harriman, T.; Han, G.; Lee, J.-K.; Lucca, D. Substrate effects on photoluminescence and low temperature phase transition of methylammonium lead iodide hybrid perovskite thin films. *Appl. Phys. Lett.* **2017**, *111*, 023902.

(94) Fang, Y.; Wei, H.; Dong, Q.; Huang, J. Quantification of re-absorption and re-emission processes to determine photon recycling efficiency in perovskite single crystals. *Nat. Commun.* **2017**, *8*, 1.

(95) Wu, X.; Jiang, X.-F.; Hu, X.; Zhang, D.-F.; Li, S.; Yao, X.; Liu, W.; Yip, H.-L.; Tang, Z.; Xu, Q.-H. Highly stable enhanced near-infrared amplified spontaneous emission in solution-processed perovskite films by employing polymer and gold nanorods. *Nanoscale* **2019**, *11*, 1959.

(96) Juan, F.; Xu, F.; Wang, M.; Wang, M.; Hou, G.; Xu, J.; Wei, H.; Wang, Y.; Wu, Y.; Cao, B. Photoluminescence enhancement of perovskite CsPbBr3 quantum dots by plasmonic Au nanorods. *Chem. Phys.* **2020**, *530*, 110627.

(97) Saliba, M.; Zhang, W.; Burlakov, V. M.; Stranks, S. D.; Sun, Y.; Ball, J. M.; Johnston, M. B.; Goriely, A.; Wiesner, U.; Snaith, H. J. Plasmonic-Induced Photon Recycling in Metal Halide Perovskite Solar Cells. *Adv. Funct. Mater.* **2015**, *25*, 5038.

(98) Habisreutinger, S. N.; Noel, N. K.; Snaith, H. J. Hysteresis index: A figure without merit for quantifying hysteresis in perovskite solar cells. *ACS Energy Lett.* **2018**, *3*, 2472.

(99) Bathula, C.; Jana, A.; Opoku, H.; Youi, H.-K.; Ghfar, A. A.; Ahmed, A. T. A.; Kim, H.-S. Interfacial engineering of quasi-2D formamidinium lead iodide nanosheets for perovskite solar cell by mechanochemical approach. *Surf. Interfaces* **2021**, *27*, 101551.

(100) Seo, J. Y.; Uchida, R.; Kim, H. S.; Saygili, Y.; Luo, J.; Moore, C.; Kerrod, J.; Wagstaff, A.; Eklund, M.; McIntyre, R. Boosting the efficiency of perovskite solar cells with CsBr-modified mesoporous TiO_2 beads as electron-selective contact. *Adv. Funct. Mater.* **2018**, *28*, 1705763.

(101) Sidhik, S.; Cerdan Pasaran, A.; Esparza, D.; Lopez Luke, T.; Carriles, R.; De la Rosa, E. Improving the optoelectronic properties of mesoporous TiO_2 by cobalt doping for high-performance hysteresis-free perovskite solar cells. *ACS Appl. Mater. Interfaces* **2018**, *10*, 3571.

(102) Min, H.; Lee, D. Y.; Kim, J.; Kim, G.; Lee, K. S.; Kim, J.; Paik, M. J.; Kim, Y. K.; Kim, K. S.; Kim, M. G. Perovskite solar cells with atomically coherent interlayers on SnO_2 electrodes. *Nature* **2021**, *598*, 444.

(103) Wen, L.; Rao, Y.; Zhu, M.; Li, R.; Zhan, J.; Zhang, L.; Wang, L.; Li, M.; Pang, S.; Zhou, Z. Reducing Defects Density and Enhancing Hole Extraction for Efficient Perovskite Solar Cells Enabled by π-Pb^{2+} Interactions. *Angew. Chem. Int. Ed.* **2021**, *60*, 17356.

(104) Park, S. Y.; Zhu, K. Advances in SnO_2 for Efficient and Stable n-i-p Perovskite Solar Cells. *Adv. Mater.* **2022**, *34*, 2110438.

(105) Ren, X.; Liu, Y.; Lee, D. G.; Kim, W. B.; Han, G. S.; Jung, H. S.; Liu, S. Chlorine-modified SnO_2 electron transport layer for high-efficiency perovskite solar cells. *InfoMat* **2020**, *2*, 401.

(106) Wang, H.; Cao, S.; Yang, B.; Li, H.; Wang, M.; Hu, X.; Sun, K.; Zang, Z. NH_4Cl-modified ZnO for high-performance $CsPbIBr_2$ perovskite solar cells via low-temperature process. *Sol. RRL* **2020**, *4*, 1900363.

(107) Zhang, F.; Ye, S.; Zhang, H.; Zhou, F.; Hao, Y.; Cai, H.; Song, J.; Qu, J. Comprehensive passivation strategy for achieving inverted perovskite solar cells with efficiency exceeding 23% by trap passivation and ion constraint. *Nano Energy* **2021**, *89*, 106370.

(108) Lv, Z.; He, L.; Jiang, H.; Ma, X.; Wang, F.; Fan, L.; Wei, M.; Yang, J.; Yang, L.; Yang, N. Diluted-CdS Quantum Dot-Assisted SnO_2 Electron Transport Layer with Excellent Conductivity and Suitable Band Alignment for High-Performance Planar Perovskite Solar Cells. *ACS Appl. Mater. Interfaces* **2021**, *13*, 16326.

(109) Ma, R.; Ren, Z.; Li, C.; Wang, Y.; Huang, Z.; Zhao, Y.; Yang, T.; Liang, Y.; Sun, X. W.; Choy, W. C. Establishing multifunctional interface layer of perovskite ligand modified lead sulfide quantum dots for improving the performance and stability of perovskite solar cells. *Small* **2020**, *16*, 2002628.

(110) Wang, P.; Chen, B.; Li, R.; Wang, S.; Ren, N.; Li, Y.; Mazumdar, S.; Shi, B.; Zhao, Y.; Zhang, X. Cobalt chloride hexahydrate assisted in reducing energy loss in perovskite solar cells with record open-circuit voltage of 1.20 V. *ACS Energy Lett.* **2021**, *6*, 2121.

(111) Dutta, D.; Bahadur, D. Influence of confinement regimes on magnetic property of pristine SnO 2 quantum dots. *J. Mater. Chem.* **2012**, *22*, 24545.

(112) Yang, X.; Yang, J.; Khan, J.; Deng, H.; Yuan, S.; Zhang, J.; Xia, Y.; Deng, F.; Zhou, X.; Umar, F.; et al. Hydroiodic Acid Additive Enhanced the Performance and Stability of PbS-QDs Solar Cells via Suppressing Hydroxyl Ligand. *Micro Nano Lett.* **2020**, *12*, 37.

(113) Yang, D.; Yang, R.; Wang, K.; Wu, C.; Zhu, X.; Feng, J.; Ren, X.; Fang, G.; Priya, S.; Liu, S. F. High efficiency planar-type perovskite solar cells with negligible hysteresis using EDTA-complexed SnO2. *Nat. Commun.* **2018**, *9*, 1.

(114) Fan, C.-M.; Peng, Y.; Zhu, Q.; Lin, L.; Wang, R.-X.; Xu, A.-W. Synproportionation reaction for the fabrication of Sn^{2+} self-doped SnO_{2-x} nanocrystals with tunable band structure and highly efficient visible light photocatalytic activity. *J. Phys. Chem. C* **2013**, *117*, 24157.

(115) Li, H.; Jiao, S.; Ren, J.; Li, H.; Gao, S.; Wang, J.; Wang, D.; Yu, Q.; Zhang, Y.; Li, L. Reaction mechanism of a PbS-on-ZnO heterostructure and enhanced photovoltaic diode performance with an interface-modulated heterojunction energy band structure. *Phys. Chem. Chem. Phys.* **2016**, *18*, 4144.

(116) Park, S. Y.; Zhu, K. Advances in SnO_2 for Efficient and Stable n-i-p Perovskite Solar Cells. *Adv. Mater.* **2022**, *34,* 2110438.

(117) Jung, E. H.; Chen, B.; Bertens, K.; Vafaie, M.; Teale, S.; Proppe, A.; Hou, Y.; Zhu, T.; Zheng, C.; Sargent, E. H. Bifunctional surface engineering on SnO_2 reduces energy loss in perovskite solar cells. *ACS Energy Lett.* **2020**, *5*, 2796.

(118) Cao, Y.; Stavrinadis, A.; Lasanta, T.; So, D.; Konstantatos, G. The role of surface passivation for efficient and photostable PbS quantum dot solar cells. *Nat. Energy* **2016**, *1*, 1.

(119) Prathapani, S.; Choudhary, D.; Mallick, S.; Bhargava, P.; Yella, A. Experimental evaluation of room temperature crystallization and phase evolution of hybrid perovskite materials. *CrystEngComm* **2017**, *19*, 3834.

(120) Zheng, X.; Lei, H.; Yang, G.; Ke, W.; Chen, Z.; Chen, C.; Ma, J.; Guo, Q.; Yao, F.; Zhang, Q. Enhancing efficiency and stability of perovskite solar cells via a high mobility p-type PbS buffer layer. *Nano Energy* **2017**, *38*, 1.

(121) Dong, J.; Jia, J.; Feng, X.; Shi, B.; Wu, Y.; Zhang, Y.; Wu, J.; Cao, B. Ligand exchange of SnO2 effectively improving the efficiency of flexible perovskite solar cells. *J. Alloys Compd.* **2021**, *883*, 160827.

(122) Yuan, Y.; Huang, J. Ion Migration in Organometal Trihalide Perovskite and Its Impact on Photovoltaic Efficiency and Stability. *Acc. Chem. Res.* **2016**, *49*, 286.

(123) Zheng, S.; Chen, J.; Johansson, E. M. J.; Zhang, X. PbS Colloidal Quantum Dot Inks for Infrared Solar Cells. *iScience* **2020**, *23*, 101753.

(124) Zhu, P.; Gu, S.; Luo, X.; Gao, Y.; Li, S.; Zhu, J.; Tan, H. Simultaneous contact and grain-boundary passivation in planar perovskite solar cells using SnO_2-KCl composite electron transport layer. *Adv. Energy Mater.* **2020**, *10*, 1903083.

(125) Liang, J.; Han, X.; Qiu, Y.; Fang, Q.; Zhang, B.; Wang, W.; Zhang, J.; Ajayan, P. M.; Lou, J. A low-cost and high-efficiency integrated device toward solar-driven water splitting. *ACS Nano* **2020**, *14*, 5426.

(126) Wang, S.; Chen, P.; Bai, Y.; Yun, J. H.; Liu, G.; Wang, L. New BiVO4 Dual Photoanodes with Enriched Oxygen Vacancies for Efficient Solar-Driven Water Splitting. *Adv. Mater.* **2018**, *30*, 1800486.

(127) Kim, M.; Lee, B.; Ju, H.; Kim, J. Y.; Kim, J.; Lee, S. W. Oxygen-Vacancy-Introduced $BaSnO_3-\delta$ Photoanodes with Tunable Band Structures for Efficient Solar-Driven Water Splitting. *Adv. Mater.* **2019**, *31*, 1903316.

(128) Li, N.; Wu, J.; Lu, Y.; Zhao, Z.; Zhang, H.; Li, X.; Zheng, Y.-Z.; Tao, X. Stable multiphasic 1T/2H $MoSe_2$ nanosheets integrated with 1D sulfide semiconductor for drastically enhanced visible-light photocatalytic hydrogen evolution. *Appl. Catal.* **2018**, *238*, 27.

(129) Zemski, K.; Justes, D.; Castleman, A. Studies of metal oxide clusters: Elucidating reactive sites responsible for the activity of transition metal oxide catalysts. *J. Phys. Chem. B* 2002, 106, 24, 6136.

(130) Perović, K.; Kovačić, M.; Kušić, H.; Lavrenčič Štangar, U.; Fresno, F.; Dionysiou, D. D.; Bozic, A. L. Recent achievements in development of TiO_2-based composite photocatalytic materials for solar driven water purification and water splitting. *Materials* **2020**, *13*, 1338.

(131) Yaw, C. S.; Ruan, Q.; Tang, J.; Soh, A. K.; Chong, M. N. A Type II nn staggered orthorhombic V_2O_5/monoclinic clinobisvanite $BiVO_4$ heterojunction photoanode for photoelectrochemical water oxidation: Fabrication, characterisation and experimental validation. *Chem. Eng. J.* **2019**, *364*, 177.

(132) Patial, S.; Hasija, V.; Raizada, P.; Singh, P.; Singh, A. A. P. K.; Asiri, A. M. Tunable photocatalytic activity of $SrTiO_3$ for water splitting: strategies and future scenario. *J. Environ. Chem. Eng.* **2020**, *8*, 103791.

(133) Sun, Q.; Wang, N.; Yu, J.; Yu, J. C. A hollow porous CdS photocatalyst. *Adv. Mater.* **2018**, *30*, 1804368.

(134) Gharibzadeh, S.; Abdollahi Nejand, B.; Jakoby, M.; Abzieher, T.; Hauschild, D.; Moghadamzadeh, S.; Schwenzer, J. A.; Brenner, P.; Schmager, R.; Haghighirad, A. A. Record open-circuit voltage wide-bandgap perovskite solar cells utilizing 2D/3D perovskite heterostructure. *Adv. Energy Mater.* **2019**, *9*, 1803699.

(135) Zhang, H.; Yang, Z.; Yu, W.; Wang, H.; Ma, W.; Zong, X.; Li, C. A Sandwich-Like Organolead Halide Perovskite Photocathode for Efficient and Durable Photoelectrochemical Hydrogen Evolution in Water. *Adv. Energy Mater.* **2018**, *8*, 1800795.

(136) Crespo-Quesada, M.; Pazos-Outon, L. M.; Warnan, J.; Kuehnel, M. F.; Friend, R. H.; Reisner, E. Metal-encapsulated organolead halide perovskite photocathode for solar-driven hydrogen evolution in water. *Nat. Commun.* **2016**, *7*, 12555.

(137) Huang, H.; Pradhan, B.; Hofkens, J.; Roeffaers, M. B. J.; Steele, J. A. Solar-Driven Metal Halide Perovskite Photocatalysis: Design, Stability, and Performance. *ACS Energy Lett.* **2020**, *5*, 1107.

(138) Ahmad, S.; Sadhanala, A.; Hoye, R. L. Z.; Andrei, V.; Modarres, M. H.; Zhao, B.; Ronge, J.; Friend, R.; De Volder, M. Triple-Cation-Based Perovskite Photocathodes with AZO Protective Layer for Hydrogen Production Applications. *ACS Appl. Mater. Interfaces* **2019**, *11*, 23198.

(139) Kim, I. S.; Pellin, M. J.; Martinson, A. B. F. Acid-Compatible Halide Perovskite Photocathodes Utilizing Atomic Layer Deposited TiO_2 for Solar-Driven Hydrogen Evolution. *ACS Energy Lett.* **2019**, *4*, 293.

(140) Poli, I.; Hintermair, U.; Regue, M.; Kumar, S.; Sackville, E. V.; Baker, J.; Watson, T. M.; Eslava, S.; Cameron, P. J. Graphite-protected $CsPbBr_3$ perovskite photoanodes functionalised with water oxidation catalyst for oxygen evolution in water. *Nat. Commun* **2019**, *10*, 2097.

(141) Nam, S.; Mai, C. T. K.; Oh, I. Ultrastable Photoelectrodes for Solar Water Splitting Based on Organic Metal Halide Perovskite Fabricated by Lift-Off Process. *ACS Appl. Mater. Interfaces* **2018**, *10*, 14659.

(142) Tran, D. T.; Prabhakaran, S.; Kim, D. H.; Hameed, N.; Wang, H.; Kim, N. H.; Lee, J. H. Ruthenium single atoms implanted continuous MoS_2-Mo_2C heterostructure for high-performance and stable water splitting. *Nano Energy* **2021**, *88*, 106277.

(143) Yang, T. T.; Wang, A.; House, S. D.; Yang, J.; Lee, J.-K.; Saidi, W. A. Computationally Guided Design to Accelerate Discovery of Doped β-Mo_2C Catalysts toward Hydrogen Evolution Reaction. *ACS Catal.* **2022**, *12*, 11791.

(144) Quarti, C.; Mosconi, E.; Ball, J. M.; D'Innocenzo, V.; Tao, C.; Pathak, S.; Snaith, H. J.; Petrozza, A.; De Angelis, F. Structural and optical properties of methylammonium lead iodide across the tetragonal to cubic phase transition: implications for perovskite solar cells. *Energy Environ. Sci.* **2016**, *9*, 155.

(145) Masi, S.; Echeverría-Arrondo, C.; Salim, K. M.; Ngo, T. T.; Mendez, P. F.; Lopez-Fraguas, E.; Macias-Pinilla, D. F.; Planelles, J.; Climente, J. I.; Mora-Sero, I. Chemi-structural stabilization of formamidinium lead iodide perovskite by using embedded quantum dots. *ACS Energy Lett.* **2020**, *5*, 418.

(146) Lin, H.; Zhang, W.; Shi, Z.; Che, M.; Yu, X.; Tang, Y.; Gao, Q. Electrospinning Hetero-Nanofibers of Fe_3C-Mo_2C/Nitrogen-Doped-Carbon as Efficient Electrocatalysts for Hydrogen Evolution. *ChemSusChem* **2017**, *10*, 2597.

(147) Wang, S.; Lu, A.; Zhong, C.-J. Hydrogen production from water electrolysis: Role of catalysts. *Nano Converg.* **2021**, *8*, 1.

(148) Wu, Z.-Y.; Hu, B.-C.; Wu, P.; Liang, H.-W.; Yu, Z.-L.; Lin, Y.; Zheng, Y.-R.; Li, Z.; Yu, S.-H. Mo_2C nanoparticles embedded within bacterial cellulose-derived 3D N-doped carbon nanofiber networks for efficient hydrogen evolution. *NPG Asia Mater.* **2016**, *8*, e288.

(149) Wu, H. B.; Xia, B. Y.; Yu, L.; Yu, X.-Y.; Lou, X. W. D. Porous molybdenum carbide nano-octahedrons synthesized via confined carburization in metal-organic frameworks for efficient hydrogen production. *Nat. Commun.* **2015**, *6*, 1.

(150) Philippe, B.; Park, B.-W.; Lindblad, R.; Oscarsson, J.; Ahmadi, S.; Johansson, E. M.; Rensmo, H. k. Chemical and Electronic Structure Characterization of Lead Halide Perovskites and Stability Behavior under Different Exposures: A Photoelectron Spectroscopy Investigation. *Chem. Mater.* **2015**, *27*, 1720.